Dissertation

Numerical Study on the Hydrodynamic Loads and Motions of a Ship Maneuvering in Waves
波浪中で操縦運動する船の流体荷重と運動に関する数値的研究

Graduate School of Engineering Science

Yokohama National University

馬 程前

Ma Chengqian

Aug 2022

Abstract

With the increasing requirement for the navigation safety and economy, the maneuverability in actual sea conditions attract more and more attention nowadays. As one of the most complex problems in the research of ship hydrodynamics, the maneuver motions in waves involves the performance of ship resistance, propulsion, maneuvering, seakeeping, and stability in waves simultaneously. With the improvement of the computational resources and algorithm, a solution of the hydrodynamic loads and motions of a ship maneuvering in waves based on the computational fluid dynamics (CFD) method becomes possible recently.

The objective of this dissertation is to detect the wave effect on the hydrodynamic loads and motions during the ship maneuvering in waves using a CFD method, which can be divided into the captive model test simulations in waves and the free-running test simulations in waves. Firstly, the wave effect on the maneuvering hydrodynamic derivatives in following waves is researched by simulating the Planer Motion Mechanism (PMM) tests in the surf-riding condition for the first time. The overset grid and Euler overlay method is adopted to achieve the simulations. Good agreement between the simulated results and the experimental ones reveals the accuracy and effectiveness of the present method. The wave effect on the hydrodynamic derivatives is also obtained, and the course stability in waves is calculated based on those derivatives to reveal the reason for the occurrence of the broaching-to phenomenon.

To detect the wave effect on the hydrodynamic derivatives in a general wave condition, simulations of the PMM tests in head waves are carried out. The detailed change tendencies of the linear and nonlinear hydrodynamic derivatives in waves are summarized and calculation methods of all wave-affected hydrodynamic derivatives in numerical simulations are proposed.

Considering the complexity of the utilization of wave-affected hydrodynamic derivatives on trajectory predictions, the direct simulations of free-running tests in waves are researched. Based on the moving grid, overset mesh technique and the body force method for a propeller effect, a zigzag test and a turning test in calm water are simulated and validated by the experimental data with acceptable accuracy. Then, zigzag tests, turning tests and course-keeping tests in regular and irregular wave are simulated combining accuracy and efficiency. The hydrodynamic loads on the hull and rudder are analyzed and the flow filed information is provided.

In summary, the present research provides a useful method to conduct the captive model tests in waves which can be utilized for the research on captive model tests in waves later. In addition, the free-running test simulations in regular and irregular waves are achieved, which can contribute to the evaluation of the hydrodynamic performance and navigation safety in the future.

Contents

Chapter 1 Introduction

1.1 Background

Generally, considering the complexity of the hydrodynamic computations for vessels navigating in actual seaways, the computations are usually separated into several parts, such as the stability, resistance, propulsion, maneuvering, and seakeeping performance research based on the focused issues. All these single performance studies are developed independently. For instance, the traditional maneuverability research mainly focused on the turning ability, initial turning ability, yaw-checking and course-keeping ability, and stopping ability in calm water conditions (IMO, 2002a, 2002b). Several research methods on that, such as the database method, the model test method, and the computational method, are proposed and established to assess the maneuverability in calm water conditions drawn in Fig 1.1(ITTC, 2008). Similarly, the traditional seakeeping performance, which means the performance and motion response of the vessel in various seagoing conditions, is researched in a framework that the speed and heading angle of the vessel are constant (Reed and Beck, 2018). However, with the increasing requirements for navigation safety and operational efficiency, the comprehensive research on ship maneuverability in waves attracts more and more attention recently. It is because the ship resistance and propulsion performance in waves will be different requiring the maneuverability better than that in the calm water condition to keep the route or change the trajectory easily. Fig 1.2 shows the statistical marine casualties and incidents distributions during 2014-2020 for the ships flying a flag of EU Member States or the accidents occur within EU Member States' territorial sea. Obviously, "Loss of control – Loss of propulsion power" takes the largest proportion (22%) in all events, which is related with the minimum propulsion power to keep the maneuverability in waves. The navigational casualties, containing collision, contact, and grounding/stranding, which are related with the maneuverability directly, represent 43% of all casualty events over this period. Hence, the maneuverability, especially in adverse conditions, should be focused on.

Different from the single performance studies, the research on maneuverability in adverse conditions is a comprehensive topic concerning the added resistance in waves, the traditional maneuverability, the seakeeping performance, and the stability in waves simultaneously. The wave loads will affect the ship motions and the ship maneuvering motions have an influence on the wave field. The hydrodynamic computations for ships maneuvering in waves is hard to conduct relying on previous single performance study methods. Therefore, even though the hydrodynamic problem for ship maneuvering in adverse conditions has been proposed for several decades (Inoue and Murahashi, 1965), the development is slow restrained by the insufficient calculation resources and unsatisfied theoretical methods for a long time. Nowadays, with the development of the theoretical methods and the improvement of the calculation resources, many efficient

mathematical models and pure CFD (Computational Fluid Dynamics) algorithms are proposed, which makes it possible to solve the problem with accuracy and efficiency.

In addition to the scientific research value and the increasing requirement of safety, the related regulations also make the research on this topic important and urgent. To improve the energy efficiency and reduce greenhouse gas (GHG) emissions of ships, EEDI (Energy Efficiency Design Index) regulation is implemented by IMO (International Maritime Organization). The EEDI provides a specific required value for an individual ship design, expressed in grams of CO2 per ship's capacity mile and is calculated by the given formula based on the design parameters for a given ship. Since 2013, following an initial two-year (2013.01.01~2014.12.31) phase 0, new designed ship should meet the reference level which is to be tightened incrementally every five years. Some ship designers might prefer to lower the installed power rather than develop more efficient propulsion method or reduce the hull resistance to achieve the EEDI requirements, which can lead to insufficient propulsion and steering abilities of ships to maintain maneuverability in adverse conditions (Papanikolaou et al., 2015). Plenty of submissions to IMO (MSC 93/21/5, MSC 93/INF.13, MEPC 67/INF.22, MEPC 67/4/16) states the urgency for developing the criterion to ensure the maneuverability in adverse wave conditions. The 2013 Interim Guidelines for determining minimum propulsion power to maintain the maneuverability in waves (the Interim Guidelines) have been adopted by resolution MEPC.232(65) at MEPC 65 (IMO, 2013).

International cooperative researches are also widely carried out in this field. In the 25th, 26th, 27th and 28th ITTC (International Towing Tank Conference) maneuvering committee, this issue is discussed in special chapters (ITTC, 2008, 2011, 2014, 2017b). A specialist committee of maneuvering in waves was active in the 29th ITTC conference (ITTC, 2021). SHOPERA (Energy Efficient Safe SHip OPERAtion), the EU-funded project, is organized to conduct the efficient analysis of the performance of ships when they are operating in complex environmental and adverse weather conditions based on the present hydrodynamic simulation software. JASNAOE (Japan Society of Naval Architects and Ocean Engineers) also funded a project to develop the mathematical model for ship maneuverability in waves and determine the wave drift force.

In summary, the research on the performance of ship maneuvering in waves is of important scientific value, engineering value and economic value, and it should be researched and focused.

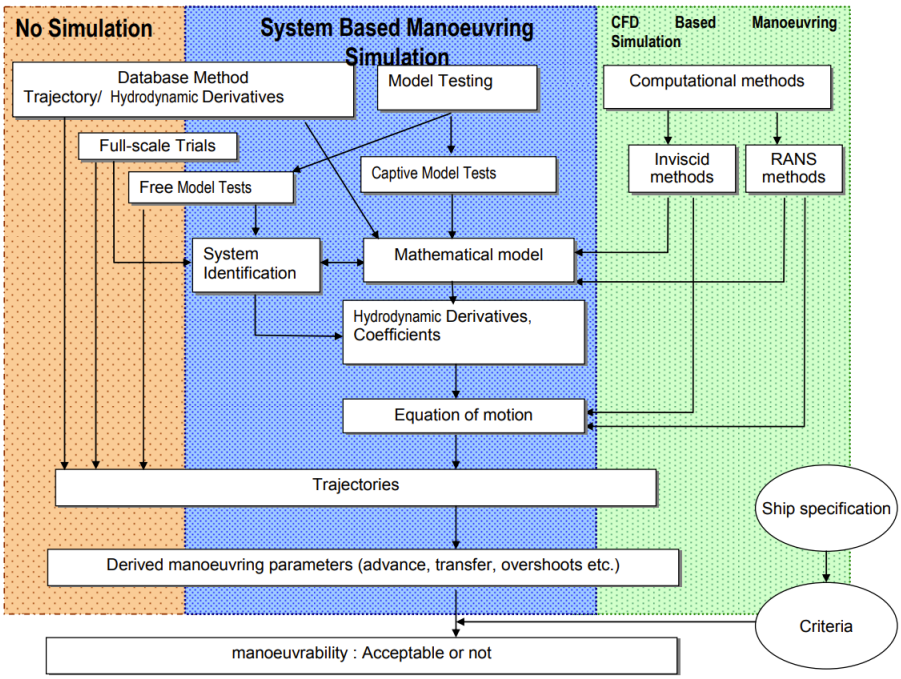

FIGURE 1.1 Overview of maneuvering prediction methods (ITTC, 2008)

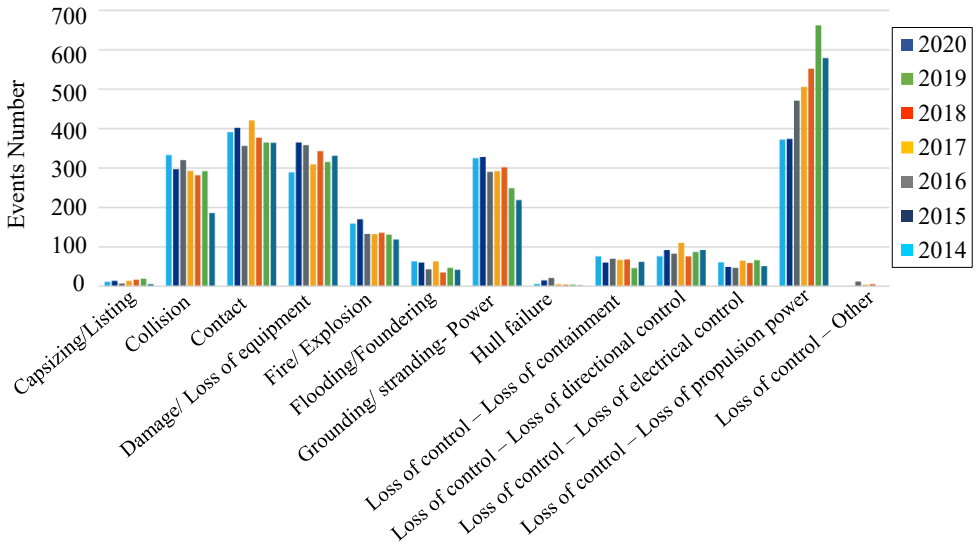

FIGURE 1.2 Distribution of casualty events with a ship over the period 2014-2020 (EMSA, 2021)

1.2 Present research situations

The research on the performance of the ship maneuvering in waves focuses on the obtain of ship's hydrodynamic loads and motions during the operations. At present, the ways to solve this problem can be classified into the experimental method, the potential flow theory method, and the pure CFD method.

1.2.1 Experimental methods

The experimental method can be separated into the free-running test method and the captive model test method. For the former one, it is conducted to obtain the hydrodynamic loads and motions during the maneuvering motion in waves directly with the aim of detecting the wave effect on loads and motions, validating the numerical prediction tools, and assessing the maneuverability of a ship in waves. Inoue and Murahashi (1965) carried out the turning circle tests of a cargo vessel and a tanker in calm water and regular waves. By investigation of the influence of drifting force on the course keeping and turning ability of the ship, they concluded that the ship progressing in waves tends to turn to the weatherside owing to the drifting forces, and the greater its deviation is, the less dynamical stability of the ship. This pioneering work emphasizes the importance of the wave drift force in the research of maneuverability in waves. Then, Hirano et al. (1980) conducted the turning circle tests of a 5m long Roll-on/Roll-off ship model in calm water and regular head waves with the constant wave height and different wavelengths ($\lambda/L = 0.35$, 0.50, 0.75, 1.00, and 2.40. λ and L denotes the wavelength and the ship length). They found the deviation of the turning trajectory in waves from that in the calm water condition might have the tendency to become larger when the wavelength becomes shorter. The effects of the rudder angle and the ship speed on the abovementioned deviation are also clarified. They also proposed a mathematical model in which the second order wave drift forces are added in the maneuvering model directly and compared the predicted trajectory with the experimental one. The good agreement shows the rationality of the mathematical model and the importance of the wave drift force on trajectory deviation. Next, Ueno et al (2003) performed the straight run test, turning circle test, zigzag test, and stopping test of a VLCC (Very Large Crude Carrier) in regular waves. Several different initial wave directions and wavelength ratios are selected with the wave height unchanged. They defined the turning circle drifting distance and drifting direction which are widely utilized to describe the drift of the turning circle in waves thereafter. In addition, they noticed that the drifting distance is larger in short wave conditions and the drifting forces in short wave conditions are larger than those in long wave conditions. The effect of the ballast on the trajectory was considered and discussed in their study. Nishimura and Hirayama (2003) focused on the roll motion during the ship maneuvering in waves. Based on the turning circle test of a fishing boat, they concluded that the maximum roll amplitude during a ship turns in head waves is remarkably larger than that in following seas. Besides, in most cases when ship runs in head or following seas, the reduction of turning time due to the large rudder area makes the rolling amplitude relatively small. Yasukawa (2006, 2008) systematically carried out the turning circle tests, zigzag tests, and stopping tests of a containership SR108 (also been known as S175) in regular and irregular waves. The results in irregular wave conditions show that the differences between the results in long-crested irregular and short-crested irregular wave are not obvious. He also proposed a mathematical model to predict the horizontal 3 DOF (degree of freedom) trajectory by adding the wave drift forces in the traditional calm-

water maneuvering model. The comparison between the simulation results and experimental ones reveals that the model can predict quite well when λ/L is larger than 0.7 but unsatisfactory in short wave condition. Sanada et al (2013) carried out the turning tests of an ONR Tumblehome ship model in calm water and regular waves to provide validation information for their CFD simulation results. Xu (2015) and Zhu (2016) conducted the turning circle tests, zigzag tests and stopping tests in calm water and regular waves for a low-speed containership S175 in the Ocean Engineering Model Basin of Shanghai Jiao Tong University. The maneuvering criteria parameters in different wave conditions are obtained. They also explored the rudder speed effect on the motion and trajectories for the maneuvering motion in waves. Hasnan et al (2020) performed turning tests of a tanker KVLCC2 and a container ship KCS in short-crested irregular waves. They proposed theoretical formulas for drifting distance and drifting direction. Yasukawa et al (2021) conducted turning tests of KCS to validate the new 6 DOF mathematical model based on the two-time-scale method which shows good agreement.

The free-running tests of ship maneuvering in waves are valuable and important for exploring the physical phenomenon, validating the numerical simulation codes or mathematical models, and evaluating the performance of the full-scale ship. However, different components of the hydrodynamic loads. For example, the second- and first-order wave forces, which are important and indispensable for simulations based on the potential flow theory methods, are hard to obtain from the free-running tests. To obtain these components of the hydrodynamic loads for establishing and validating the mathematical models, the captive model tests should be performed. Xu et al (2007) conducted the PMM (Planar Motion Mechanism) tests in regular waves to obtain the wave-drift added mass and wave-drift damping coefficients which are considered as the components of the wave-drift forces. They only conducted the pure sway tests firstly and concluded that the sway wave-drift damping coefficients are close to those in calm water. The sway wave-drift added mass is obviously smaller than that in calm water. Then, Xu et al (2011) considered the yaw motion based on the previous research. The wave effect on the wave-drift added mass and damping coefficients are obtained. Yasukawa and Adnan (2008) conducted the oblique moving tests in waves to obtain the wave-drift forces of SR108. Shigunov et al (2018) provided the international benchmark experimental results of the captive model tests in waves. Though the results of added resistance in head waves, the turning circle in calm water, regular wave and irregular waves, and the zigzag test, four different numerical methods on wave forces are compared with the experimental results to validate and improve the present prediction methods. They concluded that the present 3D panel method is good in most cases, the strip method performed generally poor for the target ships, the RANS (Reynolds averaged Navier Stokes) method demonstrates the ability to provide accurate results but frequently delivered erratic results, and empirical method provides promising results. Yasukawa et al (2019) performed the straight running tests in different wave conditions to obtain the wave-induced steady forces which are utilized to evaluate the zero-speed three-dimensional panel method (3DPM) and the strip

method based on Kochin-function method (SKFM). They found that the added resistance and steady lateral forces in waves calculated from two methods are acceptable from a practical perspective, but the accuracy was insufficient for prediction of the steady yaw moments. In addition, both methods are feasible for predicting turning motions in irregular waves.

The above-mentioned captive model tests in waves focus on obtaining the seakeeping components rather than the maneuvering parts. In fact, waves also have an effect on the maneuvering hydrodynamic coefficients. Hamamoto (1971, 1973) and later Renilson (1982) applied a slender body theory without a free-surface condition to calculate the maneuvering coefficients in following waves. They assumed that the maneuvering coefficients in waves can be separated into the potential and viscous flow components, and the viscous component will remain unchanged in waves. Therefore, they could only calculate the change of the potential flow component using the traditional seakeeping method to obtain the maneuvering hydrodynamic derivatives in waves. To validate this assumption, the experiments of the PMM (Planar Motion Mechanism) tests in the surf-riding condition is carried out in the towing tank and the circulating water channel. The surf-riding condition is achieved by using a flat plate ahead of the PMM facility. When the PMM facility moving ahead, a wave whose relative position with the ship model is fixed will be generated. Later, Fujino et al (1982) used a slender-body theory considering the free-surface condition to obtain the hydrodynamic derivatives under the surf-riding condition in following waves and compared them with the experimental data. The experiments were carried out for a flat plane rather than a ship model under the surf-riding condition in following waves. Relying on a similar experimental setup, Motora et al (1981) also performed PMM tests under the surf-riding condition. The reasons for the occurrence of the broaching-to phenomenon were discussed based on the calculated wave-effected hydrodynamic derivatives in waves. Son and Nomoto (1982) carried out the similar captive model tests in following waves generated by a wave-making board to achieve the surf-riding condition. Then, the hydrodynamic derivatives in this condition were obtained. Furthermore, the course stability index under the surf-riding condition was calculated which reveals that the reduced course stability index might be the reason for the unstable phenomenon. Bonci et al (2019) measured the forces and moments on a high-speed craft in waves employing captive model tests in following and stern quartering waves at the Seakeeping & Manoeuvring Basin of MARIN. Araki et al (2011) considered the wave effect on the hydrodynamic derivatives to improve the prediction accuracy of the broaching-to phenomenon.

1.2.2 Potential flow theory methods

Although the experimental method is considered to be the most reliable one, the high cost and complexity in local flow measurement hold back its application and the free-running tests are always conducted only at the final design stage. The numerical simulations can solve that problem. The theoretical method based on the potential flow theory can be classified into the two-time-scale method and the unified method. The

two-time-scale method considers the problem of maneuverability in waves as the superposition of the high-frequency motions and the low-frequency motions, which can rely on the traditional maneuvering method and the seakeeping method, respectively. The unified method requires a solution of the motion of the ship at the same time containing the high-frequency forces and the low-frequency parts. For the unified method, Hamamoto and Kim (1993) proposed a new coordinate system named "Horizontal body axes" with the aim of describing the maneuvering motions in horizontal plane, rolling motion in lateral plane and seakeeping motion in vertical plane simultaneously. The Froude-Krylov forces and hydrodynamic forces are evaluated in horizontal body coordinates. The time domain simulations for turning and zigzag tests in waves are carried out, which reveals the availablility of this method. Nishimura and Hirayama (2003) also added the Froude-Krylov forces in the 6 DOF motion equations to simulate the motions in waves. Considering the change of the inertia force with the change of the incident wave frequency, Baily (1997) and Ayaz et al (2006) added the time domain radiation forces based on the impulse response function method (Cummins, 1962) in addition to the Froude-Krylov forces and the diffraction forces in the equations.

As for the two-time-scale method, Triantafyllou (1982) proposed a combined method to considering the high-frequency motions and low-frequency motions for a zero-speed offshore structure. Then, Nonaka (1990) extended the method to the ship with a forward velocity. Skejic and Faltinsen (2008) conducted the simulations considering the second-order wave drift force obtained by using a variety of different strip theories. However, their analysis was based on a quasi-static assumption. Seo and Kim (2011) broke through this limitation by using the time-domain three-dimensional Rankine source panel method to calculate the wave forces and conducted a coupled maneuvering and seakeeping analysis of the ship in regular waves. Yu et al (2021) have extended this method to the irregular wave conditions.

1.2.3 Pure CFD methods

The potential flow theory methods rely on the mathematical models ignoring the viscous effect, which makes it difficult to resolve the complex flow considering the large drift angle motion, rotating propellers, and moving rudders. The CFD methods provide a flow field which is closer to the real physical phenomenon and can reflect more reliable and accurate results of the unsteady local flows. Restrained by complexity and cost, there were a limited number of pure CFD simulation research for ship maneuvers in waves. Fortunately, the improvement of the new numerical algorithms and computational resources nowadays contribute greatly to the development of the pure CFD method.

At the beginning, the simulations of the captive model tests in the calm water condition were widely performed to obtain the hydrodynamic derivatives in calm water. Ohmori (1998) developed WISDAM-V to simulate the static oblique towing tests, CMT (circular motion test) and PMM tests. Hydrodynamic forces and moments showed good agreement. Then, Orihara and Miyata (2003) developed WISDAM-X based on the previous code and the overset mesh technique, and the motions of SR108 containership

were simulated. Tahara et al (2002) simulated the oblique towing tests in different Froude numbers and drift angles, and the uncertainty analysis based on five grids with various sizes was conducted. Besides, the flow field information was also shown to reveal the superiority of the CFD method. Sakamoto et al (2012a) conducted the pure CFD simulations and experiments of the straight-ahead tests, static drift tests, pure sway and pure yaw tests. Based on the RANS code, the single-phase level set method is utilized for capturing the free surface and isotropic blended $k-\varepsilon/k-\omega$ (BKW) method is adopted as the turbulence model. The overset grid technique is adopted in their simulations. By verification and validation of the forces and hydrodynamic derivatives, they concluded that the wide background region is strongly recommended for the static drift test for the faster statistical convergence owing to the dissipation of spurious free surface waves. The simulated forces and hydrodynamic derivatives are in good agreement with the experimental ones. For the flow field information (Sakamoto et al, 2012b), they also validated the local flow characteristics using the SPIV measurement data, which showed satisfying coincidence. Yoon et al (2015a, 2015b) conducted the benchmark research on the CFD simulations for the surface combatant 5415 in PMM tests. The forces, moments, motions, and flow field information were simulated and compared with the experimental data. the detailed verification and validation were conducted. They concluded that the linear hydrodynamic derivatives could be accurate with the error smaller than 10%, but the nonlinear derivatives were not.

Later, the simulations for the free-running tests in calm water were performed owing to the improvement of the computational methods. Compared with the captive model test simulations, the simulations for the free-running tests should consider the self-propulsion, moving rudders and rotating propeller. Stern et al (1988) had ever simulated the hull-propeller interaction using the body force method based on the lifting-surface theory. Similarly, Kawamura et al (1997) simulated the self-propulsion case using a simplified propeller model. Phillips et al (2009) presented a method that significantly reduces computational cost by coupling a blade element momentum theory (BEMT) propeller model with the solution of the Reynolds averaged Navier Stokes equations. Then, they (Phillips et al, 2010) compared experimental results with numerical simulations using three different body-force propeller models which were the uniform thrust distribution without torque, the Hough and Ordway model with prescribed radial destitution of thrust and torque, radial and tangential distributions of thrust and torque from BEMT. The first one is not suitable due to the poor prediction accuracy of rudder resistance behind propeller. The other two methods are much more suitable for the research considering the hull-propeller-rudder interaction. Broglia et al (2013) simulated several different propeller models to research the effectiveness of the prediction methods for the turning motions. The classical Hough and Ordway model modified by two various semi-empirical models for the side force and the model based on the blade element theory are compared. It has been found that, accurate prediction of the turning circle is achieved when using modified Hough and Ordway models. The increase in computational resources compared with the traditional one is almost negligible. Afterwards, they (Dubbioso et al, 2013) carried out the zigzag test

simulations using different propeller models to select the accurate and efficient one. Through their simulations with structured blocks and overlap method, they concluded that the propeller effect and loads have a negligible effect on the trajectories and motions, which might be due to the small drift angle and low speed of their cases. For the simulation results, the predicted first overshoot angle is satisfactory, whereas the second overshoot angle is overpredicted. Carrica et al (2013) performed the simulations of turning tests and zigzag tests using the simple actuator disk approach. The error for the predicted maneuvering parameters is smaller than 10% which is much less than the error observed during the blind tests at SIMMAN 2008. In that paper, they also conducted the full-scale simulations and the simulations in wave conditions successfully but without validation by experiments.

The actual rotating propeller rather than the body force method for the propulsion force simulation is also adopted by some scholars. There will be two methods to deal with the propeller motion, one is the sliding mesh technique, the other is the overset mesh technique. For the former one, there are some typical works, such as Seo et al (2010), Queutey et al (2012), and el Moctar et al (2014). For the later one, Mofidi and Carrica (2014) simulated the zigzag maneuvers of KCS model with moving rudder and rotating propeller. The overset mesh technique was adopted which showed satisfying simulation results. Later, Broglia et al (2015) and Dubbioso et al (2016) conducted the maneuvering motion simulations to assess the CFD code ability using the overset mesh. Compared with the body force method, the actual rotating propeller can capture more details on the hull-propeller interaction and the flow filed information is much closer to the real condition. However, the time step should be much smaller to make the propeller rotates a small angle during one time step which is about one tenth of the time step for the body force method. In addition, the grid around and behind the propeller should be finer. Hence, the calculation resources and required time are much larger.

In recent years, the simulations for the free-running tests in waves are also carried out. Carrica et al (2015) started to simulate the turning tests in regular and irregular waves using the rotating propeller. Through the course mesh, they tried to minimize the simulation time and made the time ratio around 200 between the CFD CPU time and real physical time. Wang et al (2017) developed a course-keeping control module in the in-house RANS code developed on open-source platform OpenFOAM. Overset grid method and 6 DOF module were adopted to simulate the course-keeping maneuvers of a ONR Tumblehome model 5613 in head, quartering, and beam wave conditions. The motions, trajectories, and speeds were validated by the experimental ones, which shows the feasibility of the pure CFD methods. Due to the actual rotating propeller, the time step was set to 0.0005s corresponding to approximately 1.5degs of propeller rotation per time step. Each case required 225 wall clock hours using 40 processors. Later, they (Wang and Wan, 2018. Wang et al, 2018) performed the simulations for the turning maneuvers and zigzag maneuvers in head, quartering, and beam seas. The predicted results show good agreement with the experiment measurement with error up to 10%, which is satisfactory. The wall clock hours for turning maneuvers and zigzag maneuvers are 347h and 1206h, respectively. Kim et al (2021a) researched the wavelength effect on the course-keeping maneuvers and turning maneuvers in bow seas. Later, the course-

keeping control and turning maneuvers in different wave directions were researched by them (Kim et al, 2021b).

1.3 Scope and objectives

Based on the above-mentioned current research status and the future requirement on the prediction of detailed flow field information, ship performance, and the hull-propeller-rudder interaction in waves, the author aims to adopt the CFD method to solve the problem of maneuverability prediction in waves from two aspects.

On the one hand, the CFD method on simulating captive model tests in waves are established to obtain the wave effect on maneuvering hydrodynamic derivatives. The hydrodynamic derivatives are crucial in the mathematical models based on the potential flow theory methods. The course-stability can also be assessed relying on these parameters. However, the hydrodynamic derivatives in waves are assumed to be the same as those in calm water in many mathematical models. Therefore, the CFD simulations on captive models test in waves can not only obtain the wave effect on hydrodynamic derivatives efficiently but also provide the course-stability index in waves to analyze the maneuverability in specific adverse conditions directly.

On the other hand, considering the problem of unsatisfactory efficiency of the present simulations and insufficient research on the prediction of maneuvering motions in waves, the free-running test in waves simulations are carried out for the purpose of directly analyzing the maneuvering performance under adverse wave conditions and revealing the flow field information during the maneuvers in seas. Different from many previous simulations, the structured mesh is generated. Even though the unstructured grid can be generated more conveniently because of its high degree of automation, the structured mesh is chosen in this study for its high degree of quality, better convergence, less memory and required time to achieve the simulations combining efficiency and accuracy. The short-crested irregular wave condition is also researched in the present study. In addition, the time histories of the self-propulsion factors and the hydrodynamic forces on the hull are provided.

According to these two aspects, the main work of present thesis can be listed as follows:

1. Based on the RANS code, the simulation strategy for the planer motion mechanism tests under the surf-riding condition in following waves is proposed. The mathematical equations to calculate the maneuvering hydrodynamic derivatives in this condition are also provided to analyze the wave effect on the maneuvering components. Then, the course-stability index in waves can be calculated based on the criterion of Routh-Hurwitz and the largest real part of characteristic roots for course stability equations is calculated.
2. The simulation strategy for the captive model tests under the head waves are provided. The overset mesh technique and Euler overlay method are adopted to conduct the simulations. Different from the following wave condition, the Fast Fourier transform (FFT) technique is utilized to separate the low-

frequency and high-frequency components of the monitored hydrodynamic forces. Then, the low-frequency component is utilized to calculate the hydrodynamic derivatives in waves.

3. The dynamic overset mesh method with a structured grid, level-set method, and body force method for the propulsion force simulation are adopted to predict the self-propulsion case, turning maneuver, and zig-zag maneuver in the calm water condition. The results are validated by the experimental data. The flow field information, vortices structures, and the time histories of the forces and motions are obtained.
4. Based on the wave generation and absorption method as well as the region motion control strategy, the course-keeping maneuvers, turning maneuvers, and zigzag maneuvers in regular and irregular waves are simulated. The comparison between the results in the calm water condition and those in waves is also carried out to reveal the wave effect on the maneuverability. The flow field information, vortices structures, and the time histories of the forces and motions are also drawn.

1.4 Thesis layout

The current thesis is organized as follows. Chapter 1 states the general introduction of the present methods on the topic of maneuverability in waves and the research scope and objectives for the present research. Then, the detailed numerical simulation methodologies of the utilized codes, such as the governing equations, the linearization of equations, the overset grid meth method, the body force method, the wave generation method and so on, are presented in Chapter 2. Chapter 3 lays the simulation strategies for simulating captive model tests in following waves. The maneuvering hydrodynamic derivatives and the course-stability index in waves can be calculated based on the monitored forces, which reveal the wave effect on the maneuverability. Next, the simulations for captive model tests in head waves are introduced in Chapter 4. The Fast Fourier transform (FFT) technique is utilized to separate the low-frequency component to detect the wave-effected hydrodynamic derivatives. Then, Chapter 5 is dedicated to the simulation of free-running tests in calm water based on the body force method to predict the propeller force. The results are validated by the experimental data and the flow field information can be obtained. The simulation method and results of free-running tests in regular and irregular waves are introduced in Chapter 6. Finally, Chapter 7 summarized the conclusions of the current thesis and prospects for future research.

Chapter 2 Methodology

Computational Fluid Dynamics, abbreviated as CFD, is leveraged to unveil the hydrodynamic phenomenon of the ship maneuvering in waves in the present dissertation. The governing equations, discretization schemes, the solution algorithms will be introduced in this chapter. It should be noted that there are two codes utilized in the present dissertation, one is Star-CCM+ for the captive model tests simulations in waves (Chapter 3 and 4), the other is Nagisa (Ohashi et al, 2018) for the free-running tests simulations in waves (Chapter 5 and 6). The inherent calculation theories for these codes are similar. Therefore, the methodology of the Nagisa is utilized to describe in this chapter and the differences between these two codes will be specified in Chapter 3.

2.1 Incompossible Reynolds-averaged Navier-Stocks Solver

2.1.1 Governing equations of fluid dynamics

For the general hydrodynamic problem, the governing equations are the incompressible three-dimensional Reynolds-average Navier-Stocks equation which is obtained based on the momentum conservation, and the continuity equation based on mass conservation. A difficulty for the solution of the governing equations is the decoupling of the continuity and momentum equations due to the absence of the pressure term in the former. Nagisa utilizes the artificial compressibility approach (Chorin, 1967) to solve this problem. For the unsteady computation, the dual time steeping method (Jameson, 1991) is applied. Hence, the dimensionless governing equations can be listed as:

$$\frac{\partial \boldsymbol{q}}{\partial t}+\frac{\partial \boldsymbol{q}^{*}}{\partial \tau}+\frac{\partial\left(\boldsymbol{e}-\boldsymbol{e}^{v}\right)}{\partial x}+\frac{\partial\left(\boldsymbol{f}-\boldsymbol{f}^{v}\right)}{\partial y}+\frac{\partial\left(\boldsymbol{g}-\boldsymbol{g}^{v}\right)}{\partial z}-\boldsymbol{H}=0 \quad (2.1)$$

where $\boldsymbol{q}=\left[0\ u\ v\ w\right]^{T}$, $\boldsymbol{q}^{*}=\left[p\ u\ v\ w\right]^{T}$.

This equation is non-dimentionalized by the reference density (fluid density), reference velocity (initial vessel speed) and reference length (ship length). (u,v,w) denote the velocity in *x*, *y*, and *z* directions, respectively.

The convective terms $\boldsymbol{e},\boldsymbol{f},\boldsymbol{g}$, viscous terms $\boldsymbol{e}^{v},\boldsymbol{f}^{v},\boldsymbol{g}^{v}$, and source term $\boldsymbol{H}$ in Eq (2.1) are expressed as:

$$\boldsymbol{e}=\begin{bmatrix}\beta u\\ \left(u-u_{g}\right)u+p\\ \left(u-u_{g}\right)v\\ \left(u-u_{g}\right)w\end{bmatrix},\quad \boldsymbol{f}=\begin{bmatrix}\beta v\\ \left(v-v_{g}\right)u\\ \left(v-v_{g}\right)v+p\\ \left(v-v_{g}\right)w\end{bmatrix},\quad \boldsymbol{g}=\begin{bmatrix}\beta w\\ \left(w-w_{g}\right)u\\ \left(w-w_{g}\right)v\\ \left(w-w_{g}\right)w+p\end{bmatrix},$$

$$\boldsymbol{e}^v=\begin{bmatrix}0\\ \tau_{xx}\\ \tau_{xy}\\ \tau_{xz}\end{bmatrix},\quad \boldsymbol{f}^v=\begin{bmatrix}0\\ \tau_{yx}\\ \tau_{yy}\\ \tau_{yz}\end{bmatrix},\quad \boldsymbol{g}^v=\begin{bmatrix}0\\ \tau_{zx}\\ \tau_{zy}\\ \tau_{zz}\end{bmatrix},\quad \boldsymbol{H}=\begin{bmatrix}0\\ f_x\\ f_y\\ f_z\end{bmatrix} \tag{2.2}$$

where (u_g, v_g, w_g) are moving grid velocities, β is the parameter of the artificial compressibility approach and $\beta = 1.0$ is adopted in the present simulation. For the incompressible Newtown fluid, the viscous stress component τ_{ij} is defined as $\tau_{ij}=\frac{1}{Re}\left(\frac{\partial u_i}{\partial x_j}+\frac{\partial u_j}{\partial x_i}\right)-\overline{u_i'u_j'}$, in which Re represents the Reynolds number $\mathrm{Re}=vl/\nu$, ν is the kinematic viscosity coefficient, and $\overline{u_i'u_j'}$ denotes the Reynolds stress component coming from the Reynolds decomposition.

The pressure p in Eq(2.1) is modified in the following equation for free surface flow:

$$p = p^* + \frac{z}{Fn^2} \tag{2.3}$$

where p^* is the pressure in a computational domain, Fn represents the Froude number, and z denotes the vertical coordinate from the static water plane ($z = 0$). Through the modification, the gravity term is included in the pressure.

The integrational form of Eq(2.1) can be expressed as Eq(2.4) relying on the finite volume method and Gauss integral theorem.

$$\begin{aligned}&\frac{\partial}{\partial t}\iiint_{V_{i,j,k}}\boldsymbol{q}dV+\frac{\partial}{\partial \tau}\iiint_{V_{i,j,k}}\boldsymbol{q}^*dV-\iiint_{V_{i,j,k}}\boldsymbol{H}dV\\&+\oint_{\partial V_{i,j,k}}\left(\left(\boldsymbol{e}-\boldsymbol{e}^v\right)n_x+\left(\boldsymbol{f}-\boldsymbol{f}^v\right)n_y+\left(\boldsymbol{g}-\boldsymbol{g}^v\right)n_z\right)dS=0\end{aligned} \tag{2.4}$$

Finally, the discretized form of the governing equation for a structured grid with a cell-centered layout can be listed as follows:

$$\begin{aligned}&\frac{\partial V_{i,j,k}\boldsymbol{q}_{i,j,k}}{\partial t}+\frac{\partial V_{i,j,k}\boldsymbol{q}^*_{i,j,k}}{\partial \tau}-V_{i,j,k}\boldsymbol{H}_{i,j,k}\\&+\left[\boldsymbol{E}-\boldsymbol{E}_v\right]_{i-1/2}^{i+1/2}+\left[\boldsymbol{F}-\boldsymbol{F}_v\right]_{j-1/2}^{j+1/2}+\left[\boldsymbol{G}-\boldsymbol{G}_v\right]_{k-1/2}^{k+1/2}=0\end{aligned} \tag{2.5}$$

where $\pm 1/2$ represents contrary directions of each cell face, $\boldsymbol{E},\boldsymbol{F},\boldsymbol{G}$ are the convective fluxes, $\boldsymbol{E}_v,\boldsymbol{F}_v,\boldsymbol{G}_v$ are the viscous fluxes whose definition and calculation method will be introduced in the next section.

2.1.2 Convective flux with the moving grid and Viscous flux

For the simulations with a moving grid, the convective flux $\boldsymbol{E}$ can be defined as:

$$\boldsymbol{E}=\begin{bmatrix}\beta U\\ u\left(U-U_g\right)+pS_x\\ v\left(U-U_g\right)+pS_y\\ w\left(U-U_g\right)+pS_z\end{bmatrix} \quad (2.6)$$

where $U=uS_x+vS_y+wS_z$, $U_g=u_gS_x+v_gS_y+w_gS_z$, $\left(S_x,S_y,S_z\right)$ is the face area vector. The convective flux $E_{i+1/2}$ is evaluated using the upwinding scheme based on the flux difference splitting scheme of Roe (1986),

$$\boldsymbol{E}_{i+1/2}=1/2\left[\boldsymbol{E}\left(\boldsymbol{q}^L\right)+\boldsymbol{E}\left(\boldsymbol{q}^R\right)-|\boldsymbol{A}|\left(\boldsymbol{q}^L-\boldsymbol{q}^R\right)\right]_{i+1/2} \quad (2.7)$$

where $\boldsymbol{q}^L$ and $\boldsymbol{q}^R$ are the left and right interface values of $\boldsymbol{q}$ at the $i+1/2$ face, respectively. $\boldsymbol{E}\left(\boldsymbol{q}^L\right)$ and $\boldsymbol{E}\left(\boldsymbol{q}^R\right)$ are calculated by $\boldsymbol{q}^L$, $\boldsymbol{q}^R$ and $i+1/2$ face area vector with grid velocity U_g.

The values $\boldsymbol{q}^L$ and $\boldsymbol{q}^R$ on the $i+1/2$ face are evaluated based on the MUSCL method (Anderson et al, 1986) with the third order upwinding scheme:

$$\boldsymbol{q}^L_{i+1/2}=\frac{2}{6}\boldsymbol{q}_{i+1}+\frac{5}{6}\boldsymbol{q}_i-\frac{1}{6}\boldsymbol{q}_{i-1} \quad (2.8)$$

$$\boldsymbol{q}^R_{i+1/2}=\frac{2}{6}\boldsymbol{q}_i+\frac{5}{6}\boldsymbol{q}_{i+1}-\frac{1}{6}\boldsymbol{q}_{i+2} \quad (2.9)$$

The fluxes of $\boldsymbol{F}$ and $\boldsymbol{G}$ are calculated similarly by replacing the suffix i with j and k, respectively.

For the viscous flux, $\boldsymbol{E}_v$ can be expressed as follows:

$$\boldsymbol{E}_v=\begin{bmatrix}0\\ \tau_{xx}S_x+\tau_{xy}S_y+\tau_{xz}S_z\\ \tau_{xy}S_x+\tau_{yy}S_y+\tau_{yz}S_z\\ \tau_{xz}S_x+\tau_{yz}S_y+\tau_{zz}S_z\end{bmatrix} \quad (2.10)$$

The velocity gradient on a face is calculated using the divergence theorem for the control volume constructed around the face $i+1/2$. The cell center values of i and $i+1$ located at the face center are utilized. Other variables are obtained by interpolation. Second order central scheme is adopted here. The viscous fluxes of $\boldsymbol{F}_v$ and $\boldsymbol{G}_v$ can be

calculated similarly by replacing i with j and k, respectively.

2.1.3 Temporal Discretization

According to the dual time steeping method, the time is discretized into the temporal t and pseudo time τ. The three-level backward differencing is utilized for the discretization of temporal time step (n), and the first order back ward Euler scheme for the pseudo-time step (m). The equations can be listed as follows:

$$\frac{\partial V_i \boldsymbol{q}_i}{\partial t} \approx \frac{3V_{i,j,k}^{(n+1)}\boldsymbol{q}_{i,j,k}^{(n+1)} - 4V_{i,j,k}^{(n)}\boldsymbol{q}_{i,j,k}^{(n)} + V_{i,j,k}^{(n-1)}\boldsymbol{q}_{i,j,k}^{(n-1)}}{2\triangle t} \quad (2.11)$$

$$\frac{\partial V_i \boldsymbol{q}_i^*}{\partial \tau} \approx \frac{V_{i,j,k}^{(n+1)}\triangle \boldsymbol{q}_{i,j,k}^{*(m+1)}}{\triangle \tau} = \frac{V_{i,j,k}^{(n+1)}\left(\boldsymbol{q}_{i,j,k}^{*(m+1)} - \boldsymbol{q}_{i,j,k}^{*(m)}\right)}{\triangle \tau} \quad (2.12)$$

The pseudo-time step process is iterated at each temporal time step to meet the divergence free requirement, and the local time stepping approach is adopted for the pseudo-time step $\triangle\tau$ to obtain fast convergence according to Eq(2.13).

$$\triangle\tau_{i,j,k} = CFL\frac{V_{i,j,k}}{\sum_{faces} 0.5\left(\left|U - U_g/2\right| + c\right)} \quad (2.13)$$

2.1.4 Determination of grid velocity

The grid velocity in x direction $U_{g\,i+1/2}$ is derived from the volume where the face $i+1/2$ sweeps. The swept volume at face $i+1/2$ and time step n is expressed as $\triangle V_{i+1/2}^{n}$, and the time step n+1 is $\triangle V_{i+1/2}^{n+1}$. Then, the grid velocity $U_{g\,i+1/2}$ is obtained as follows:

$$U_{g\,i+1/2} = \frac{3\triangle V_{i+1/2}^{n+1} - \triangle V_{i+1/2}^{n}}{2\triangle t} \quad (2.14)$$

$U_{g\,j+1/2}$ and $U_{g\,k+1/2}$ can be calculated by substituting j and k for i, respectively.

2.1.5 Linearization of equations

The linearization for the convective and viscous fluxes is based on Eq(2.15).

$$\begin{cases} \boldsymbol{E}^{(m+1)} = \boldsymbol{E}^{m} + \dfrac{\partial \boldsymbol{E}^{m}}{\partial \boldsymbol{q}^{*(m)}}\Delta \boldsymbol{q}^{*(m+1)} \\ \boldsymbol{E}_v^{(m+1)} = \boldsymbol{E}_v^{m} + \dfrac{\partial \boldsymbol{E}_v^{m}}{\partial \boldsymbol{q}^{*(m)}}\Delta \boldsymbol{q}^{*(m+1)} \end{cases} \quad (2.15)$$

The convective term in this equation is evaluated using the first order upwind

scheme.

Finally, the linearized and implicit forms of Eq(2.5) can be expressed as follows:

$$
\begin{aligned}
&\left(\begin{array}{l}
\dfrac{3V_{i,j,k}^{(n+1)(m)}}{2\triangle t}+\dfrac{V_{i,j,k}^{(n+1)(m)}}{\triangle\tau_{i,j,k}}+\dfrac{\partial \boldsymbol{E}_{i+1/2}^{(m)}}{\partial \boldsymbol{q}_{i}^{*(m)}}-\dfrac{\partial \boldsymbol{E}_{i-1/2}^{(m)}}{\partial \boldsymbol{q}_{i}^{*(m)}}-\dfrac{\partial \boldsymbol{E}_{v\,i+1/2}^{(m)}}{\partial \boldsymbol{q}_{i}^{*(m)}} \\
+\dfrac{\partial \boldsymbol{E}_{v\,i-1/2}^{(m)}}{\partial \boldsymbol{q}_{i}^{*(m)}}+\dfrac{\partial \boldsymbol{F}_{j+1/2}^{(m)}}{\partial \boldsymbol{q}_{j}^{*(m)}}-\dfrac{\partial \boldsymbol{F}_{j-1/2}^{(m)}}{\partial \boldsymbol{q}_{j}^{*(m)}}-\dfrac{\partial \boldsymbol{F}_{v\,j+1/2}^{(m)}}{\partial \boldsymbol{q}_{j}^{*(m)}}+\dfrac{\partial \boldsymbol{F}_{v\,j-1/2}^{(m)}}{\partial \boldsymbol{q}_{j}^{*(m)}} \\
+\dfrac{\partial \boldsymbol{G}_{k+1/2}^{(m)}}{\partial \boldsymbol{q}_{k}^{*(m)}}-\dfrac{\partial \boldsymbol{G}_{k-1/2}^{(m)}}{\partial \boldsymbol{q}_{k}^{*(m)}}-\dfrac{\partial \boldsymbol{G}_{v\,k+1/2}^{(m)}}{\partial \boldsymbol{q}_{k}^{*(m)}}+\dfrac{\partial \boldsymbol{G}_{v\,k-1/2}^{(m)}}{\partial \boldsymbol{q}_{k}^{*(m)}}
\end{array}\right)\Delta \boldsymbol{q}_{i,j,k}^{*(n+1)(m+1)} \\
&=\left[\boldsymbol{E}^{(m)}-\boldsymbol{E}_{v}^{(m)}\right]_{i-1/2}^{i+1/2}+\left[\boldsymbol{F}^{(m)}-\boldsymbol{F}_{v}^{(m)}\right]_{j-1/2}^{j+1/2}+\left[\boldsymbol{G}^{(m)}-\boldsymbol{G}_{v}^{(m)}\right]_{k-1/2}^{k+1/2}+V_{i,j,k}^{(n+1)}\boldsymbol{H}_{i,j,k} \\
&-\left(\frac{\partial \boldsymbol{E}_{i+1/2}^{(m)}}{\partial \boldsymbol{q}_{i+1}^{*(m)}}-\frac{\partial \boldsymbol{E}_{v\,i+1/2}^{(m)}}{\partial \boldsymbol{q}_{i+1}^{*(m)}}\right)\Delta \boldsymbol{q}_{i+1,j,k}^{*(n+1)(m+1)}+\left(\frac{\partial \boldsymbol{E}_{i-1/2}^{(m)}}{\partial \boldsymbol{q}_{i-1}^{*(m)}}-\frac{\partial \boldsymbol{E}_{v\,i-1/2}^{(m)}}{\partial \boldsymbol{q}_{i-1}^{*(m)}}\right)\Delta \boldsymbol{q}_{i+1,j,k}^{*(n+1)(m+1)} \\
&-\left(\frac{\partial \boldsymbol{F}_{j+1/2}^{(m)}}{\partial \boldsymbol{q}_{j+1}^{*(m)}}-\frac{\partial \boldsymbol{F}_{v\,j+1/2}^{(m)}}{\partial \boldsymbol{q}_{j+1}^{*(m)}}\right)\Delta \boldsymbol{q}_{i,j+1,k}^{*(n+1)(m+1)}+\left(\frac{\partial \boldsymbol{F}_{j-1/2}^{(m)}}{\partial \boldsymbol{q}_{j-1}^{*(m)}}-\frac{\partial \boldsymbol{F}_{v\,j-1/2}^{(m)}}{\partial \boldsymbol{q}_{j-1}^{*(m)}}\right)\Delta \boldsymbol{q}_{i,j+1,k}^{*(n+1)(m+1)} \\
&-\left(\frac{\partial \boldsymbol{G}_{k+1/2}^{(m)}}{\partial \boldsymbol{q}_{k+1}^{*(m)}}-\frac{\partial \boldsymbol{G}_{v\,k+1/2}^{(m)}}{\partial \boldsymbol{q}_{k+1}^{*(m)}}\right)\Delta \boldsymbol{q}_{i,j,k+1}^{*(n+1)(m+1)}+\left(\frac{\partial \boldsymbol{G}_{k-1/2}^{(m)}}{\partial \boldsymbol{q}_{k-1}^{*(m)}}-\frac{\partial \boldsymbol{G}_{v\,k-1/2}^{(m)}}{\partial \boldsymbol{q}_{k-1}^{*(m)}}\right)\Delta \boldsymbol{q}_{i,j,k+1}^{*(n+1)(m+1)} \\
&-\frac{3V_{i}^{(n+1)(m)}\boldsymbol{q}_{i,j,k}^{(n+1)(m)}-4V_{i}^{(n)}\boldsymbol{q}_{i,j,k}^{(n)}+V_{i}^{(n-1)}\boldsymbol{q}_{i,j,k}^{(n-1)}}{2\triangle t}
\end{aligned}
\tag{2.16}
$$

The symmetric Gauss-Seidel (SGS) method is applied to solve this equation.

2.2 Overset grid method

The overset grid method is based on the following steps (Kobayashi and Kodama, 2016).

1. Set the priority of the computational grid. The priority of a small grid is higher than a larger grid which covers it. The lowest priority grid should be the base region grid. For instance, a priority order can be a rudder grid, a rudder overlap grid, a hull grid, and a base grid.
2. Identify the cells of a lower priority grid and those inside a body (named as the in-wall cells herein). For example, the cells of the rudder overlap grid inside the rudder surface are the in-wall cells.
3. Define receptor cells for which the flow variables must be interpolated from donor cells of other grids. Two layers of the cells on a higher priority grid and facing the outer boundary are set as receptor cells to satisfy the third-order discretization of the NS solver. Additionally, two cells that neighbor the in-wall cells, cells of a lower priority grid and cells inside the domain of a higher priority grid are also set as the receptor cells.
4. Calculate the weight values for the overset interpolation by solving the inverse problem based on the Ferguson spline interpolation.

Flow variables of the receptor cell are updated when the boundary condition is set. To eliminate the overlapping region on wall surfaces, the forces and moments are integrated on the higher priority grid. First, the cell face of the lower priority grid is

separated into several small faces. Then, these small faces are projected to the cell face of a higher priority grid based on the normal vector of the higher priority face. The 2D solid angle is calculated and the small face is determined to be inside or outside the higher priority face. The area ratio is zero if the small face is inside the higher priority one. Finally, the area ratio is integrated on the higher priority face, and then used to integrate the forces and moments on the lower priority face.

2.3 Free surface model

The single-phase localized level-set method (Hino, 1999) is applied to capture free surfaces. The level-set function ϕ, representing the signed distance from the interface, near a solid wall region is calculated by solving the following extrapolation equation:

$$\frac{\partial \phi}{\partial \tau} - C_x \frac{\partial \phi}{\partial x} - C_y \frac{\partial \phi}{\partial y} - C_z \frac{\partial \phi}{\partial z} = 0 \quad (2.17)$$

where (C_x, C_y, C_z) are the vectors of the gradient of the distance from a solid wall.

The free surface condition can be approximated using the following two conditions in the single-phase method. First, the velocity gradients normal to the free surface are zero (the kinematic boundary condition). The velocities are extrapolated to the air region ($\phi < 0$) by solving Eq(2.18).

$$\frac{\partial \boldsymbol{q}}{\partial \tau} - C_x \frac{\partial \boldsymbol{q}}{\partial x} - C_y \frac{\partial \boldsymbol{q}}{\partial y} - C_z \frac{\partial \boldsymbol{q}}{\partial z} = 0 \quad (2.18)$$

where (C_x, C_y, C_z) are the tangential vectors near the wall region and the vector of gradient ϕ away from the wall.

Second, the pressure on the free surface is given as atmospheric pressure:

$$p = \frac{Z_c}{Fn^2} \quad \text{on the free surface}$$

where atmospheric pressure is assumed to be zero and Z_c is the z-coordinate of the interface. As shown in Fig 2.1, the closest point on the water-air interface from the cell i is defined as point A and the closest point from the cell $i+1$ is defined as point B. The intersection of the interface and the line connecting the cell centers is expressed as point C. Therefore, Z_c can be calculated by

$$Z_c = \frac{|\phi_i| Z_{i+1} + |\phi_{i+1}| Z_i}{|\phi_i| + |\phi_{i+1}|} \quad (2.19)$$

For the air region, pressure is extrapolated using Eq(2.18).

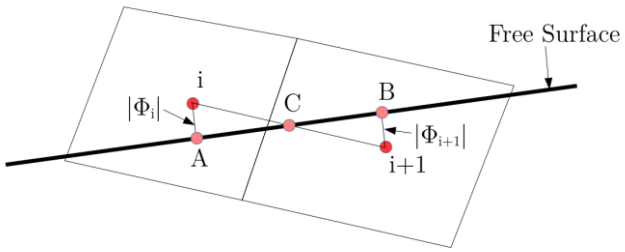

FIGURE 2.1 Pressure condition on a free surface

2.4 Methods to deal with propeller

The body force method based on the potential flow theory (Ohashi, 2018) is adopted. The propeller effect is accounted for by the body forces that are calculated using the following equations:

$$f_x(r,\theta)=\frac{\Gamma(r,\theta)V_\theta}{r}-\frac{1/2\,C_D NC(r)\sqrt{1+\left(h(r)/r\right)^2}V_{ox}V_{o\theta}}{2\pi r} \quad (2.20)$$

$$f_t(r,\theta)=\frac{\Gamma(r,\theta)V_x}{r}+\frac{1/2\,C_D N_c(r)\sqrt{1+\left(h(r)/r\right)^2}V_{o\theta}^2}{2\pi r} \quad (2.21)$$

$$f_y=f_t\cos\theta \quad f_z=f_t\sin\theta \quad (2.22)$$

where r and θ are the cylindrical coordinates at the propeller plane. The propeller circle is divided into fan-shaped segments at (r,θ). $\Gamma(r,\theta)$ is the vortex strength, and $\Gamma(r,\theta)$ is determined using the equation based on the boundary condition at the segment (r,θ). V_x and V_θ are the inflow velocities to the segment, and V_{ox} and $V_{o\theta}$ are the circumferential averaged velocities. C_D is a drag coefficient that is given by the empirical formula, N is the blade number of a propeller, $C(r)$ is a cord length at each radial direction, and $h(r)$ is the pitch of a free stream vortex.

The coupling between the flow field and the propeller model is performed by the velocities V_x and V_θ. First, the velocity at the segment center is interpolated from the computational grid. Then, the $\Gamma(r,\theta)$ is determined, and the body forces are calculated. Finally, the cross-section between the computational grid and the propeller segment is searched, and the forces at the cell are derived by multiplying the body forces and the cross-sectional area. It should be noted that the coordinate transfer is necessary

for motion calculation because of the polar coordinate system utilized here.

2.5 Body motions calculation

Body motions are prescribed (e.g., the rudder motions during the turning circle tests) or calculated by solving the motion equation (e.g., the hull motion). The motion equation in the body-fixed coordinate system is as follows:

$$\begin{cases} m\left(\dot{a}'-b'c'+c'q'\right)=F_{x'} \\ m\left(\dot{b}'-c'p'+a'r'\right)=F_{y'} \\ m\left(\dot{c}'-a'q'+b'p'\right)=F_{z'} \\ I_x\dot{p}'+\left(I_z-I_y\right)q'r'=M_{x'} \\ I_y\dot{q}'+\left(I_x-I_z\right)r'p'=M_{y'} \\ I_z\dot{r}'+\left(I_y-I_x\right)p'q'=M_{z'} \end{cases} \quad (2.23)$$

where m is the system mass, I_x, I_y, I_z represent the products of the mass and the moments of inertia in *x*, *y*, and *z* directions, respectively. a', b', c' denote the nondimensionalized linear velocities, and p', q', r' are the nondimensionalized angular velocities in the body-fixed coordinate system.

The coordinate transformation can be performed using Euler angles (Carrica el al., 2007). The transfer matrix for the linear velocities and forces from the earth-fixed coordinate to the body-fixed coordinate is presented as follows:

$$\begin{bmatrix} \cos\psi\cos\theta & \sin\psi\cos\theta & -\sin\theta \\ -\sin\psi\cos\phi+\sin\phi\sin\theta\cos\psi & \cos\psi\cos\phi+\sin\phi\sin\theta\sin\psi & \sin\phi\cos\theta \\ \sin\theta\sin\psi+\cos\phi\sin\theta\cos\psi & -\cos\psi\sin\phi+\cos\phi\sin\theta\sin\psi & \cos\theta\cos\phi \end{bmatrix} \quad (2.24)$$

For the angular velocities and moments, the transfer matrix from the earth-fixed coordinate to the body-fixed coordinate is defined as follows:

$$\begin{bmatrix} 1 & 0 & -\sin\theta \\ 0 & \cos\phi & \cos\theta\sin\phi \\ 0 & -\sin\phi & \cos\theta\cos\phi \end{bmatrix} \quad (2.25)$$

For example, hydrodynamic forces $\left(F_x, F_y, F_z\right)$ on the earth-fixed coordinate are transformed to the body-fixed coordinate as Eq(2.26).

$$\begin{bmatrix} F_{x'} \\ F_{y'} \\ F_{z'} \end{bmatrix} = \begin{bmatrix} \cos\psi\cos\theta & \sin\psi\cos\theta & -\sin\theta \\ -\sin\psi\cos\phi+\sin\phi\sin\theta\cos\psi & \cos\psi\cos\phi+\sin\phi\sin\theta\sin\psi & \sin\phi\cos\theta \\ \sin\theta\sin\psi+\cos\phi\sin\theta\cos\psi & -\cos\psi\sin\phi+\cos\phi\sin\theta\sin\psi & \cos\theta\cos\phi \end{bmatrix} \begin{bmatrix} F_x \\ F_y \\ F_z \end{bmatrix} \quad (2.26)$$

Hydrodynamic moments $\left(M_x, M_y, M_z\right)$ on the earth-fixed coordinate are similarly transformed.

In turn, for the linear velocities and forces, the transfer matrix from the body-fixed

coordinate to the earth-fixed coordinate can be expressed as follows:

$$\begin{bmatrix} \cos\theta\cos\psi & \sin\phi\sin\theta\cos\psi-\cos\phi\sin\psi & \cos\phi\sin\theta\cos\psi+\sin\phi\sin\psi \\ \cos\theta\sin\psi & \sin\phi\sin\theta\sin\psi+\cos\phi\cos\psi & \cos\phi\sin\theta\sin\psi-\sin\phi\cos\psi \\ -\sin\theta & \sin\phi\cos\theta & \cos\phi\cos\theta \end{bmatrix} \quad (2.27)$$

The transfer matrix for the angular velocities and moments is expressed as follows:

$$\begin{bmatrix} 1 & \sin\phi\tan\theta & \cos\phi\tan\theta \\ 0 & \cos\phi & -\sin\phi \\ 0 & \sin\phi/\cos\theta & \cos\phi/\cos\theta \end{bmatrix} \quad (2.28)$$

The accelerations of the motions can be obtained by solving the motion equation for the body-fixed coordinate, and the velocity $\dot{h}$ representing all components is derived from the following equation:

$$\dot{h}^{n+1} = \dot{h}^{n} + \triangle t \ddot{h}^{n+1} \quad (2.29)$$

The velocity $\dot{h}$ of the body-fixed coordinate is transformed into the earth-fixed coordinate by the previous angular velocities transfer matrices. Then, the displacement of a predictor step is calculated using the third-order Adams-Bashforth scheme:

$$h^{n+1} = h^{n} + \frac{\triangle t}{12}\left(23\dot{h}^{n+1} - 16\dot{h}^{n} + 5\dot{h}^{n-1}\right) \quad (2.30)$$

2.6 Wave generation and absorption method

The incoming waves are generated in a specified region near the boundaries of the calculation domain. As shown in Eq(2.31), the flow variables are calculated by the solution $\boldsymbol{q}_{solved}$ of the RANS code, the theoretical value $\boldsymbol{q}_{wave}$ of the potential flow theory, and the blending function α .

$$\boldsymbol{q} = (1-\alpha)\boldsymbol{q}_{solved} + \alpha\boldsymbol{q}_{wave} \quad (2.31)$$

The level-set function utilized for capturing the free surface is also blended in this designated region as follows:

$$\phi = (1-\alpha)\phi_{solved} + \alpha\phi_{wave} \quad (2.32)$$

where ϕ_{solve} represents the level-set function calculated from the RANS code and ϕ_{wave} is obtained from the wave theory. α is the weight function relying on the distance from the outer boundary and can be expressed as follows:

$$\alpha_x = \begin{cases} 1.0 & x_m \le x \le x_o \\ \sin^n\left(\dfrac{\pi}{2}\dfrac{x-x_b}{x_m-x_b}\right) & x_b \le x \le x_m \end{cases} \quad (2.33)$$

$$\alpha_y = \begin{cases} 1.0 & y_m \le y \le y_o \\ \sin^n\left(\frac{\pi}{2}\frac{y - y_b}{y_m - y_b}\right) & y_b \le y \le y_m \end{cases} \quad (2.34)$$

where x_b and y_b are the coordinates from where the blending region starts. x_o and y_o are the locations of the boundaries. x_m and y_m are the arbitrary locations from where the constant value (1.0) starts.

Chapter 3 Captive model tests in following waves

Restrained by the required large computational resources and long CPU time, the work of the pure CFD simulations on free-running tests in waves are few. Even for the calm water condition, simulations are not widely performed by scholars considering the complex hull-propeller-rudder interaction and the requirement for huge computational resources. The potential flow theory methods, containing the two-time-scale method and the unified method, are widely studied and adopted to predict the loads and motions when ships maneuvers in waves. The viscous maneuvering forces in these mathematical models are calculated by the maneuvering hydrodynamic derivatives obtained from experiments, CFD simulations, or empirical formulas. Simonsen et al (2012) utilized the simulated static PMM data to predict the standard 10/10 and 20/20 zigzag tests and 35deg turning circle maneuvers with good agreement. He et al (2016) replaced the experimental linear hydrodynamic derivatives with computed ones obtained by Star-CCM+ in the MMG mathematical model to simulate the turning and zigzag maneuvers with high accuracy. Relying on the successful simulations in calm water condition, many scholars extended the methods to the wave condition directly. For example, Sadat-Hosseini et al. (2011) adopted the simulated linear and nonlinear hydrodynamic derivatives in calm water to predict the broaching, surf-riding and periodic motion for the ONR Tumblehome model.

So far, most of the hydrodynamic derivatives obtained under the calm water condition are directly utilized in the mathematical model for predicting the maneuvering motions in waves without adjustment. Only one modification is considered in the surge motion, which is the added resistance in waves. The wave effect on the lateral velocity related parameters and yaw angular velocity related parameters are ignored. However, the previous experiments (Hamamoto, 1971, Son and Nomoto, 1982, Bonci et al, 2019) reveal that the wave effect on these hydrodynamic derivatives should not be ignored all the time. Furthermore, some scholars (Reed and Beck, 2008) attribute the unsatisfied prediction results of the potential theory methods to the ignorance of the wave effect on the maneuvering hydrodynamic derivatives. Hence, this chapter is devoted to obtaining the hydrodynamic derivatives under waves through numerical simulations and comparing them with the experimental values for validation. The influence of the wave on hydrodynamic derivatives will be analyzed and discussed.

The relevant research has been started several decades ago. For the experimental research on this topic, the first work might be the research of Hamamoto (1971). To obtain the hydrodynamic derivatives in different relative positions between ship and wave, a flap plate was fixed at the front of the carriage in the towing tank. Then, the wave will be generated behind the plate when the model fixed on the PMM facility is towed by the carriage. Relying on this experimental setup, the relative position between the model and wave can be fixed during the PMM tests. Hence, the hydrodynamic derivatives in waves under the specific relative position between the ship and wave are obtained, which reveals the huge differences between the hydrodynamic derivatives in calm water and waves. Then, Renilson and Driscoll (1981) conducted the similar PMM

tests in following waves in the CWC (Circulating Water Channel). A flap plate is also utilized to generate a wave zone with zero encounter wave frequency to obtain the hydrodynamic derivatives in various wave positions. Following them, Son and Nomoto (1982) conducted PMM tests in waves, and the coupled roll motion was considered for the first time. Recently, Araki et al (2011) performed the captive model tests in following waves to obtain the hydrodynamic derivatives in waves for the purpose of improving the prediction accuracy of the broaching-to phenomenon. However, the prediction accuracy did not change significantly considering the wave effect on hydrodynamic derivatives even though these coefficients varied greatly with the change of relative position between ship and wave. They considered the reason might be the insufficient consideration of parameters in the model, such as the roll-related hydrodynamic derivatives. Bonci et al (2019) carried out captive model tests in following and stern quartering waves to obtain the linear hydrodynamic derivatives. Based on comparisons between the experimental and numerical results, a correction method is proposed and used to predict the broaching-to phenomenon.

However, the previous research is limited on the experimental method. There seem few CFD simulations on this topic. Considering economy and efficiency, the numerical simulations of the captive model tests in following waves are performed in this chapter. Furthermore, the flow field information can be obtained through the CFD methods. Some contents of this chapter were published in the paper of the author (Ma et al, 2021).

3.1 Simulation conditions

The target ship model is the containership S175 (SR108) because it is one of the benchmark models for researching the maneuverability in waves according to ITTC (ITTC, 2017b) and the experimental data of this model is available. To compare with experimental results published by Son and Nomoto (1982), the same ship model scale of 1/58.33 is adopted. The principal particulars and geometry of the model-scaled ship are shown in Table 3.1 and Fig 3.1, respectively.

To obtain the hydrodynamic derivatives in waves, PMM tests are carried out under the surf-riding condition in regular following waves. The surf-riding condition denotes that the ship has the same velocity as the wave celerity in the direction of wave propagation, in other words, the relative position between the ship gravity center and the wave is stationary. In the present research, mainly four typical relative positions of the ship gravity center on the wave are considered, where the gravity center of the ship locates on the wave crest, up-slope, down-slope and wave trough. Fig 3.2 illustrates the definition of the four relative positions of ship and wave. Obviously, $\xi_G/\lambda = 0 \text{ or } 1$ represents that the gravity center of the ship locates on the wave trough, $\xi_G/\lambda = 0.25$ up-slope, $\xi_G/\lambda = 0.5$ crest and $\xi_G/\lambda = 0.75$ down-slope, where λ is the wavelength and ξ_G represents the longitudinal position of the ship gravity center. To evaluate the

wave effect on hydrodynamic derivatives systematically, all four typical relative positions are simulated.

FIGURE 3.1 Geometric model of the S175 containership with a rudder

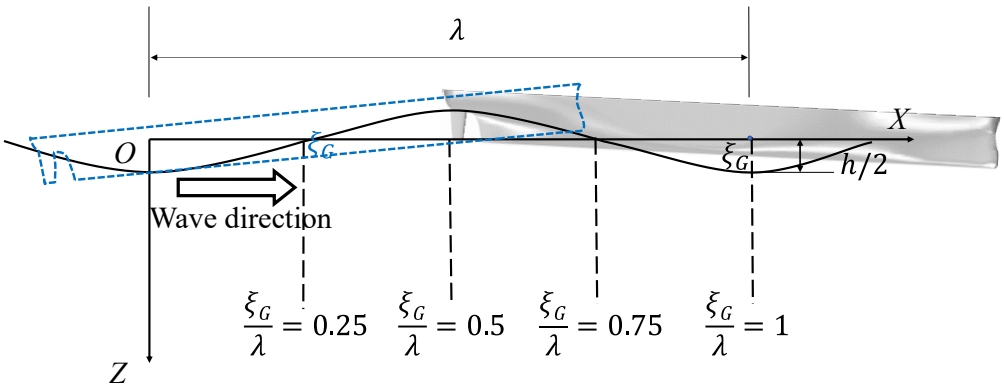

FIGURE 3.2 Relative positions between the ship and wave

TABLE 3.1 Principal particulars of S175 with a rudder

Specifications	Full scale	Model
Length between perpendiculars (m)	175	3.00
Beam (m)	25.4	0.435
Draft (m)	8.5	0.1457
Block coefficient	0.559	0.559
L.C.B. from F.P. (m)	90.65	1.554
Radius of gyration about z-axis (m)	42	0.72
Height of C.G. above base line (m)	\	0.1290
Height from keel to transverse metacenter KM(m)	10.39	0.1781
Height from keel to center of buoyancy KB (m)	4.6154	0.07912
Displacement (m^3)	21222	0.10686
Rudder height(m)	7.7583	0.133

It should be noticed that the definition of the surf-riding condition in the present captive model tests is a little different from that in the free-running tests. In the latter, the surf-riding condition is a phenomenon when a ship traveling in the following sea is captured by the wave and forced to move at the same speed as the wave celerity. The horizontal motions are free which might change rapidly, and this unstable phenomenon might cause the capsizal named as broaching-to. For the present simulated captive model tests, the horizontal motions (surge-sway-yaw) are predetermined, which makes the horizontal motions during the surf-riding condition somewhat different from those

in the free-running tests. Nevertheless, for the hydrodynamic derivatives in the surf-riding condition obtained through the PMM tests, the differences between the definition of the surf-riding condition in the free-running tests and that in the captive model tests do not affect the results. Therefore, the characterization of "surf-riding" for the ship conditions representing the same vessel speed as the wave celerity is acceptable, which is also accepted by other scholars (Motora et al, 1981, Son and Nomoto, 1982).

Two right-handed coordinate systems, i.e., the earth-fixed cartesian system $O_0-X_0Y_0Z_0$ and the ship-fixed cartesian system $G-XYZ$, are used to solve the maneuvering motion equations, as shown in Fig 3.3. In the ship-fixed system, the 3 DOF maneuvering motion equations can be expressed as Eq(3.1) relying on the rigid body motion functions and the velocity transformation between two coordinate systems:

$$\begin{cases} \left(m+m_x\right)\dot{u}-\left(m+m_y\right)vr=X_H+X_W \\ \left(m+m_y\right)\dot{v}+\left(m+m_x\right)ur=Y_H+Y_W \\ \left(I_z+J_z\right)\dot{r}=N_H+N_W \end{cases} \quad (3.1)$$

where m stands for the ship mass, m_x and m_y are the added mass in X and Y directions, respectively. I_z represents the moment of inertia around the z-axis, and J_z is the added moment of inertia around the Z-axis, u and v are ship longitudinal and lateral speed in the ship-fixed system, r is the ship yaw rate around the gravity center of the ship, X, Y, N are the forces and moment in longitudinal, lateral, and yaw directions, the subscripts H and W represent the hull and wave forces.

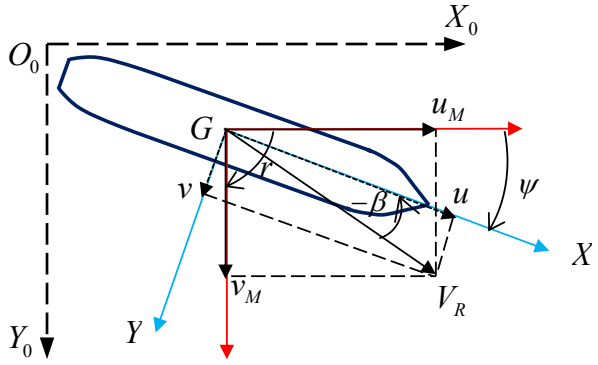

FIGURE 3.3 Coordinate systems utilized for the PMM test simulations in waves

To compare with the experimental data and simplify the problem, we take the same assumption as Son and Nomoto (1982) did that the hydrodynamic derivatives are linear ignoring the nonlinear and coupling hydrodynamic derivatives. The wave forces can be expressed as the linear function of the incident wave angle χ because the wave force component is constant in this condition and this assumption is also be used by other scholars (Araki et al, 2011). Then, Eq(3.1) can be transferred into Eq(3.2) by linear expansion.

$$\begin{cases} \left(m+m_y\right)\dot{v}+\left(m+m_x\right)ur=Y_v v+Y_r r+Y_\chi \chi \\ \left(I_z+J_z\right)\dot{r}=N_v v+N_r r+N_\chi \chi \end{cases} \quad (3.2)$$

Due to the linear assumption, only the oblique towing tests and the pure yaw tests should be simulated to obtain hydrodynamic derivatives in Eq(3.2).

For the oblique towing tests, the simulation conditions are shown in Table 3.2. The motion definition is illustrated in Fig 3.4. The ship is moving straight ahead with a constant drift angle. Meanwhile, the wave celerity is equal to the vessel longitudinal speed u_M, which makes the relative position stationary.

For the pure yaw tests, the simulation conditions are summarized in Table 3.3. The motion definition is illustrated in Fig 3.5. The ship is moving ahead with a yaw angular velocity, which makes the lateral velocity component in the ship-fixed coordinate system equals zero. The motions can be expressed as follows.

$$\begin{cases} v_M=-y_{\max}\omega\cos\left(\omega t\right) \\ r=\dfrac{\varepsilon\omega}{1+\varepsilon^2\cos^2\left(\omega t\right)}\sin\left(\omega t\right) \end{cases} \quad (3.3)$$

where $\varepsilon=y_{\max}\omega/u_M$, u_M is the vessel longitudinal speed in the earth-fixed coordinate system which equals the wave celerity. In addition, the wave incidence angle χ is the same as the yaw angle ψ, which is easy to obtain that $r=\dot{\psi}=\dot{\chi}$. Considering the extremely small value of ε, we regarded $\dfrac{\varepsilon\omega}{1+\varepsilon^2\cos^2\left(\omega t\right)}$ as a constant as Son and Nomoto (1982) did. Then, the coefficients in Eq(3.3) can be expressed as follows.

$$\begin{cases} \chi=-\chi_0\cos\left(\omega t\right) \\ r=r_0\sin\left(\omega t\right) \\ \beta=\dot{\beta}=0 \end{cases} \quad (3.4)$$

where the χ_0 is the maximum incident wave angle, r_0 is the maximum yaw angular velocity.

For the present simulations, the model speed is 2.4 m/s corresponding to the Froude number of 0.443 which is the same as the experimental data. The wave parameters in simulations are $\lambda/L=1.0$ and $h/\lambda=0.0625$, which are in accordance with the experimental data. The initial position should be precalculated to ensure the correct position of the gravity center of the ship on the wave. The heave and pitch motion in all simulations are free.

TABLE 3.2 Simulation conditions for oblique towing tests

Drift angle (deg)	Relative positions between the ship and the wave ξ_G/λ
0, -2, -4	Trough, Up-slope, Down-slope, Crest

TABLE 3.3 Simulation conditions for pure yaw tests

y_{max} (m)	Oscillation frequency ω(1/s)	Maximum yaw angular velocity r_0 (1/s)	ξ_G/λ
0.1	0.6283	0.0104	Trough, Up-slope, Down-slope, Crest
0.2	0.6283	0.0208	
0.3	0.6283	0.0311	

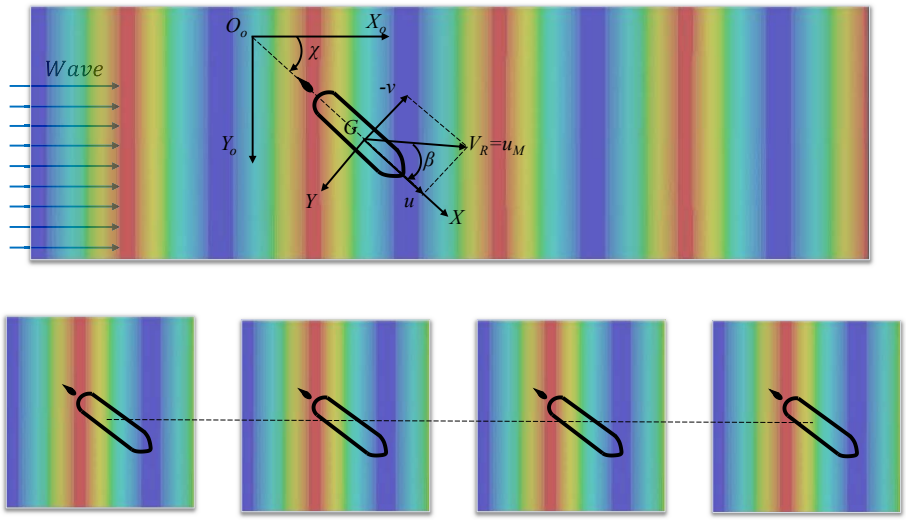

FIGURE 3.4 Schematic diagram of the oblique towing test

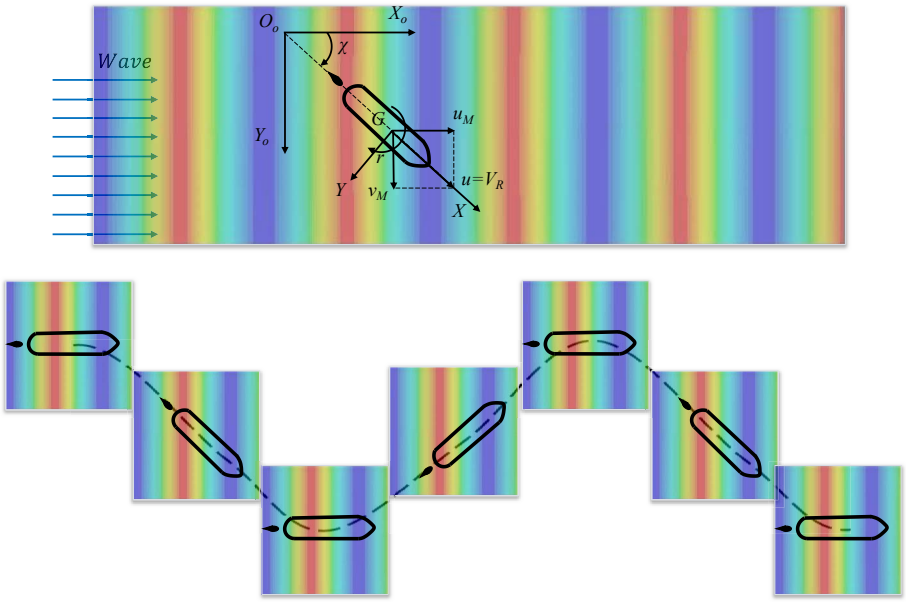

FIGURE 3.5 Schematic diagram of the pure yaw test

3.2 Simulation method

There are some differences between the simulation method of the Star-CCM+ utilized in this Chapter and the method introduced in Chapter 2. For the solution method of the government equations, the method in this chapter adopts the SIMPLE (Semi-Implicit Method for Pressure Linked Equations (Patankar, 1981)) method rather than the artificial compressibility approach.

Considering the huge wave steepness and possible green water phenomenon, the two-phase VOF method is adopted to capture the free surface rather than the single-phase level-set method. The method for wave generation and absorption is also different. To avoid the reflection of the ship wave and minimize the calculation domain, the Euler overlay method (Kim et al, 2012) is utilized on the inlet, outlet, and side boundaries. For the six surfaces of the cubic computation domain, the velocity-inlet boundary condition is applied to five surfaces except the upside one where the pressure-outlet boundary condition is used. As is shown in Fig 3.6, for the Euler overlay method, a new source term is added to the transport equations in the form of Eq(3.5) for the purpose of transfering the solution of internal RANS solver to that of a potential flow theory solver on the boundary smoothly.

$$f_i = -\gamma\rho\left(u_i - u_i^*\right) \quad (3.5)$$

where the coefficient γ satisfies the equation $\gamma = -\gamma_0 \cos^2\left(\pi x/2\right)$, u_i is the current solution of the transport equation and u_i^* is the value towards which the solution is forced.

As for the wave type, the fifth order stokes wave is adopted because it is closer to the actual generated wave under the high wave steepness condition ($h/\lambda = 0.0625$). The simulated wave evaluation around the ship model is monitored and validated by the theoretical data based on the Stokes theory of waves. The comparison result shown in Fig 3.7 reveals the accuracy of the present simulation strategy for wave generation.

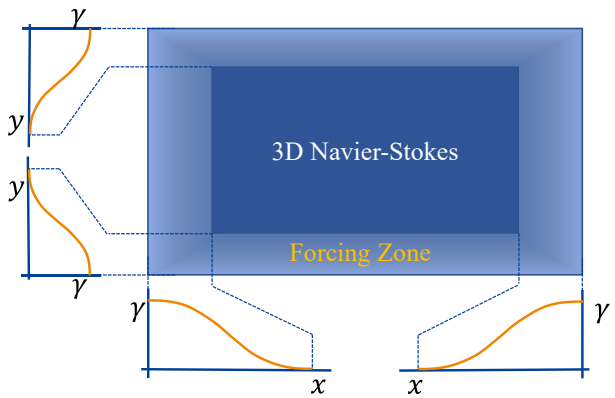

FIGURE 3.6 Euler overlay method illustration

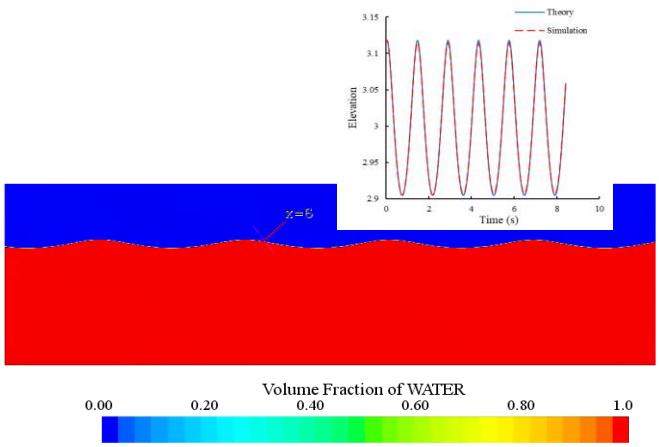

FIGURE 3.7 Comparison of the computational and theoretical wave elevation (x=6m)

3.3 Computational domain and Grids

To conduct the PMM motions simulation under the surf-riding condition, the whole calculation domain should be divided into two parts, which are the overset region and the background region. As shown in Fig 3.8, the background domain extends to $-2.5L<x<2.0L$, $-1.5L<y<1.5L$, and $-1.0L<z<0.8L$. The overset mesh region has the same motions as the ship, i.e., the PMM motion together with the pitch and heave motions. The background region moves with the ship to minimize the calculation domain by setting the same longitudinal and lateral velocities as the ship. Considering better maintaining the stability of the flow field, the background region will not rotate with the same yaw angular velocity as the ship model in present study.

To capture the motion and wave accurately, the grid near the ship and free surface should be refined. The total grid number for the oblique towing tests and the pure yaw tests is around 8 million, where the background grid varies with different lateral distances of different pure yaw test simulation cases. For the case with larger maximum lateral distance, the overlap region should be larger making the total grid number larger.

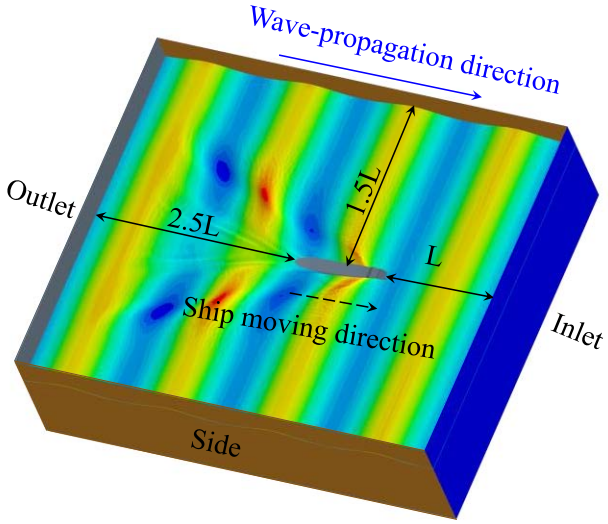

FIGURE 3.8 Illustration of the calculation domain

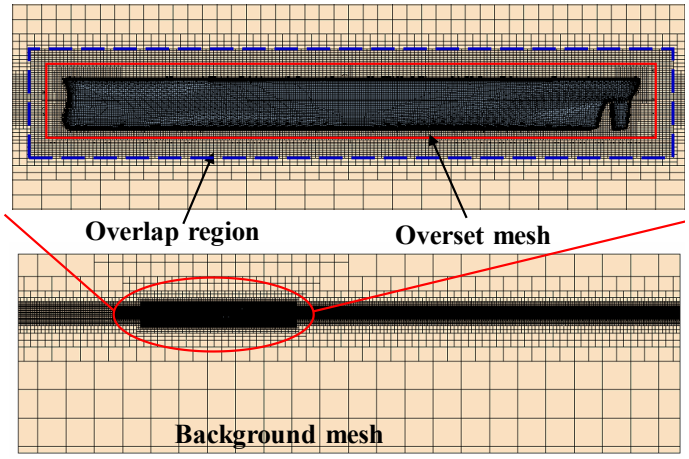

FIGURE 3.9 Overset grid and the finer mesh around the free surface

3.4 Verification

The verification and validation for the numerical simulation method should be conducted for determining the uncertainty. Restrained by the unprovided experimental data for the time histories of the forces, the validation of forces and moments during the PMM tests is not conducted. However, the calculated hydrodynamic derivatives using the forces can be validated by the experimental data in next section. The V&V process is carried out according to ITTC 7.5-03-01-01 (ITTC, 2017a).

For the oblique towing tests, the lateral forces and yaw moments are utilized to verify the grid convergency and calculate the grid uncertainty. The oblique towing test chosen to conduct the uncertainty analysis is the case in which the gravity center locates on the up-slope position with a -4 deg drift angle. The mesh of the calculation domain is generated based on a base size, which means that the base size will determine the whole mesh of the calculation domain. Therefore, we generated three meshes referred to as fine (S1), medium (S2), and coarse (S3) based on the refinement ratio (r_G) of $\sqrt{2}$. The results of grid convergence are shown in Table 3.4.

In this table, $\varepsilon_{21}=S_2/S_1-S_1/S_1$ and $\varepsilon_{32}=S_3/S_1-S_2/S_1$ stand for the changes between medium-fine solutions and coarse-medium solutions, respectively. Then, the convergence ratio R_G can be defined as ε_{21} divided by ε_{32} . Three convergence conditions are possible: (i) Monotonic convergence (MC): $0<R_G<1$; (ii) Oscillatory convergence (OC): $R_G<0$; (iii) Divergence: $R_G>1$. For condition (i), generalized Richardson extrapolation (RE) is utilized to estimate the grid uncertainty U_G and simulation numerical error due to the grid δ_{RE_G} . For condition (ii), uncertainties are

obtained from the oscillation maximum S_U and minimum S_L, i.e., $U_G = \frac{1}{2}(S_U - S_L)$. More than three cases should be conducted if the condition (ii) is used. For condition (iii), errors and uncertainties cannot be estimated. In the present study, only three solutions using different grid sizes are performed. Therefore, the order of accuracy p_G can be defined as $p_G = \frac{\ln(\varepsilon_{32} - \varepsilon_{21})}{\ln(r_G)}$ and the estimate for error is $\delta_{RE_G} = \frac{\varepsilon_{21}}{r_G^{p_G} - 1}$.

As is clearly shown in Table 3.4, for simulations on oblique towing tests in waves, the lateral force shows monotonic convergence (MC) and the predicted value achieves satisfactory accuracy with the uncertainty of 0.176%. The yaw moment shows oscillatory convergence (OC) with the uncertainty of 3.779%. This chart indicates that the grid density for present generated grid has a slight influence on the hull forces. In addition, the yaw moment is more sensitive to the grid compared with the lateral force for the oblique towing tests which might be due to the small value.

Different from the steady forces during oblique towing tests, the lateral force and yaw moment during the pure yaw tests are sinusoidal rather than constant. According to ITTC guidance (ITTC, 2017a) and the time histories of forces, the Fourier series are adopted to express the forces as shown below.

$$\left.\begin{aligned} Y_{CFD} &= Y_1 \cos \omega t + Y_2 \sin \omega t \\ N_{CFD} &= N_1 \cos \omega t + N_2 \sin \omega t \end{aligned}\right\} \quad (3.6)$$

Therefore, we can conduct uncertainty analysis through these coefficients Y_1, Y_2, N_1, and N_2. Table 3.5 shows that all the lateral force components and yaw moment components are monotonic convergent. Contrary to the results of oblique towing tests, the lateral forces in pure yaw tests seem to be more sensitive to the grid with the highest error of 14.45%. All the coefficients are convergent which reveals that the numerical simulation grid is acceptable.

TABLE 3.4 Grid convergence study of oblique towing tests

	Y	N
S_1	33.6	17.2
S_2	33.5	16.5
S_3	33.2	17.5
ε_{21}	-0.0030	-0.0407
ε_{32}	-0.0089	0.0581
R_G	0.33	-0.70
Convergence	MC	OC
p_G	3.169925	/
δ_{RE_G}	-0.05004	/
U_G	0.059085	0.65
U_G (%S_1)	0.176	3.779

TABLE 3.5 Grid convergence study of pure yaw tests

	Y_1	Y_2	N_1	N_2
S_1	3.892	-2.722	-0.940	13.010
S_2	3.916	-3.106	-1.073	13.620
S_3	6.331	-3.865	-4.032	14.850
ε_{21}	0.0062	0.1411	0.1414	0.0469
ε_{32}	0.6205	0.2788	3.1475	0.0945
R_G	0.0099	0.5059	0.0449	0.4959
Convergence	MC	MC	MC	MC
p_G	13.306	1.966	8.953	2.024
δ_{RE_G}	0.0002	-0.3934	-0.006	0.601
U_G	0.0002	0.3934	0.006	0.606
U_G (%S_1)	0.01	-14.45	0.7	4.7

3.5 Results and discussions

Based on the previous verification, the grid is acceptable for its small uncertainty. Then, systematical simulations of oblique towing tests and pure yaw tests are performed and the hydrodynamic derivatives in following waves can also be calculated and validated by experimental data. The simulations for predicting the hydrodynamic derivatives in calm water is also carried out to compare with those in waves. The detailed setup for the simulations in the calm water condition can refer to the previous work of the authors (Ma et al, 2019). By comparison, the wave effect on the linear hydrodynamic derivatives can be evaluated. The course stability in waves can also be analyzed to determine the reason for the occurrence of the broaching-to phenomenon.

3.5.1 Hydrodynamic derivatives obtained from oblique towing tests

The monitored hydrodynamic forces from the numerical simulations include the added mass component (inertia force $m_y\dot{v}+m_xur$ and $J_z\dot{r}$), viscous maneuvering forces (Y_vv+Y_rr and N_vv+N_rr), and wave forces ($Y_\chi\chi$ and $N_\chi\chi$). Therefore, the lateral force Y_{CFD} and yaw moment N_{CFD} monitored in numerical simulations can be expanded as follows.

$$\begin{cases} Y_{CFD}=\left(Y_vv+Y_rr+Y_\chi\chi\right)-m_y\dot{v}-m_xur \\ N_{CFD}=\left(N_vv+N_rr+N_\chi\chi\right)-J_z\dot{r} \end{cases} \quad (3.7)$$

For oblique towing tests, the lateral velocity in the ship-fixed coordinate system is constant and the yaw angular velocity is zero, which can be expressed as $\dot{v}=r=\dot{r}=0$.

Hence, Eq(3.7) can be simplified as Eq(3.8).

$$\begin{cases} Y_{CFD} = Y_v v + Y_\chi \chi \\ N_{CFD} = N_v v + N_\chi \chi \end{cases} \quad (3.8)$$

The non-dimensional variables are shown below:

$$\begin{cases} Y'_{CFD} = \dfrac{Y_{CFD}}{1/2\,\rho U^2 L^2} \quad N'_{CFD} = \dfrac{N_{CFD}}{1/2\,\rho U^2 L^3} \\ v' = v/U \quad r' = rL/U \quad \beta' = \beta \quad \chi' = \chi \end{cases} \quad (3.9)$$

Due to the relationship between the drift angle and dimensionless lateral velocity $\beta = \sin(-v/U) \approx -v/U = -v'$, the dimensionless equations can be expressed as follows by combining Eq(3.8) and Eq(3.9).

$$\begin{cases} Y'_{CFD} = Y'_\beta \beta' + Y'_\chi \chi' = Y'_{\beta^*} \beta^{*\prime} \\ N'_{CFD} = N'_\beta \beta' + N'_\chi \chi' = N'_{\beta^*} \beta^{*\prime} \end{cases} \quad (3.10)$$

where β^* is of the same physical meaning and value as β. The reason for choosing different symbols is to distinguish whether the wave forces are considered.

After a series of simulations, the lateral forces and yaw moments in different drift angles in various relative positions are calculated. The lateral-velocity-related hydrodynamic derivatives Y'_{β^*} and N'_{β^*}, which are the slopes of the force-fitting lines, can be obtained by the regression of these forces. Fig 3.10 shows the fitting curve and the regression formula of N'_{β^*} when the ship gravity center locates on the wave crest ($\xi_G/\lambda = 0.5$). The hydrodynamic derivatives in other relative positions between the ship and the wave can be obtained in the same way. The results are summarized in Table 3.6 and drawn in Fig 3.11. The error between the predicted derivatives and the experimental ones shows that the simulated lateral forces agree well with the experimental results. However, when the ship gravity center locates on the up-slope condition and the wave trough, the predicted value N'_{β^*} is not quite close to the experimental results. The errors mainly come from two aspects. On the one hand, there is quite serious green-water phenomenon during the simulations of the PMM tests in following waves. In Fig 3.12, we can notice that there is a serious green-water phenomenon when the gravity center locates on the up-slope condition (Fig 3.12(b)) and the wave trough condition (Fig 3.12(c)), in which the errors are huge. On the other hand, the yaw moment when the gravity center locates on the wave trough is so small that a small difference in the flow field will cause a large relative error. However, the absolute error is not significant. In addition, Fig 3.11 also indicates that the variation trend and numerical value of hydrodynamic derivatives obtained from the simulation are in good agreement with the experimental ones.

Fig 3.11 illustrates that Y'_{β^*} and N'_{β^*} fluctuate in an approximately sinusoidal form around their calm-water values with the change of the relative position ξ_G/λ. In Fig 3.11(a), when the gravity center locates on the up-slope position, Y'_{β^*} reaches the maximum value. On the down-slope position, it reaches the minimum value. The maximum value is 77% larger than the minimum value. On the contrary, N'_{β^*} has a contrary tendency. The maximum value occurs on the down-slope position and the minimum value on the up-slope position. Compared with Y'_{β^*}, N'_{β^*} fluctuates more significantly. The maximum value of N'_{β^*} is 4.5 times of the minimum value. It is revealed that the hydrodynamic derivatives in regular waves change significantly. Thus, the wave effect on the maneuvering hydrodynamic derivatives cannot be ignored under this condition. Furthermore, it illustrates that the yaw moments induced by the drift angle change more rapidly compared with the lateral forces induced by the drift angle.

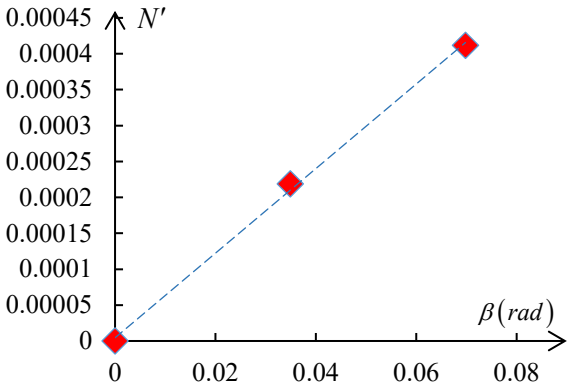

FIGURE 3.10 Curve fitting of the N'_{β^*} with ξ_G/λ=0.5

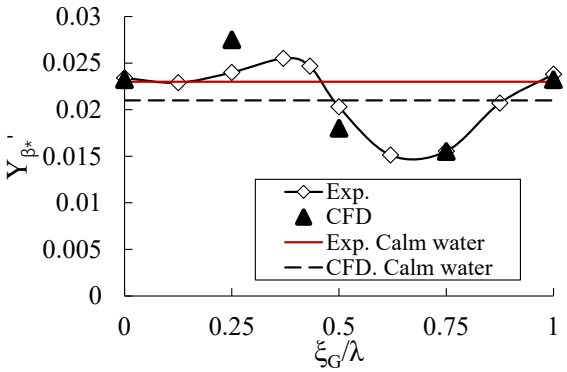

(a)

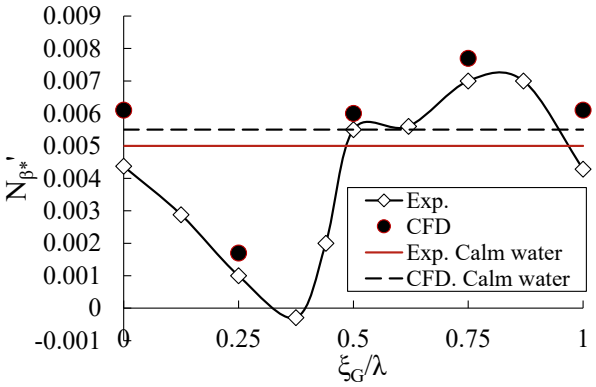

(b)

FIGURE 3.11 Comparison of hydrodynamic derivatives in calm water and regular following waves (a) Y'_{β^*} (b) N'_{β^*}

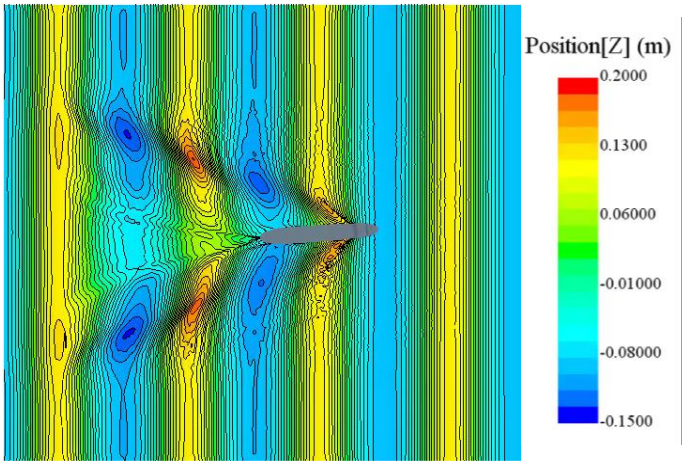

(a)

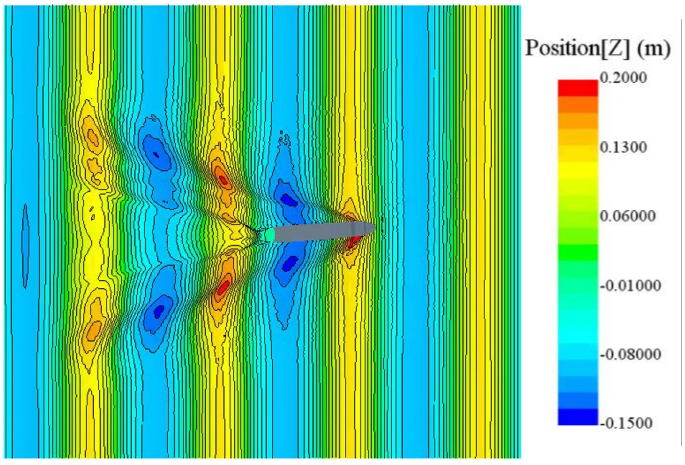

(b)

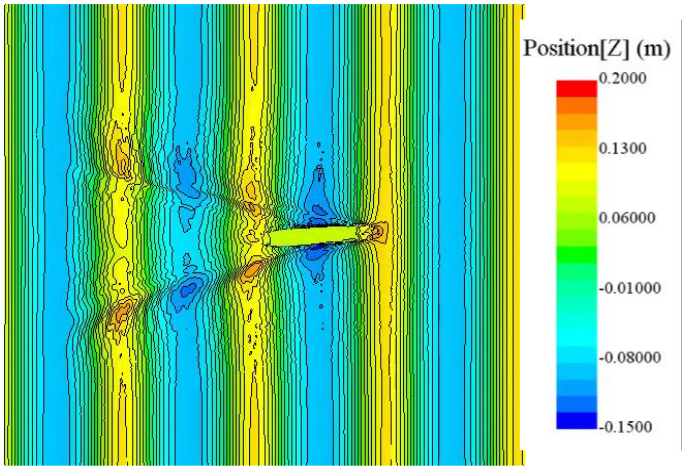

(c)

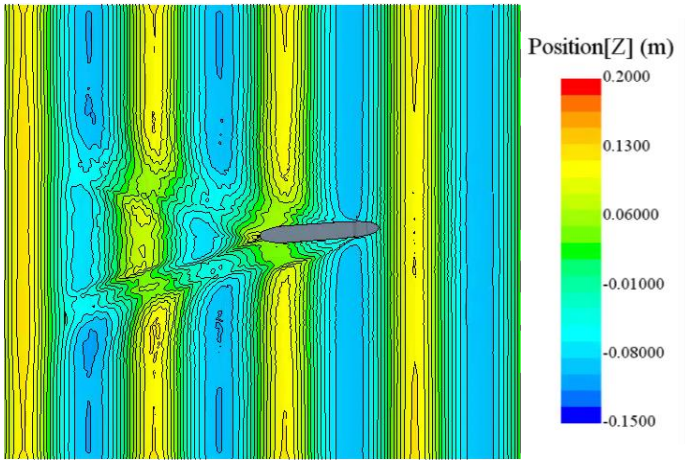

(d)

FIGURE 3.12 Free surface captured for oblique towing tests in regular following waves (β=-4°) (a) crest (b) up-slope (c)wave trough (d) down-slope

Fig 3.12 shows the contour maps of wave elevation with different relative positions between the ship and the wave. The generated Kelvin waves in these pictures are similar but the obvious green-water phenomenon occurs when the ship gravity center locates on the wave trough. In addition, the cases with obvious trim by stern (Fig 3.12 (a) and (b)) have larger wave elevations of the Kelvin waves.

The contour maps of wave elevation with different drift angle when the gravity center locates on the wave crest are provided in Fig 3.13. The asymmetry of the flow field induced by the drift angle causes lateral forces and yaw moments. For the condition with a larger drift angle, the wave height range will be wider.

Fig 3.14 shows the dynamic pressure on the hull in various drift angles when the gravity center locates on the wave crest. The differences between the port side and starboard side can be seen clearly. For example, the red dotted rectangles show the differences between the bow and the parallel middle body near the stern. The dynamic pressure on the port side is larger than that on the starboard on the bow of the ship. However, when it comes to the parallel middle body near the stern, the dynamic pressure on the port side is much smaller than that on the starboard. With the increasing

drift angle, the differences will be much more obvious. Fig 3.15 shows the dynamic pressure on the hull with a constant drift angle $\beta = 4^o$ on various relative positions. On different relative positions, the distribution areas and the intensity of the dynamic pressure values are totally different.

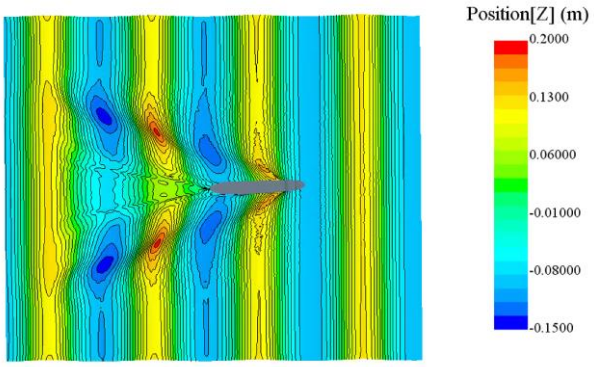

(a)

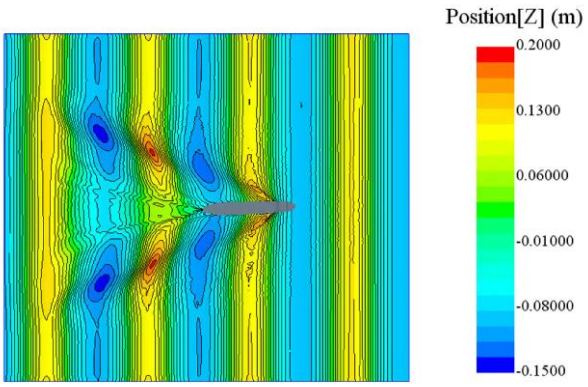

(b)

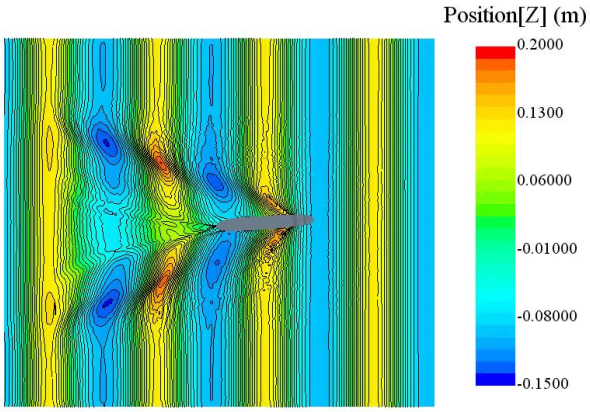

(c)

FIGURE 3.13 Free surface captured for oblique towing tests in regular following waves ($\xi_G/\lambda = 0.5$) (a) β=0° (b) β=-2° (c) β=-4°

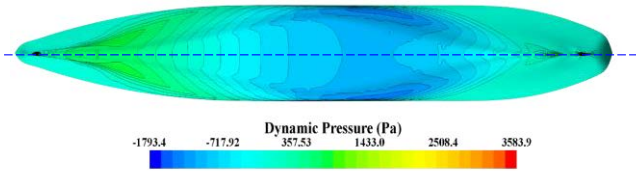

(a)

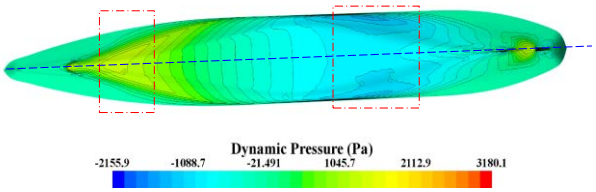

(b)

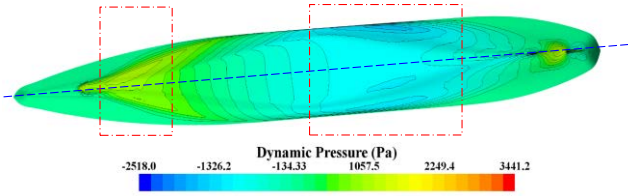

(c)

FIGURE 3.14 Dynamic pressure distribution on the hull ($\xi_G/\lambda = 0.5$)

(a) β=0° (b) β=-2° (c) β=-4°

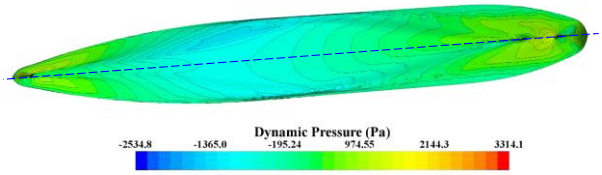

(a)

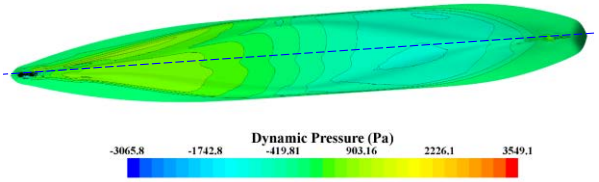

(b)

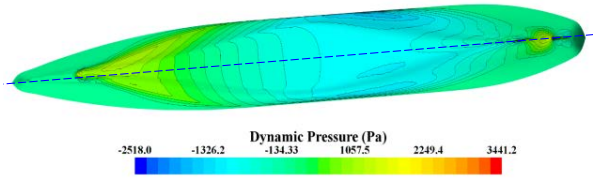

(c)

FIGURE 3.15 Dynamic pressure distribution on the hull ($\beta = -4^o$)

(a) $\xi_G/\lambda = 0.75$ (b) $\xi_G/\lambda = 0.25$ (c) $\xi_G/\lambda = 0.5$

TABLE 3.6 Comparison of derivatives in regular following waves obtained from CFD and experiments

Relative position	Derivatives	CFD	Experiment	Error
Wave crest	$Y'_{\beta*}$	0.0180	0.0203	-11%
	$N'_{\beta*}$	0.0059	0.0055	7%
Down-slope	$Y'_{\beta*}$	0.0155	0.0155	0%
	$N'_{\beta*}$	0.0077	0.0070	10%
Up-slope	$Y'_{\beta*}$	0.0275	0.0240	15%
	$N'_{\beta*}$	0.0017	0.0010	70%
Wave trough	$Y'_{\beta*}$	0.0232	0.0238	-3%
	$N'_{\beta*}$	0.0061	0.0043	42%

3.5.2 Hydrodynamic derivatives obtained from pure yaw tests

The ship conducts pure yaw tests with the same forward speed as the wave celerity to realize the surf-riding condition. The motion control is set according to Eq(3.4) to obtain the linear yaw-rate-related hydrodynamic derivatives Y'_r and N'_r. In these simulations, the lateral velocity component is zero, which means $\dot{v} = v = 0$. Therefore, the Eq(3.7), which are the forces obtained by the numerical simulations, can be simplified as below:

$$\begin{cases} Y_{CFD} = -m_x ur + Y_r r + Y_\chi \chi \\ N_{CFD} = -J_z \dot{r} + N_r r + N_\chi \chi \end{cases} \quad (3.11)$$

Substituting the Eq(3.4) into this expression, we can obtain

$$\begin{cases} Y_{CFD} = (Y_r - m_x u) r_o \sin(\omega t) - Y_\chi \chi_o \cos(\omega t) \\ N_{CFD} = -J_z r_o \omega \cos(\omega t) - N_\chi \chi_o \cos(\omega t) + N_r r_o \sin(\omega t) \end{cases} \quad (3.12)$$

Based on Eq(3.9), the dimensionless equations can be expressed as follows:

$$\begin{cases} Y'_{CFD} = (Y'_r - m'_x u') r_o \sin(\omega t) - Y'_\chi \chi_o \cos(\omega t) \\ N'_{CFD} = -J'_z r_o \omega \cos(\omega t) - N'_\chi \chi_o \cos(\omega t) + N'_r r_o \sin(\omega t) \end{cases} \quad (3.13)$$

By the Fourier series expansion, the forces can be expressed as follows:

$$\begin{cases} Y'_{CFD} = Y_1 \cos \omega t + Y_2 \sin \omega t \\ N'_{CFD} = N_1 \cos \omega t + N_2 \sin \omega t \end{cases} \quad (3.14)$$

By comparison of the Eq(3.13) and Eq(3.14), it is easy to get the following equations:

$$\begin{cases} Y'_{\chi}\chi_0 = Y_1 \\ (m'u' - Y'_r)r_0 = Y_2 \\ J'_z r_0\omega + N'_{\chi}\chi_0 = N_1 \\ -N'_r r_0 = N_2 \end{cases} \quad (3.15)$$

Through Eq(3.15), the hydrodynamic derivatives $Y_{\chi}, N_{\chi}, Y_r, N_r$ can be obtained by fitting in a Fourier series form. For example, Fig 3.16 shows the time histories of lateral force and yaw moment in the specific condition where $\xi_G/\lambda = 0.25$ and maximum yaw angular velocity is set as 0.0208 rad/s. By Fourier series expansion and curve fitting techniques, the hydrodynamic derivatives under the surf-riding condition can be obtained.

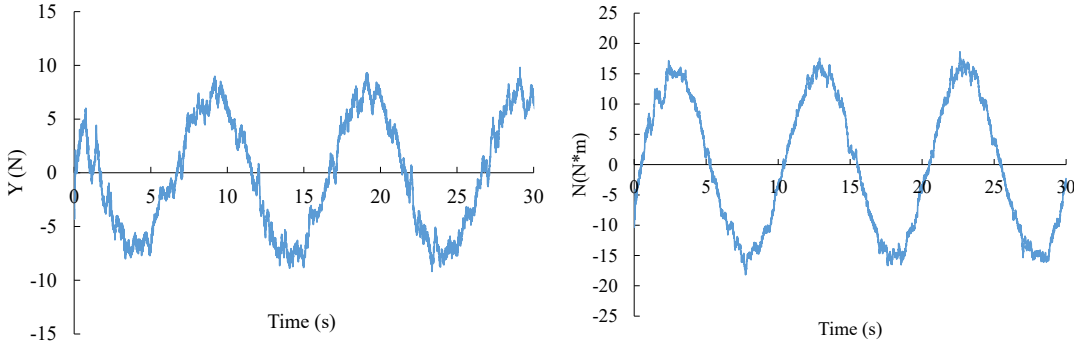

(a) (b)

FIGURE 3.16 Time history of the force and moment ($\xi_G/\lambda = 0.25$, r_0 =0.0208 rad/s)

(a) lateral force Y (b) yaw moment N

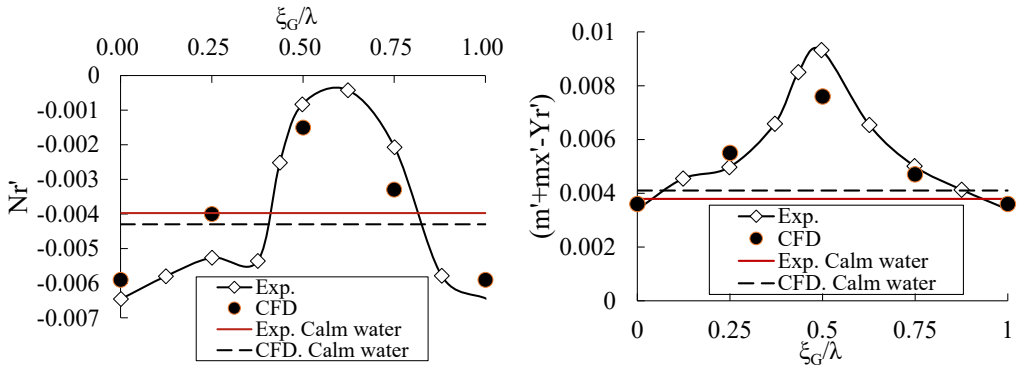

(a) (b)

FIGURE 3.17 Comparison of hydrodynamic derivatives in calm water and regular following waves (a) N'_r (b) $(m' + m'_x - Y'_r)$

The linear yaw-rate-related hydrodynamic derivatives are drawn in Fig 3.17. It is

obvious that N'_r and $(m'+m'_x-Y'_r)$ vary with the change of the relative position. For $(m'+m'_x-Y'_r)$, the maximum value is obtained when gravity center locates on the crest and the minimum data is obtained on the trough. For N'_r under the $\xi_G/\lambda=0.5$ condition, the absolute value is much smaller than those in other relative positions and the calm water condition. It is because that the ship gravity center locates on the wave crest making the altitude of the free surface on the bow and stern lower than that under the calm water condition. The dynamic pressure on the bow and stern is crucial for the whole yaw moment. Hence, the absolute value of the N'_r in this condition is the lowest, which is approximately one-sixth of the largest one. It also indicates the huge wave effect on the hydrodynamic derivatives.

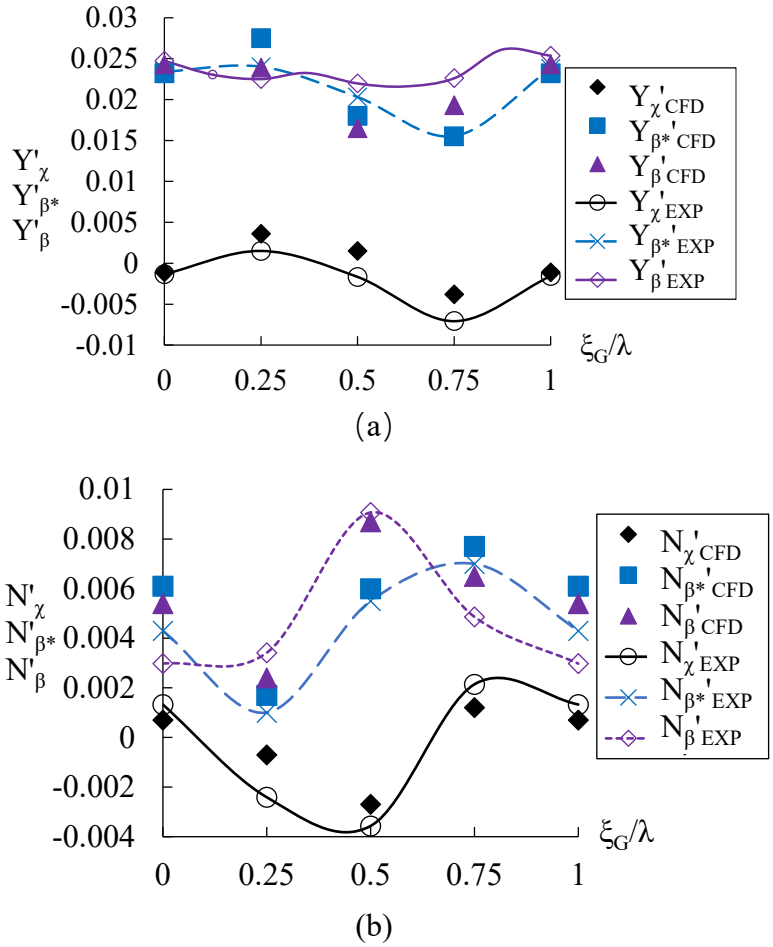

FIGURE 3.18 Comparison of wave-induced hydrodynamic derivatives

(a) comparison of $Y'_\chi, Y'_{\beta*}, Y'_\beta$ (b) comparison of $N'_\chi, N'_{\beta*}, N'_\beta$

TABLE 3.7 Comparison of hydrodynamic derivatives in following waves obtained from numerical and experimental pure yaw tests

Relative position	Derivatives	CFD	Experiment
Wave crest	Y'_r	-0.0002	-0.0012
	N'_r	-0.0008	-0.0015
	Y'_χ	0.0015	-0.0017
	N'_χ	-0.0027	-0.0033
Down-slope	Y'_r	0.0035	0.0032
	N'_r	-0.0033	-0.0021
	Y'_χ	-0.0038	-0.0071
	N'_χ	0.0012	0.0016
Up-slope	Y'_r	0.0027	0.0032
	N'_r	-0.0040	-0.0053
	Y'_χ	0.0036	0.0015
	N'_χ	-0.0007	-0.0004
Wave trough	Y'_r	0.0046	0.0048
	N'_r	-0.0059	-0.0065
	Y'_χ	-0.0011	-0.0013
	N'_χ	0.0007	0.0009

Moreover, the wave-induced hydrodynamic derivatives Y'_χ and N'_χ can be obtained by these simulations. In section 3.5.1, the hydrodynamic derivatives Y'_{β^*} and N'_{β^*} include the wave force component, which makes the comparison of these derivatives in waves and calm waters inappropriate. Therefore, the wave-induced hydrodynamic derivatives Y'_χ and N'_χ should be calculated according to Eq(3.15)

and subtracted to obtain Y'_β and N'_β. The results are summarized in Table 3.7. In Fig 3.18, all the parameters obtained are drawn and compared with the experiment data. The wave-induced hydrodynamic derivatives Y'_χ and N'_χ are obtained by Eq(3.15). The curves of the wave-induced hydrodynamic derivatives are fluctuating around the y=0 axis. In Fig 3.18(a), the simulated Y'_χ and Y'_{β^*} are in good agreement with those experimental data. However, for the experimental result of Y'_β, there is no obvious sinusoidal trend as the curve of $Y'_{\beta CFD}$. For the yaw moment, the simulation results agree well with the experiment ones shown in Fig 3.18(b).

3.5.3 Course stability index in waves without steering

For the study of the surf-riding/broaching-to phenomenon, the weak course stability is considered as the possible reason for this stability failure mode. By simulating the PMM tests in the surf-riding condition, the course stability in waves can be assessed to verify this hypothesis. Son and Nomoto (1982) evaluated the course stability in waves using the traditional course stability discriminant ($D = Y'_v N'_r + (m' + m'_x - Y'_r) N'_v$). The comparison between the experimental data and the calculated data obtained from the CFD simulation is shown in Fig 3.19. It is obvious that the CFD predicted results are well consistent with the experimental ones. As we all know, D>0 represents that the ship has course stability and the larger the value, the better the course stability. Therefore, Fig 3.19 reveals that the stability discriminant D near the crest is smaller than that in calm water and the minimum value is negative which may result in poor stability in the down-slope condition.

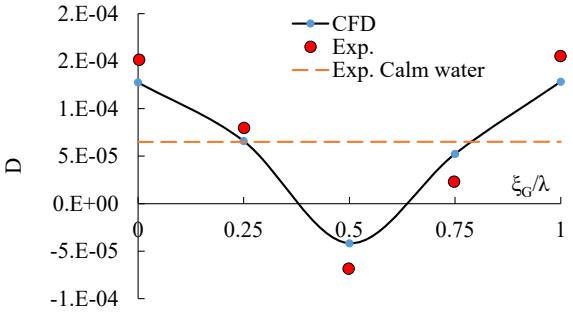

FIGURE 3.19 Course stability discriminant D

However, the conclusion that the most dangerous condition is the wave crest condition is not satisfied with the actual situation. In addition, the course stability discriminant in calm water is not suitable in the wave conditions in theory. Because this discriminant should be obtained from the motion equations and stability discrimination

of the system. In the surf-riding condition, the longitudinal velocity u is a constant. Therefore, the equation in the longitudinal direction can be neglected. For the wave condition, the motion equations are different from those in calm water, which can be expressed as follows.

$$\begin{cases} \left(m+m_y\right)\dot{v}+\left(m+m_x\right)ur = Y_v v + Y_r r + Y_\delta \delta + Y_\chi \chi \\ \left(I_z+J_z\right)\dot{r} = N_v v + N_r r + N_\delta \delta + N_\chi \chi \end{cases} \quad (3.16)$$

The dimensionless equations are

$$\begin{cases} \left(m'+m_y'\right)\dot{v}'+\left(m'+m_x'\right)r'-Y_v'v'-Y_r'r'-Y_\chi'\chi' = Y_\delta'\delta' \\ \left(I_{zz}'+J_{zz}'\right)\dot{r}'-N_v'v'-N_r'r'-N_\chi'\chi' = N_\delta'\delta' \end{cases} \quad (3.17)$$

According to the physical meaning, the yaw angular velocity can also be expressed as $r=\dot{\chi}$. The equations can be expressed as:

$$\begin{cases} \left(m'+m_y'\right)\dot{v}'+\left(m'+m_x'-Y_r'\right)\dot{\chi}'-Y_v'v'-Y_\chi'\chi' = Y_\delta'\delta' \\ \left(I_{zz}'+J_{zz}'\right)\ddot{\chi}'-N_v'v'-N_r'\dot{\chi}'-N_\chi'\chi' = N_\delta'\delta' \end{cases} \quad (3.18)$$

When the rudder is not steering, the equations have general solution:

$$v' = \tilde{v}e^{\sigma t} \qquad \chi' = \tilde{\chi}e^{\sigma t} \quad (3.19)$$

It should be noticed that the condition when the rudder is not steering is unrealistic for the real adverse wave conditions. However, to explore the characteristics of bare hull ship itself, and to simplify the problem, we use this condition in this paper.

Then the new equations can be obtained by adding these terms into the equations above.

$$\begin{cases} \left(m'+m_y'\right)\sigma\tilde{v}+\left(m'+m_x'-Y_r'\right)\sigma\tilde{\chi}-Y_v'\tilde{v}-Y_\chi'\tilde{\chi} = 0 \\ \left(I_{zz}'+J_{zz}'\right)\sigma^2\tilde{\chi}-N_v'\tilde{v}-N_r'\sigma\tilde{\chi}-N_\chi'\tilde{\chi} = 0 \end{cases} \quad (3.20)$$

To ensure the equations have non-zero solutions, the determinant of $\tilde{v}$ and $\tilde{r}$ should be zero, i.e.,

$$\begin{vmatrix} \left(m'+m_y'\right)\sigma-Y_v' & \left(m'+m_x'-Y_r'\right)\sigma-Y_\chi' \\ -N_v' & \left(I_{zz}'+J_{zz}'\right)\sigma^2-N_r'\sigma-N_\chi' \end{vmatrix} = 0 \quad (3.21)$$

Finally, we can obtain

$$A_w s^3 + B_w s^2 + C_w s + D_w = 0 \quad (3.22)$$

where,

$$\begin{aligned} A_w &= \left(m'+m_y'\right)\left(I_{zz}'+J_{zz}'\right) \\ B_w &= -\left(m'+m_y'\right)N_r'-\left(I_{zz}'+J_{zz}'\right)Y_v' \\ C_w &= -\left(m'+m_y'\right)N_\chi'+N_r'Y_v'+\left(m'+m_x'-Y_r'\right)N_v' \\ D_w &= N_\chi'Y_v'-N_v'Y_\chi' \end{aligned} \quad (3.23)$$

According to the criterion of Routh-Hurwitz, the coefficients A_w to D_w should

satisfy the following equations to ensure the stable system.

$$\begin{cases} A_w > 0, B_w > 0, C_w > 0, D_w > 0 \\ B_w C_w - A_w D_w > 0 \end{cases} \quad (3.24)$$

Based on Eq(3.23) and the definition of the physical parameters, it is easy to obtain that $A_w > 0, B_w > 0, C_w > 0$. Therefore, critical criteria should be $D_w > 0$ and $B_w C_w - A_w D_w > 0$.

$$D_w = N'_\chi Y'_v - N'_v Y'_\chi = Y'_v Y'_\chi \left(\frac{N'_\chi}{Y'_\chi} - \frac{N'_v}{Y'_v} \right) > 0 \quad (3.25)$$

It is clearly seen from the simulation results that when the gravity center locates on the up-slope position ($\xi_G / \lambda = 0.25$), $Y'_\chi > 0, N'_\chi < 0$, which makes the critical discriminant $D > 0$. When it comes to the downslope condition ($\xi_G / \lambda = 0.75$), the hydrodynamic derivatives $Y'_\chi < 0, N'_\chi > 0$ which makes the critical discriminant $D_w < 0$. The discriminant of the course stability in waves D_w in different relative positions is calculated and drawn in Fig 3.20. It reveals that the ship system in the downslope condition is unstable, which might result in the occurrence of the broaching-to phenomenon.

Comparing Fig 3.19 and Fig 3.20, it can be found that the discriminant D cannot be adopted as a simple alternative for D_w, because the calculated unstable regions evaluated by these two discriminants are quite different. The discriminant in waves can also indicate that the dominated factors are the wave force coefficients Y'_χ, N'_χ, which reveals that the course stability in waves is determined by the wave effect on the hull.

Furthermore, the stability of the ship system can be evaluated quantitatively by the symbol of the solutions of the characteristic equation Eq(3.22). In this method, the nonnegativity of the roots of the characteristic equation is the sufficient and necessary condition for the asymptotic stability of the ship system. If the maximum root is larger than zero, the lateral velocity and yaw angle will be far from zero as time passes, which means the system is unstable. In contrast, if all the roots are negative, the velocities will approach zero, which indicates the ship system is stable.

After calculating roots of the univariate cubic equation, the largest real part of characteristic roots of the equation for course stability $\sigma_{\max}$ can be drawn in Fig 3.21. Two lines obtained from the experiments and the numerical simulation are drawn in this figure. Obviously, both results show the instability under the downslope condition. The critical values of the stability (the value when $\sigma_{\max} = 0$) in these two lines are close.

The values calculated by the CFD method differ significantly from those obtained from the experiment data in some cases, especially the upslope and downslope condition. The reason might come from the previous errors of hydrodynamic derivatives. The largest real part of characteristic roots is calculated by the cubic equation including all the hydrodynamic derivatives. The errors of the simulated hydrodynamic derivatives, such as the wave-induced hydrodynamic derivatives Y'_χ, N'_χ, are accumulated and expanded, which causes a huge difference. However, for the instability zone prediction, the CFD method is of high accuracy due to the close critical values of the course stability. The value of the root is not important for this unsafety range or risk possibility.

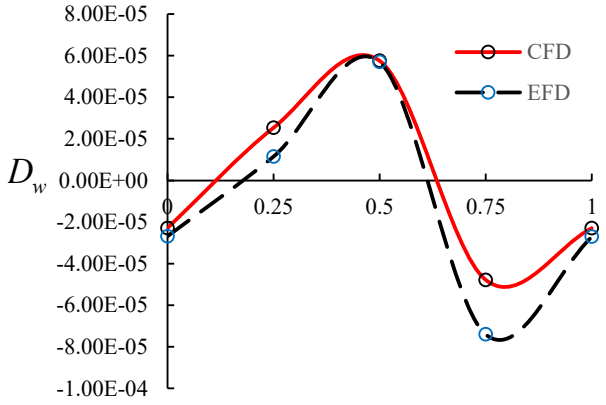

FIGURE 3.20 The discriminant of the course stability in waves D_w

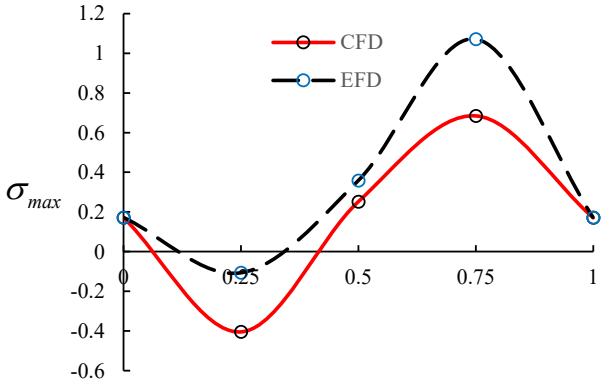

FIGURE 3.21 Largest real part of characteristic roots for course stability

3.5.4 Course stability in waves with PID control

For the actual steer condition, the rudder will be steered to keep the sailing direction. PID (proportional–integral–derivative) autopilot is one of the most widely used methods. A function of the rudder angle should be added in Eq(3.17) as:

$$\delta = K_p\chi + K_i\int_0^t \chi dt + K_d\dot{\chi} \quad (3.26)$$

where K_p is the proportional gain, K_i is the integral gain, and K_d is the derivative coefficient.

To ensure that Eq(3.17) has non-zero solutions, the determinant of lateral velocity, wave incident angle and rudder angle should be zero, i.e.,

$$\begin{vmatrix} \left(m'+m'_y\right)\sigma - Y'_v & \left(m'+m'_x-Y'_r\right)\sigma - Y'_\chi & -Y'_\delta \\ -N'_v & \left(I'_{xx}+J'_{xx}\right)\sigma^2 - N'_r\sigma - N'_\chi & -N'_\delta \\ 0 & -K_p - K_i\dfrac{1}{\sigma} - K_d\sigma & 1 \end{vmatrix} = 0 \quad (3.27)$$

Then, it can be transferred as follows.

$$a_4\sigma^4 + a_3\sigma^3 + a_2\sigma^2 + a_1\sigma + a_0 = 0 \quad (3.28)$$

where

$$\begin{cases} a_4 = \left(m'+m'_y\right)\left(I'_{zz}+J'_{zz}\right) \\ a_3 = -\left(m'+m'_y\right)N'_r - \left(I'_{zz}+J'_{zz}\right)Y'_v - K_d N'_\delta\left(m'+m'_y\right) \\ a_2 = -\left(m'+m'_y\right)N'_\chi + N'_r Y'_v + \left(m'+m'_x-Y'_r\right)N'_v - K_d Y'_\delta N'_v \\ \quad -K_p N'_\delta\left(m'+m'_y\right) + K_d N'_\delta Y'_v \\ a_1 = N'_\chi Y'_v - N'_v Y'_\chi - K_p Y'_\delta N'_v + K_p N'_\delta Y'_v - K_i N'_\delta\left(m'+m'_y\right) \\ a_0 = -K_i N'_v Y'_\delta + K_i N'_\delta Y'_v \end{cases}$$

Based on Routh–Hurwitz stability criterion, to keep the stability of the system, the coefficients $a_n\left(n=0\sim4\right)$ should satisfy the following equations.

$$\begin{cases} a_n > 0\left(n=0\sim4\right) \\ a_3a_2 > a_4a_1 \\ a_3a_2a_1 > a_4a_1^2 + a_3^2a_0 \end{cases} \quad (3.29)$$

TABLE 3.8 Stability discriminants calculated using the experimental hydrodynamic derivatives (EFD) with $K_p=-1, K_i=-0.1, K_d=-4$

Discriminant	Trough	Up-slope	Crest	Down-slope
a_4	1.40E-05	1.40E-05	1.40E-05	1.40E-05
a_3	1.95E-04	1.84E-04	1.09E-04	1.19E-04
a_2	3.11E-04	2.80E-04	2.04E-04	1.57E-04
a_1	1.42E-05	4.87E-05	1.08E-04	**-3.65E-05**
a_0	3.92E-06	3.51E-06	4.92E-06	3.59E-06
$a_3\ a_2 - a_4\ a_1$	6.05E-08	5.08E-08	2.08E-08	1.92E-08
$a_3\ a_2\ a_1 - a_4\ a_1^2 - a_3^2\ a_1$	7.12E-13	2.36E-12	2.19E-12	**-7.51E-13**

TABLE 3.9 Stability discriminants calculated using the numerical hydrodynamic derivatives (CFD) with $K_p = -1, K_i = -0.1, K_d = -4$

Condition	Trough	Up-slope	Crest	Down-slope
a_4	1.40E-05	1.40E-05	1.40E-05	1.40E-05
a_3	1.86E-04	1.66E-04	1.15E-04	1.34E-04
a_2	3.08E-04	2.74E-04	1.83E-04	1.72E-04
a_1	2.23E-05	6.72E-05	1.02E-04	**-1.17E-05**
a_0	4.34E-06	3.97E-06	4.21E-06	3.45E-06
$a_3 a_2 - a_4 a_1$	5.70E-08	4.46E-08	1.95E-08	2.32E-08
$a_3 a_2 a_1 - a_4 a_1^2 - a_3^2 a_1$	1.12E-12	2.89E-12	1.93E-12	**-3.34E-13**

TABLE 3.10 Stability discriminants calculated using the experimental hydrodynamic derivatives (EFD) with $K_p = -0.5, K_i = -0.1, K_d = -4$

Condition	Trough	Up-slope	Crest	Down-slope
a_4	1.40E-05	1.40E-05	1.40E-05	1.40E-05
a_3	1.95E-04	1.84E-04	1.09E-04	1.19E-04
a_2	3.02E-04	2.69E-04	1.94E-04	1.49E-04
a_1	**-5.37E-06**	3.11E-05	8.35E-05	**-5.45E-05**
a_0	3.92E-06	3.51E-06	4.92E-06	3.59E-06
$a_3 a_2 - a_4 a_1$	5.89E-08	4.91E-08	2.01E-08	1.84E-08
$a_3 a_2 a_1 - a_4 a_1^2 - a_3^2 a_1$	**-4.66E-13**	1.41E-12	1.62E-12	**-1.06E-12**

TABLE 3.11 Stability discriminants calculated using the numerical hydrodynamic derivatives (CFD) with $K_p = -0.5, K_i = -0.1, K_d = -4$

Condition	Trough	Up-slope	Crest	Down-slope
a_4	1.40E-05	1.40E-05	1.40E-05	1.40E-05
a_3	1.86E-04	1.66E-04	1.15E-04	1.34E-04
a_2	2.98E-04	2.63E-04	1.73E-04	1.63E-04
a_1	6.31E-07	4.73E-05	8.06E-05	**-2.90E-05**
a_0	4.34E-06	3.97E-06	4.21E-06	3.45E-06
$a_3 a_2 - a_4 a_1$	5.56E-08	4.31E-08	1.87E-08	2.23E-08
$a_3 a_2 a_1 - a_4 a_1^2 - a_3^2 a_1$	**-1.16E-13**	1.93E-12	1.45E-12	**-7.08E-13**

To reveal the effect of the PID autopilot on the course stability and evaluate the simulated hydrodynamic derivatives, the stability discriminants are calculated using the experimental and numerical hydrodynamic derivatives in waves. The results are summarized in Tables 3.8~3.13. The red bold numbers represent the instability of the corresponding case. The unstable phenomenon occurs when the gravity center locates on the downslope of the wave with $K_p = -1, K_i = -0.1, K_d = -4$. Compared with the results in Section 3.5.3, these results reveal that the wave trough condition and the up-slope

condition are transferred from the unstable condition to the stable one by using the PID autopilot. Then, the PID parameters are changed to calculate the stability discriminations using the experimental and the numerical hydrodynamic derivatives in the surf-riding condition. The new results are listed in Tables 3.10~11. Both indicate that the wave trough condition will be unstable due to rudder control with mild sensitivity. These four tables also reveal that the difference of the hydrodynamic derivatives in waves results in the difference of the course stability which makes the ship is dangerous when locates on the downslope condition. The comparison between the numerical and experimental results verified that the course stability discriminants using the numerical hydrodynamic derivatives can provide the same conclusion as the experimental one. In Tables 3.12~13, the stability discriminants calculated with higher sensitive PID parameters are listed. The results show that the ship is stable in all four typical positions when adopting these PID parameters. This does not mean the broaching-to phenomenon can be avoided for any ship and any conditions through the modification of the PID parameters. The calculation results are utilized to clarify that the appropriate PID control parameters can be helpful for the course stability in waves and the numerical hydrodynamic derivatives can replace the experimental ones to calculate the course stability discriminants in waves.

TABLE 3.12 Stability discriminants calculated using the experimental hydrodynamic derivatives (EFD) with $K_p = -2, K_i = -0.1, K_d = -4$

Condition	Trough	Up-slope	Crest	Down-slope
a_4	1.40E-05	1.40E-05	1.40E-05	1.40E-05
a_3	1.95E-04	1.84E-04	1.09E-04	1.19E-04
a_2	3.67E-04	3.43E-04	2.61E-04	2.07E-04
a_1	1.32E-04	1.54E-04	2.56E-04	7.12E-05
a_0	3.92E-06	3.51E-06	4.92E-06	3.59E-06
$a_3\ a_2 - a_4\ a_1$	6.98E-08	6.10E-08	2.50E-08	2.36E-08
$a_3\ a_2\ a_1 - a_4\ a^2_1 - a^2_3\ a_1$	9.06E-12	9.28E-12	6.34E-12	1.63E-12

TABLE 3.13 Stability discriminants calculated using the numerical hydrodynamic derivatives (CFD) with $K_p = -2, K_i = -0.1, K_d = -4$

Condition	Trough	Up-slope	Crest	Down-slope
a_4	1.40E-05	1.40E-05	1.40E-05	1.40E-05
a_3	1.86E-04	1.66E-04	1.15E-04	1.34E-04
a_2	3.64E-04	3.37E-04	2.40E-04	2.22E-04
a_1	1.53E-04	1.86E-04	2.28E-04	9.16E-05
a_0	4.34E-06	3.97E-06	4.21E-06	3.45E-06
$a_3\ a_2 - a_4\ a_1$	6.57E-08	5.34E-08	2.43E-08	2.84E-08
$a_3\ a_2\ a_1 - a_4\ a^2_1 - a^2_3\ a_1$	9.87E-12	9.85E-12	5.50E-12	2.54E-12

3.6 Summary

In this chapter, a standard ship model, S175, is chosen as the target ship model. The wave-effected hydrodynamic derivatives of S175 are calculated by PMM test simulations in following waves, the surf-riding condition, specifically. The results are validated using experimental data and achieve good agreements in most cases. This study aims to provide preliminary research on hydrodynamic derivatives in waves. In addition, the course stability in waves is calculated based on the hydrodynamic derivatives obtained from the numerical simulation, which reveals the mechanism of the broaching-to phenomenon.

The main conclusions can be summarized as follows:

(1) The numerical simulation method established here can effectively deal with problems of captive model tests in regular following waves. The overset grid and Euler overlay method are useful and efficient. Grid convergence study for PMM tests in the surf-riding condition is firstly performed to verify the CFD setup. A good consistency has been obtained by comparing the calculated hydrodynamic derivatives in waves with those in experiments in most cases.

(2) Wave effect on the hydrodynamic derivatives is significant in some conditions which cannot be ignored. The detailed changing tendencies and calculation equations of all wave-affected hydrodynamic derivatives in numerical simulations are proposed. N_r' under the wave trough is twice that under the calm water condition, and $\left(m'+m_x'-Y_r'\right)$ under the wave crest is also around twice the value under the calm water condition.

(3) By calculating the course stability in waves qualitatively and quantitatively, the ship system in the down-slope condition is verified to be unstable, which results in the broaching-to phenomenon. In addition, this conclusion is also validated by the calculated course stability in waves with PID control.

There are some limitations for this first study on the numerical simulation of the captive model tests in waves. Firstly, to reduce the grid number and ensure the convergence, the rolling mode motion is not considered in this paper. Further investigation should consider the roll motion effect and coupling terms. Secondly, only four typical relative positions are selected for simplification. However, the extreme points of sinusoidal variation of the hydrodynamic derivatives are not precisely at these four positions in practice. Therefore, if these hydrodynamic derivatives in waves are utilized in the mathematical model in the future, eight relative positions of ship and waves should be selected at least.

Chapter 4 Captive model tests in head waves

The previous chapter focused on the following wave condition without other wave direction conditions. The main reason why the current research mainly limited on the following wave condition is that the experimental method as well as the data processing method in other wave conditions is difficult. For instance, in head waves, the relative position between the ship and the wave (ξ_G/λ) will change rapidly rather than be stationary all the time, which makes it hard to obtain the influence of ξ_G/λ on the maneuvering hydrodynamic derivatives.

To solve this problem, a method of separating the whole hydrodynamic forces into the low-frequency and high-frequency part based on the Fast Fourier transform technique is adopted. The influence of the rapidly changed parameter ξ_G/λ on the low-frequency forces is considered as a time-average effect and not researched. A similar method has been utilized by Rameesha and Krishnankutty (2019) before. Relying on the mesh-morphing method, they simulated the PMM tests in head waves and the low-frequency components obtained by the FFT technique are utilized to calculate the wave-effected hydrodynamic derivatives. However, their simulations are conducted only in one wave condition. To explore the influence of the wave parameters on hydrodynamic derivatives, various wavelengths and wave steepness should be simulated to conduct the PMM tests. What's more, the simulation results were not validated by the experimental data in the referenced paper (Rameesha and Krishnankutty, 2019). Therefore, in present research, the simulations of the PMM tests in various head wave conditions are carried out and validated by the experimental data.

In this section, the head wave direction is chosen as the target wave direction. The standard ship model, KVLCC2, is the target ship model. The captive model tests in calm water conditions and regular head wave conditions are performed in the towing tank of Shanghai Jiao Tong University. Considering the economy and time cost, the numerical simulation is a useful and effective alternative for the experiments. What's more, the numerical method can also provide flow field information easily. Hence, the captive model tests in calm water and regular head waves are carried out by the numerical and experimental methods together in this section. Systematic simulations in head waves are performed based on the RANS code. The simulation results of the captive model tests in head waves are verified and validated by the experimental data for the first time. The conclusions obtained from the simulations are summarized to reveal the wave effect on the hydrodynamic derivatives in head wave conditions.

4.1 Simulation conditions

Principal particulars of the target ship model KVLCC2 are listed in Table 4.1. The

bare hull without a rudder and a propeller is utilized in the experiments and simulations.

For the captive model tests in head waves. they are carried out in the towing tank of Shanghai Jiao Tong University. The towing tank is 300m long, 16m wide, and 7.5m deep equipped with a drive carriage, a Planar Motion Mechanism (PMM), a wave maker, and a wave-damping beach shown in Fig 4.1. The detailed PMM facility and the data acquisition system are drawn in Fig 4.2. In this figure, the drive carriage is instrumented with a computer for data acquisition and post-processing, a signal amplifier, two strain gauge balances for analog voltage measurements of forces, and a control panel for controlling the horizontal motions of the PMM facility by the stepper motor. To generate the preset regular wave, the multi-unit wave-maker system relying on 40 rocker flaps is adopted. The wave-absorption system includes a wave-damping beach and an active wave-absorption system. The ship model and the PMM facility are connected by two strain gauge balances located on the aft and fore of the model. These two connecting points are symmetrical about the ship gravity center. The total lateral or longitudinal force on the ship model is the sum of the data measured by two strain gauge balances. The moment of the ship model should be calculated as follows.

$$N_E = \left(F_{yf} - F_{ya}\right) l_{pmm} \quad (4.1)$$

where F_{yf} and F_{ya} denote the lateral forces monitored on the fore and aft of the model, respectively. l_{pmm} is the distance between two strain gauge balances.

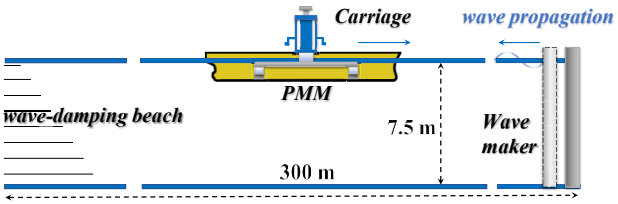

FIGURE 4.1 Illustration of the captive model tests in waves in the towing tank of SJTU

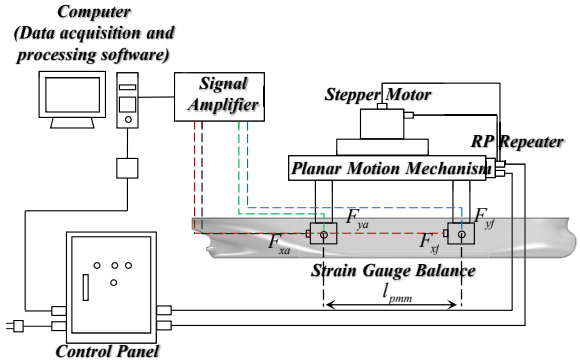

FIGURE 4.2 Illustration of the PMM system

TABLE 4.1 Principal particulars of the KVLCC2

Parameters	Full scale	Model scale
Scale	1	70
Length between perpendiculars (m)	320.0	4.5714
Breadth (m)	58.0	0.8286
Draft (m)	20.8	0.2971
Displacement (ton)	312622	0.9114
Metacentric height (m)	16.8	0.2393
Longi. Center of buoyancy from F.P. (m)	11.1	0.1600
Block coefficient	0.8098	0.8098

The test conditions in regular head waves are summarized in Table 4.2. The simulation conditions are listed in Table 4.3. Considering the high cost of the experiment method, only several simulation conditions are chosen to conduct the experiments to verify the simulation results and explore the physical mechanism. For the simulations, the wavelength to ship length ratio λ/L varies from 0.5 to 1.0 with the wave steepness H/λ varying from 0.03 to 0.055. The vessel speed is 0.953m/s corresponding to the same Froude number (0.142) as the designed speed of the full-scale ship. The oscillation periods of the pure yaw tests are chosen according to the ITTC Guidelines 7.5-02-06-02 (2017) and the parameters of the present experimental facility. For the pure yaw tests in the calm water condition, the model velocities in earth-fixed coordinate system and ship-fixed coordinate system can be expressed as Eq(4.2) and Eq(4.3), respectively (Yoon, 2009).

$$\begin{cases} u_E = const \\ v_E = -y_{\max}\omega\cos\omega t \\ \psi_E = \arctan\left(-\varepsilon\cos\omega t\right) \end{cases} \tag{4.2}$$

$$\begin{cases} u = u_E\sqrt{1+\varepsilon^2\cos^2\omega t} \\ v = \dot{v} = 0 \\ r = \varepsilon\omega\sin\omega t\dfrac{1}{1+\varepsilon^2\cos^2\omega t} \end{cases} \tag{4.3}$$

where $\varepsilon = y_{\max}\omega/u_E$, u_E and v_E are the longitudinal and lateral velocities of the model motivated by the PMM facility under the earth-fixed coordinate system. ω is the oscillation circular frequency. u , v, and r are the longitudinal, lateral, and yaw angular velocities of the model in the ship-fixed coordinate system.

The hull hydrodynamic forces can be expressed as:

$$\begin{cases} Y_H = Y_v v + Y_{v|v|}v|v| + Y_r r + Y_{r|r|}r|r| + Y_{|v|r}|v|r + Y_{v|r|}v|r| \\ N_H = N_v v + N_{v|v|}v|v| + N_r r + N_{r|r|}r|r| + N_{|v|r}|v|r + N_{v|r|}v|r| \end{cases} \tag{4.4}$$

For the pure yaw tests, the components related with the lateral velocity in Eq(4.4) will be removed and the hydrodynamic derivatives only related with the yaw angular

velocity can be calculated.

The main difference between the tests in the calm water condition and those in waves is the generation of waves. The experimental process can be divided into the following steps. Firstly, the model should sway and yaw with the preset parameters. Then, the regular head waves are generated by the wavemaker. When the distance between the wavefront and the ship model is about 10 meters long, the carriage starts to move forward at the preset longitudinal velocity, and the data of the forces and motions are collected from then on. The obtained experimental results will be shown later and can be utilized to validate the numerical simulation results.

TABLE 4.2 Test conditions for the PMM tests in regular head waves

Test	Drift angle (deg)	Oscillation period (s)	λ/L	H/λ
Oblique towing	-4	/	0.5,0.8,1.0	0.03
		/	0.5	0.04
	-8, -2	/	0.5	0.03
Pure yaw	/	17.26,14.10,12.21,10.92	0.5	0.03
		12.21	0.8	0.03

TABLE 4.3 Simulation conditions for the PMM tests in regular head waves

Test	Oscillation period (s)	λ/L	H/λ
Pure yaw	17.26,14.10,12.21,10.92, 9.23	0.5	0.03
	14.10,12.21,10.92, 9.23	0.8	0.03
	14.10,12.21,10.92, 9.23	0.8	0.055
	14.10,12.21,10.92, 9.23	0.1	0.03
	14.10,12.21,10.92, 9.23	0.8	0.03

4.2 Computational method and data processing

The simulation model and setup utilized in this chapter are close to those in Chapter 3. For the simulations in the calm water condition, the computational domain and the boundary conditions are drawn in Fig 4.3. Except the outlet surface adopting the pressure outlet boundary condition, the other five surfaces of the cubic calculation domain adopt the velocity inlet boundary condition. For the hull surface, a no-slip wall boundary is utilized here. The background region is moving horizontally with the same longitudinal and lateral velocities as those of the ship for the purpose of minimizing the calculation domain. The other four degrees of freedom (heave-roll-pitch-yaw) of the background region is fixed. For the wave generation and absorption method, wave damping zones are placed around the outlet and side surfaces to speed up the dissipation. In the wave damping zone, a resistance term is added to the equation for vertical velocity (Choi and Yoon, 2006).

For the simulations in regular head waves, the computational domain and the boundary conditions are shown in Fig 4.4. Different from the calm water cases, the up surface adopts the pressure outlet boundary condition, and the outlet surface adopts the velocity inlet condition to decrease the reverse flow and keep the results convergent.

In fact, there are several dynamic mesh motion techniques, such as the mesh-morphing method, the sliding interface method, and the overset mesh method. Compared with other methods, the mesh-morphing method requires fewer grid numbers and saves the simulation resources. However, the displacement of the body leads to a deformation of single control volumes, which makes the original high-quality mesh can be poor grid quality during the simulations. Some problems, such as the large aspect ratios and the highly skewed cells, might appear, resulting in numerical stability issues. The sliding interface method can handle rotational motion with good numerical stability. However, it is limited by the main disadvantage that they are only appropriate for single DOF (degree of freedom) motions except the multiple sub-domains nested approach. The overset mesh method, also known as "Chimera" or overlapping mesh method, is utilized to discretize a computational domain with several different mesh regions that overlap each other. Even though the required simulation resources are larger than the mesh-morphing method, and the interpolation between meshes may cause some uncertainty, the mesh structure and quality remain constant throughout the simulation with large amplitude motions in multiple DOFs (Davidson et al, 2019). Some scholars (Windt et al, 2020) have concluded that the overset grid method with the same accuracy as the mesh-morphing one is better able to handle the large amplitude motions.

For the current research, a series of wave conditions will be simulated, in which the ship model might have large motions in multi DOFs. Hence, considering the simulation accuracy and the possibility of the extension to more dangerous wave conditions in the future, the overset mesh technique is adopted here.

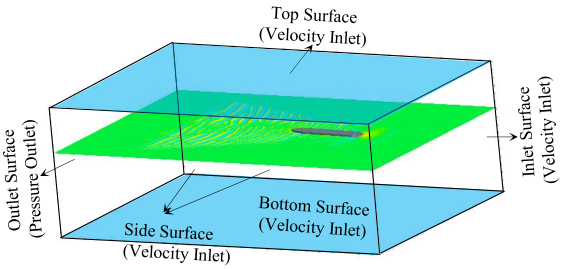

FIGURE 4.3 Computational domain of the pure yaw tests in the calm water condition

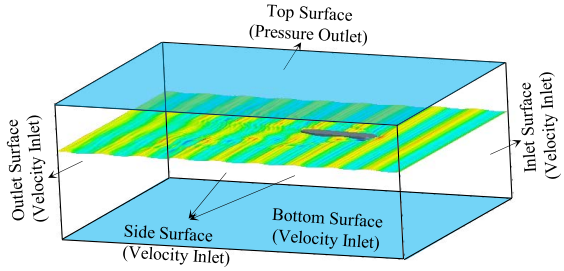

FIGURE 4.4 Computational domain of the pure yaw tests in head waves

For the captive model tests in the calm water condition, the maneuvering motion equations can be expressed as follows:

$$\begin{cases}\left(m+m_y\right)\dot{v}+\left(m+m_x\right)ur=Y_H+Y_E\\ \left(I_z+J_z\right)\dot{r}=N_H+N_E\end{cases} \quad (4.5)$$

Based on Eq(4.5) and the functions of the velocities, the equations for the pure yaw tests can be expressed as:

$$\begin{cases}\left(m+m_x\right)ur=Y_r r+Y_{r|r|}r\left|r\right|+Y_E\\ \left(I_z+J_z\right)\dot{r}=N_r r+N_{r|r|}r\left|r\right|+N_E\end{cases} \quad (4.6)$$

For the pure yaw tests, the forces are not constant. Hence, Eq(4.7) is utilized to calculate the corresponding hydrodynamic derivatives relying on the integral properties of trigonometric functions.

$$\begin{cases}Y_{out}=\dfrac{1}{4}\left(\int_0^{\pi}Y_E d\omega t-\int_{\pi}^{2\pi}Y_E d\omega t\right)=\left(Y_r-mu\right)a\omega^2/u+Y_{r|r|}\left(a\omega^2/u\right)^2\dfrac{\pi}{4}\\ N_{out}=\dfrac{1}{4}\left(\int_0^{\pi}N_E d\omega t-\int_{\pi}^{2\pi}N_E d\omega t\right)=N_r\,a\omega^2/u+N_{r|r|}\left(a\omega^2/u\right)^2\dfrac{\pi}{4}\end{cases} \quad (4.7)$$

For the captive model tests in regular head waves, the wave forces should be added on the motion functions. The FFT method is adopted to separate the low-frequency (PMM-frequency ω) forces and high-frequency (encounter wave frequency ω_e and its multiples) forces. Then, the low-frequency forces are utilized to calculate the hydrodynamic derivatives in waves based on the same method as that in the calm water condition.

For numerical simulations, the mathematical model is slightly different from those for the experiments. The monitored simulated forces are the hydrodynamic components and can be expressed as:

$$\begin{cases}m\dot{v}+mur=Y_H-m_y\dot{v}-m_x ur=Y_{CFD}\\ I_z\dot{r}=N_H-J_z\dot{r}=N_{CFD}\end{cases} \quad (4.8)$$

The transfer function between the numerical simulation results and the experimental results can be expressed as Eq(4.9). Based on that, the simulation results can be transferred into the experimental ones.

$$\begin{cases}Y_E=m\dot{v}+mur-Y_{CFD}\\ N_E=I_z\dot{r}-N_{CFD}\end{cases} \quad (4.9)$$

4.3 Verification and Validation (V&V)

Verification is a process to assess the simulation numerical uncertainty and estimate the magnitude of the simulation numerical error together with the uncertainty in the error estimate. Validation is a process for assessing simulation modeling uncertainty and estimating the magnitude of modeling error (ITTC, 2017a). The V&V should be carried out before the systematical simulations.

4.3.1 V&V for the case in the calm water condition

The pure yaw test in the calm water condition, whose oscillation period T_{pmm} is 9.23s, is chosen to perform the V&V of the present simulation model. Three various grid sizes are utilized to conduct the simulations for the purpose of revealing the convergence of the solutions and calculating the simulation uncertainty. The simulated force coefficients Y_{amp} and N_{amp} ($Y_E(t)=Y_{amp}\sin(\omega t+\varphi)$ and $N_E(t)=N_{amp}\sin(\omega t+\varphi)$) are compared with the experimental ones to validate the effectiveness.

For the present simulations, the unstructured trimmed hexahedral grid is generated with the base size and its multiples. The base size is defined as a fundamental mesh size, and other values such as surface minimum/target size and boundary layer thickness are proportional to it. Therefore, the total mesh sizes can be refined or coarsened by modifying the base size value. The base size for the fine mesh, the middle mesh, and the coarse mesh are 0.01m, 0.015m, and 0.02m, respectively. The total grid number are 0.99 million (0.31 million for the overset region and 0.68 million for the background region), 2.06 million (0.57 million for the overset region and 1.49 million for the background region), and 6.36 million (1.41 million for the overset region and 4.96 million for the background region) for the coarse, middle, and fine mesh, respectively.

The simulated time histories of the lateral force and the yaw moment using different grid sizes are summarized in Fig 4.5. Obviously, all three results are close. For the coarse mesh, the simulation results are in good consistency with the other two results except for several unreasonably high-frequency oscillations. Considering the sine form of the time histories, the amplitudes of the forces are utilized to conduct the verification process and the results are listed in Table 4.4. For the grid uncertainty analysis, the results using the Richardson Extrapolation method can be estimated based on Eq(4.10) and Eq(4.11).

$$U_G=\left(2|1-C_G|+1\right)\left|\delta_{RE_G}\right| \quad (4.10)$$

$$C_G=\left(r_G^{p_G}-1\right)\Big/\left(r_G^{p_{G_{est}}}-1\right) \quad (4.11)$$

where $p_{G_{est}}$ is the limiting order of accuracy of the method. This table reveals that the forces are convergent, and the uncertainty of the mesh size is smaller than 1%S_1 which reveals the small effect of the mesh size on the forces.

The validation of the numerical simulation is drawn in Fig 4.6. The good agreement of the numerical and experimental results indicates that the present numerical method can predict the forces with quite good accuracy. The comparison error E is defined as the difference between the experimental and numerical results. $E(\%D)$ for lateral force Y and yaw moment N are 8.6% and 5.2%, respectively. The validation uncertainty U_V is defined as $U_V^2=U_D^2+U_G^2$, where the uncertainty of

experimental data for lateral force and yaw moment are 1.04% and 1.14%, respectively. Hence, according to ITTC 7.5-03-01-01 (2017), the validation is successful at the 8.6% level for Y and 5.2% level for N from a programmatic standpoint.

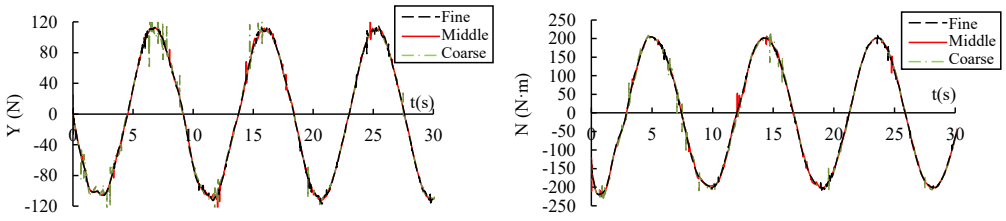

(a) (b)

FIGURE 4.5 Time histories of the lateral force Y and yaw moment N with various mesh sizes in calm water condition

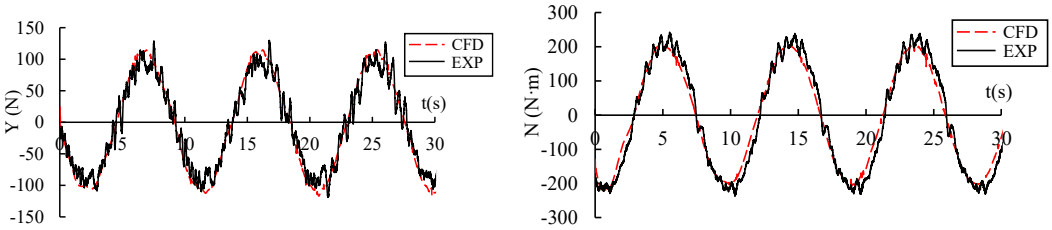

(a) (b)

FIGURE 4.6 Comparison between the numerical and experimental forces

TABLE 4.4 Amplitudes of the lateral force Y and yaw moment N with different mesh sizes in calm water condition

Parameter	Y_{amp} (N)	N_{amp} (N·m)
Fine	109.9	203.9
Middle	109.7	203.8
Coarse	108.8	204.6
ε_{21}	-0.2	-0.1
ε_{32}	-0.9	0.8
R_G	0.2	-0.1
Convergence	MC	OC
p_G	4.342	-
δ_{RE_G}	-0.057	-
U_G	0.138	0.400
$U_G(\%S_1)$	0.126	0.196

4.3.2 V&V for the cases in head waves

The pure yaw test in the head wave condition, whose oscillation period is 12.21s, is chosen to perform the V&V of the simulation model. The wavelength to ship length ratio λ/L is 0.5 and the wave steepness H/λ equals 0.03.

Similarly, three different grid sizes are utilized to conduct the simulations for the head wave condition. The base size for the fine mesh, the middle mesh, and the coarse mesh are 0.01m, 0.015m, and 0.02m, respectively. The total grid number are 1.12 million (0.31 million for the overset region and 0.81 million for the background region), 2.29 million (0.57 million for the overset region and 1.71 million for the background region), and 7.20 million (1.41 million for the overset region and 5.80 million for the background region) for the coarse mesh, middle mesh, and fine mesh, respectively.

The time histories of the lateral force Y and the yaw moment N are summarized in Fig 4.7. Obviously, all three curves obtained from cases with various grid sizes are close to each other. The verification results are listed in Table 4.5. Both forces are monotonic convergent with small uncertainty. Considering the calculation efficiency and accuracy, the middle grid size will be utilized to perform the simulations hereafter.

Fig 4.8 shows the experimental frequency spectrum of the lateral force and yaw moment, which indicates that there are mainly three groups of peaks. The low-frequency part is the maneuvering force, and the other high-frequency forces are the wave-induced forces at the frequency of the encounter wave ω_e and its double $2\omega_e$. The comparison between the numerical and experimental forces are drawn in Fig 4.9. In this figure, "EFD w 1st" represents the experimental results containing only the wave-induced force at the encounter wave frequency and the maneuvering force. The other forces, such as the high-frequency forces in the frequency of $2\omega_e$ and the environment noises, are removed. "EFD w 1st 2nd" stands for the experimental data containing all three forces at the three groups of peaks, i.e., the maneuvering frequency, the encounter wave frequency and the double of the encounter wave frequency. The comparison shows the simulation results are agreed well with the "EFD w 1st". As for the higher frequency forces, the current simulation results may not reflect these forces clearly. The authors considered the error might come from the difference between the experimental and numerical setup. For the experiments, the link point of the ship and PMM facility is two strain gauge balances, which enables the ship to move slightly within the allowable range of the strain balances during the PMM motion. Combined with the large wave loads, the ship will vibrate frequently, and a high-frequency force is produced. This high-frequency force is hard to simulate due to the difference between the experimental setup and numerical setup, which makes the error. In addition, for the present study, the low-frequency maneuvering force is important. The difference between the CFD and EFD results in the high-frequency part ($2\omega_e$) can be acceptable. The validation is successful at the 10.2% level for Y and 6.4% level for N from a programmatic standpoint.

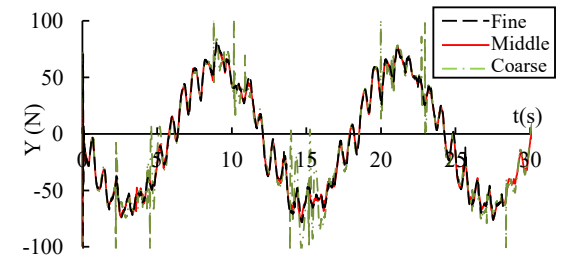

(a)

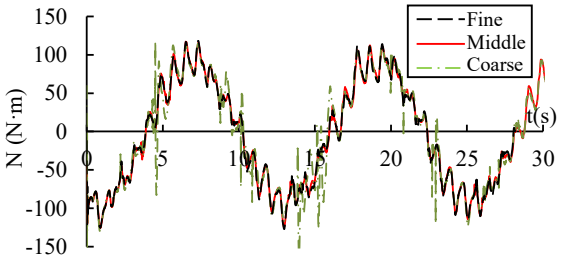

(b)

FIGURE 4.7 Time histories of the lateral force Y and yaw moment N with different mesh sizes in regular head waves

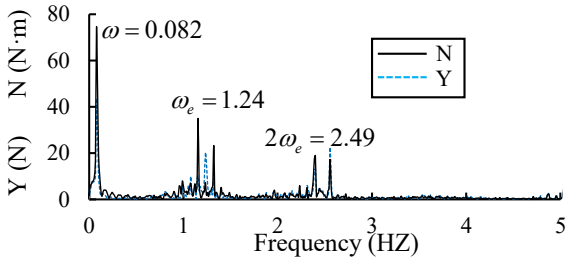

FIGURE 4.8 Frequency spectrum of the lateral force and yaw moment obtained from the experiment in head wave condition

TABLE 4.5 Amplitudes of the lateral force Y and yaw moment N with different mesh sizes in regular head waves

Parameter	Y_{amp} (N)	N_{amp} (N·m)
Fine	63.58	92.48
Middle	63.20	92.22
Coarse	63.04	91.72
ε_{21}	-0.4	-0.3
ε_{32}	-0.2	-0.5
R_G	2.4	0.5
Convergence	MC	MC
p_G	-2.497	1.888
δ_{RE_G}	0.656	-0.282
U_G	4.237	0.845
$U_G(\%S_t)$	6.663	0.914

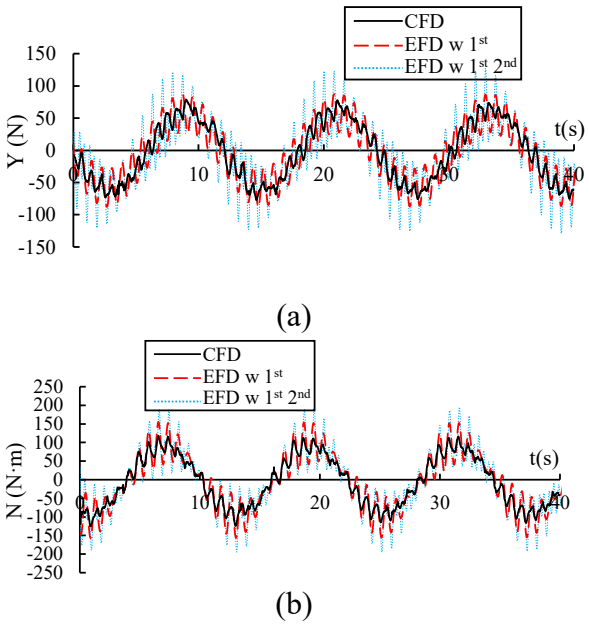

FIGURE 4.9 Comparison between the numerical and experimental data in head waves

4.4 Results and discussions

After the V&V, the present numerical method is considered to be acceptable. Then, systematical simulations are performed relying on this methos and the middle grid size.

4.4.1 Comparison of the forces in calm water and regular head waves

The pure yaw tests are simulated to obtain the hydrodynamic derivatives related with the yaw angular velocity r, such as Y_r, N_r, $Y_{r|r|}$ and $N_{r|r|}$. The time histories of the lateral force and yaw moment for pure yaw tests in the calm water and regular head wave condition are drawn in Fig 4.10. Y and N are the simulated hydrodynamic forces in calm water and wave conditions. Y_{wave} and N_{wave} are the simulated hydrodynamic forces in waves minus those in calm water. The typical real-time attitude of the ship is also shown in these figures. The low-frequency forces in the wave condition seem to be close to the forces in calm water condition. In addition, when the heading angle reaches the extreme value, the wave-induced lateral force $Y_{\_wave}$ reaches the peak. When the heading angle is zero, representing the model is parallel to the wave propagation direction, wave-induced lateral force $Y_{\_wave}$ is the minimum. It is because that the wave-induced forces are larger when the encounter wave direction is closer to the transverse wave. For the yaw direction, there is a phase difference between the motion and the yaw moment.

To analyze the wave effect on the forces, the frequency spectrums of the lateral

force and yaw moment in regular head waves are drawn in Figs 4.11 and 4.12, respectively. The spectrums in waves have obvious peaks around the encounter wave frequency and its multiples. The forces at the frequency larger than $2\omega_e$ is not obvious. With the increase of the oscillation period, the maneuvering motions slow down, and the forces at the PMM motion frequency ω and encounter wave frequency are also decreased. The wave-induced forces increase with the increase of the wavelength and wave steepness, but the maneuvering forces do not.

For the high-frequency part, there are two peaks around the encounter wave frequency and its multiples. It is easy to know through the motion analysis. As shown in Fig 4.13, in step 1, the encounter wave frequency for the fore part of the model is smaller than that at the gravity center. Then, in step 2, the encounter wave frequency for the fore part of the model is larger than that at the gravity center. Similarly, there are also two encounter wave frequencies for the aft part of the ship model. Hence, two peaks will occur around the encounter wave frequency and its multiples. Due to the difference between the flow field around the aft and the fore, the amplitudes of these two peaks are not the same. In addition, with the decrease of the oscillation frequency, the maximum yaw angle of the PMM motion will decrease, and the two peak frequencies will be closer to the encounter wave frequency, representing that the gap between two peaks will decrease. Fig 4.11 and Fig 4.12 verify the correctness of the hypothesis. This finding also indicates the possible errors in some previous methods (Gu et al, 2015). In these methods, the wave forces are obtained by using the pre-calculated frequency-domain drift coefficient and interpolating according to the encountered wave frequency calculated at the gravity center.

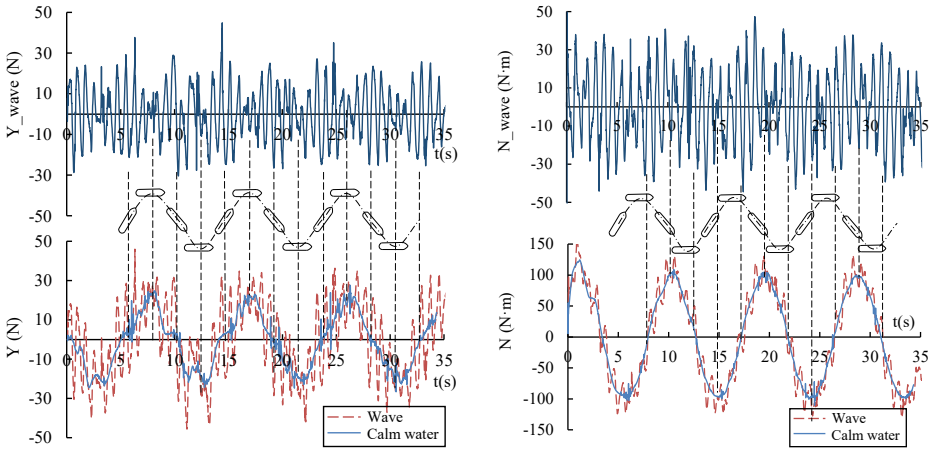

(a) (b)

FIGURE 4.10 Time histories of the lateral force and yaw moment and the instantaneous attitude of the ship in regular head waves (ω=0.0819 ; $\lambda/L=0.5$, $H/\lambda=0.03$)

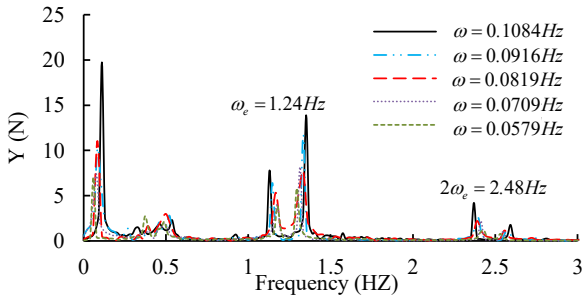

(a)

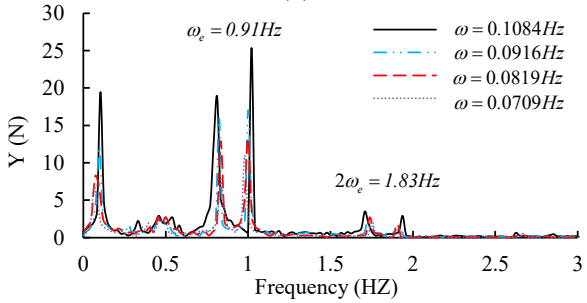

(b)

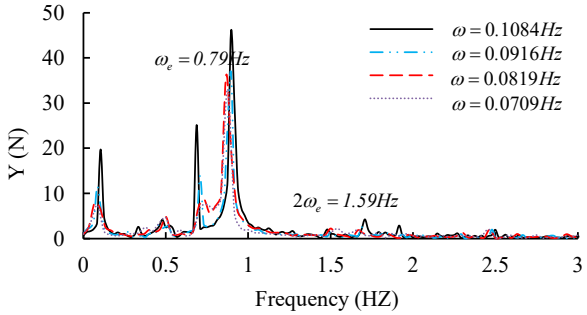

(c)

FIGURE 4.11 The frequency spectrums of the lateral force Y in regular head waves

(a: $\lambda/L = 0.5$, $H/\lambda = 0.03$; b: $\lambda/L = 0.8$, $H/\lambda = 0.03$;c: $\lambda/L = 1.0$, $H/\lambda = 0.03$)

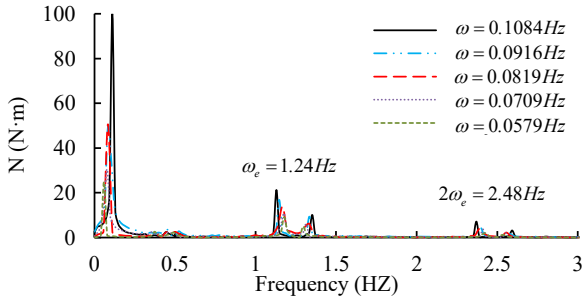

(a)

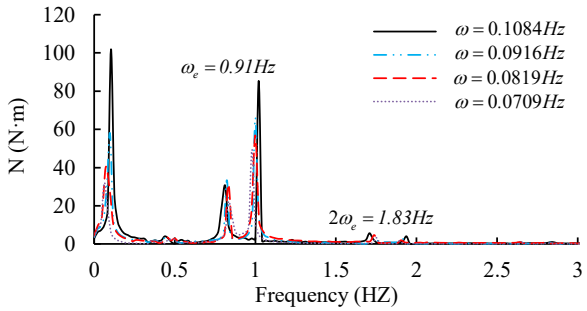

(b)

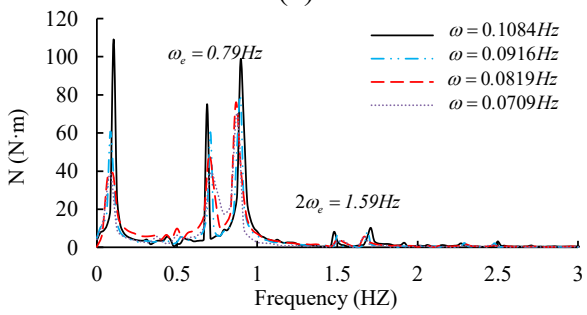

(c)

FIGURE 4.12 The frequency spectrums of the yaw moment N in head waves

(a: $\lambda/L = 0.5$, $H/\lambda = 0.03$; b: $\lambda/L = 0.8$, $H/\lambda = 0.03$;c: $\lambda/L = 1.0$, $H/\lambda = 0.03$)

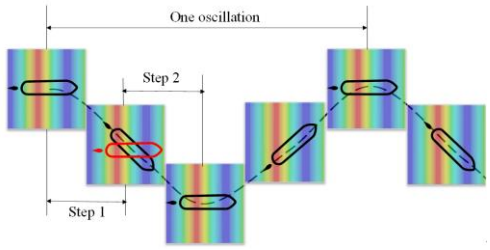

FIGURE 4.13 Illustration of one oscillation motion of the pure yaw test

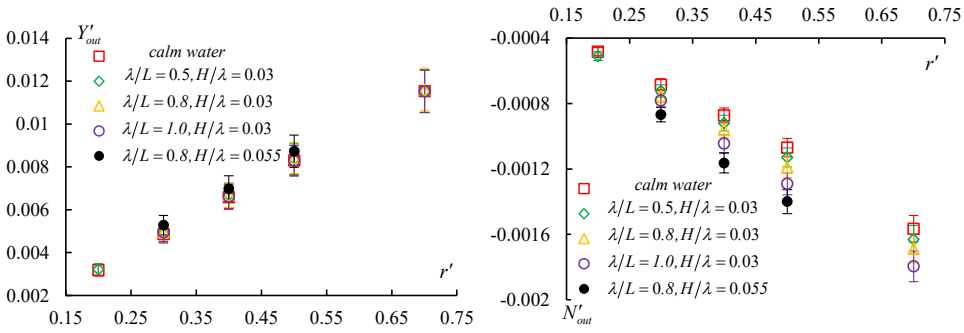

(a) (b)

FIGURE 4.14 Comparison of Y'_{out} and N'_{out} in calm water and head waves

TABLE 4.6 Comparison of the force coefficients of pure yaw tests in calm water and regular head waves

Case	Y_{amp}	N_{amp}	Gap_Y (%)	Gap_N (%)
T_{pmm}=9.23s, calm water	-109.7	-203.8	0.0	0.0
T_{pmm}=9.23s, λ/L=0.5, H/λ=0.03	-109.8	-208.2	0.1	2.2
T_{pmm}=9.23s, λ/L=0.8, H/λ=0.03	-110.8	-212.5	1.0	4.3
T_{pmm}=9.23s, λ/L=1.0, H/λ=0.03	-110.1	-218.4	0.4	7.2
T_{pmm}=10.92s, calm water	-79.13	-122.7	0.0	0.0
T_{pmm}=10.92s, λ/L=0.5, H/λ=0.03	-79.63	-126.9	0.9	4.9
T_{pmm}=10.92s, λ/L=0.8, H/λ=0.03	-80.31	-130.6	1.8	7.9
T_{pmm}=10.92s, λ/L=1.0, H/λ=0.03	-79.08	-136.6	0.2	**12.9**
T_{pmm}=10.92s, λ/L=0.8, H/λ=0.055	-83.80	-138.9	6.2	**14.8**
T_{pmm}=12.21s, calm water	-62.76	-88.70	0.0	0.0
T_{pmm}=12.21s, λ/L=0.5, H/λ=0.03	-63.74	-92.25	1.8	6.3
T_{pmm}=12.21s, λ/L=0.8, H/λ=0.03	-63.68	-96.20	1.7	**10.8**
T_{pmm}=12.21s, λ/L=1.0, H/λ=0.03	-63.27	-99.65	1.0	**14.8**
T_{pmm}=12.21s, λ/L=0.8, H/λ=0.055	-67.32	-106.6	7.5	**22.8**
T_{pmm} = *14.10s*, calm water	-46.27	-60.12	0.0	0.0
T_{pmm}=14.10s, λ/L=0.5, H/λ=0.03	-46.72	-62.11	0.9	6.8
T_{pmm}=14.10s, λ/L=0.8, H/λ=0.03	-47.36	-65.65	2.3	**12.9**
T_{pmm}=14.10s, λ/L=1.0, H/λ=0.03	-47.21	-68.76	2.0	**18.3**
T_{pmm}=14.10s, λ/L=0.8, H/λ=0.055	-51.01	-73.35	**10.2**	**26.2**
T_{pmm} = *17.26s*, calm water	-30.21	-33.85	0.0	0.0
T_{pmm} = *17.26s*, λ/L=0.5, H/λ=0.03	-30.62	-36.47	1.2	8.9

TABLE 4.7 Hydrodynamic derivatives ($\times 10^3$)

Case	$Y_r'^*$	$N_r'^*$	Y_r'	$Y_{r\|r\|}'$	N_r'	$N_{r\|r\|}'$
Calm water	2.4	-2.1	2.4	0.56	-2.2	0.06
λ/L=0.5, H/λ=0.03	2.4	-2.2	2.3	-0.10	-2.4	0.18
λ/L=0.8, H/λ=0.03	2.2	-2.3	2.1	-0.40	-2.5	0.12
λ/L=1.0, H/λ=0.03	2.4	-2.5	2.2	-0.35	-2.7	0.17
λ/L=0.8, H/λ=0.055	1.4	-2.7	1.4	-0.80	-3.1	0.75

*The derivatives with superscript * represent the results obtained by linear fitting, and the others are obtained by quadratic function fitting.

For the low-frequency part, the FFT method is utilized to obtain the wave-effected maneuvering forces. The curve fitting method is adopted to obtain the coefficients Y_{amp} and N_{amp} in regular waves. All results are summarized in Table 4.6. In this table, Gap_Y and Gap_N represent the differences between the force coefficients in the calm water condition and waves. The values larger than 10% are highlighted in red. Obviously, Gap_Y is small except for the steepest wave condition. Gap_N is large in waves and increases significantly with the increase of the wave steepness and the wavelength. Based on Eq(4.7), Y'_{out} and N'_{out} can be calculated and drawn in Fig 4.14. The differences between Y'_{out} in various wave conditions are smaller than the uncertainty range. However, the differences between N'_{out} in various waves are larger than the uncertainty range indicating the significant wave effect on the yaw moment.

Table 4.7 shows the whole simulated hydrodynamic derivatives. We can conclude that the lateral hydrodynamic derivative Y'^{*}_{r} does not change obviously with the wavelength but decreases significantly with the increase of the wave steepness. However, the absolute value of the yaw hydrodynamic derivative N'^{*}_{r} increases significantly with the increase of the wavelength and wave steepness. For the nonlinear hydrodynamic derivatives $Y'_{r|r|}$ and $N'_{r|r|}$ in waves, they change notably compared with those in the calm water condition. Unfortunately, for these high-order derivatives, there is no monotonically changing tendency with the increase of the wavelength and wave steepness. Therefore, it is hard to propose a simple modification on the wave effect on the high-order hydrodynamic derivatives.

4.4.2 Comparison of the flow field in calm water and head waves

The instantaneous free surfaces of the pure yaw tests in the calm water condition and regular waves with various wave parameters are summarized in Figs 4.15~4.17. In these figures, the position z represents the distance between the free surface and the base line of the ship. For the periodic motion with the period T_{pmm}, the typical time $t = T_{pmm}/2$ is chosen to draw the free surface. The comparison between Fig 4.15 and

Fig 4.16 indicates that the wave height around the bow in head waves is higher than that in the calm water condition. In addition, the amplitude of the ship wave in the head wave condition is higher than that in the calm water condition. With the increase of the wavelength, the amplitude of the ship wave increases. Comparing Fig 4.16(a) and Fig 4.17, it is obvious that the PMM motions have little effect on the amplitude of the ship wave and significant effect on the waveform.

Figs 4.18~4.21 show the dynamic pressure on the hull. The windward side is the port side, and the leeward side is the starboard for $t = T_{pmm}/2$. For the port side of the hull in calm water condition, there is an obvious high-pressure zone on the bow and a low-pressure zone after the high-pressure zone. For the starboard in calm water conditions, the low-pressure zone in the bow is larger and with lower pressure than that on the port side. The significant asymmetry of the port side and starboard leads to the lateral force and yaw moment during the motions. For the wave condition, the dynamic pressure distribution on the hull is characterized by the staggered distribution of the high-pressure region and the low-pressure region clearly. Compared with the calm water condition, the dynamic pressure in wave conditions is much higher around the bow and much lower in the low-pressure of the bow. For the wave conditions with different wave parameters, the range of the dynamic pressure is changed significantly. With the increase of wavelength and wave steepness, the amplitude of hull dynamic pressure is greater. The increase of the low-frequency maneuvering motion period also makes the amplitude of hull dynamic pressure larger.

Compared with the hydrodynamic derivatives obtained by FFT and time average processing in the last section, the flow field information analyzed in this section is instantaneous. This analysis not only gives the instantaneous information of the flow field but also explains the source of the difference of time average force from the perspective of the flow field. It can be seen from the analysis that for the instantaneous flow field information, the influence of waves on free surface fluctuation and dynamic pressure is more significant than that of low-frequency maneuvering motions.

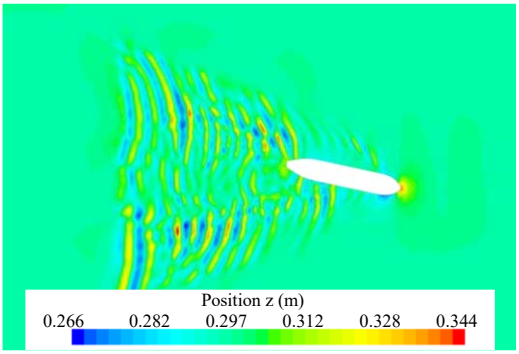

FIGURE 4.15 The free surface in the pure yaw tests (T_{pmm}=9.23s, $t = T_{pmm}/2$) for the calm water condition

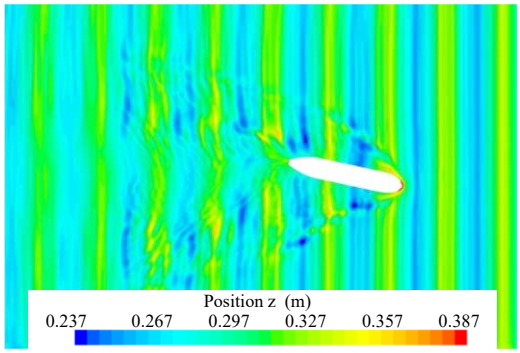

(a)

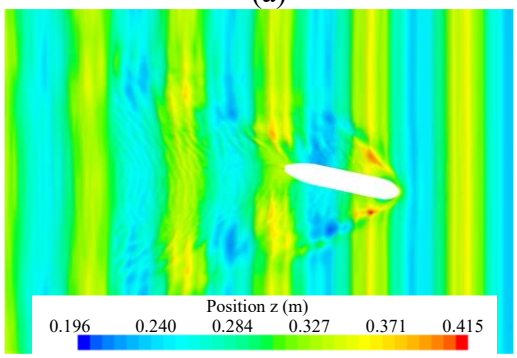

(b)

FIGURE 4.16 The free surface in the pure yaw tests (T_{pmm}=9.23s, $t = T_{pmm}/2$) for the head wave condition (a: $\lambda/L = 0.5$, $H/\lambda = 0.03$; b: $\lambda/L = 0.8$, $H/\lambda = 0.03$)

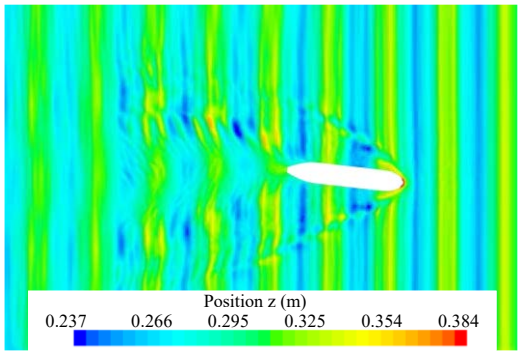

FIGURE 4.17 The free surface in the pure yaw tests (T_{pmm}=17s, $t = T_{pmm}/2$) for the head wave condition ($\lambda/L = 0.5$, $H/\lambda = 0.03$)

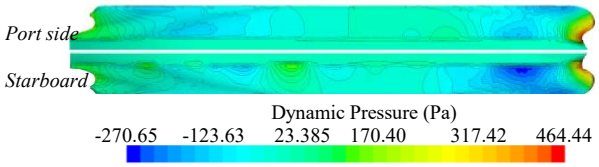

FIGURE 4.18 The dynamic pressure on the hull in the pure yaw tests (T_{pmm}=9.23s, $t=T_{pmm}/2$) for the calm water condition

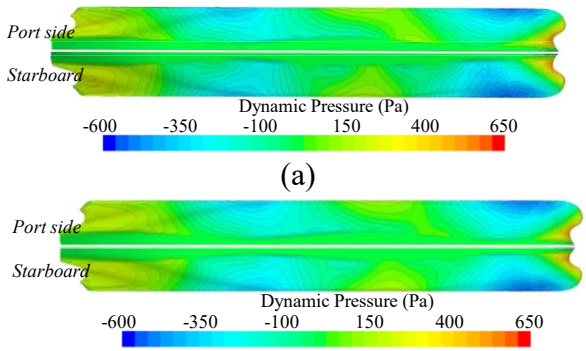

FIGURE 4.19 The dynamic pressure on the hull in the pure yaw tests (T_{pmm}=9.23s, t=T_{pmm}/2) for the head wave condition (a: $\lambda/L=0.5$, $H/\lambda=0.03$; b: $\lambda/L=0.8$, $H/\lambda=0.03$)

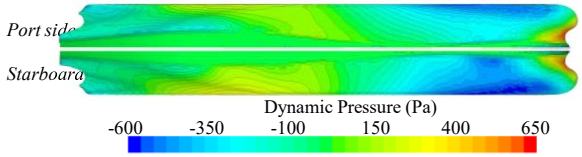

FIGURE 4.20 The dynamic pressure on the hull in the pure yaw tests (T_{pmm}=17s, t=T_{pmm}/2) for the head wave condition ($\lambda/L=0.5$, $H/\lambda=0.03$)

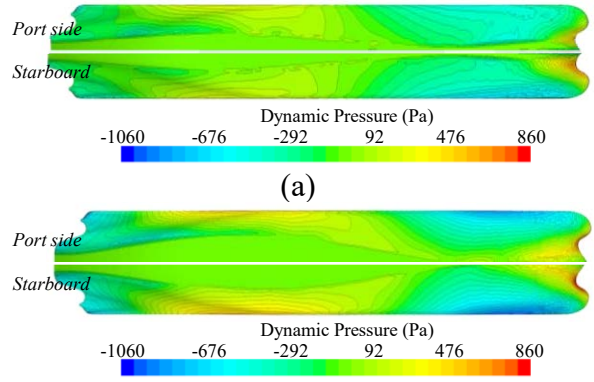

FIGURE 4.21 The dynamic pressure on the hull in the pure yaw tests (T_{pmm}=12s, t=T_{pmm}/2) for the head wave condition (a: $\lambda/L=0.8$, $H/\lambda=0.03$; b: $\lambda/L=0.8$, $H/\lambda=0.055$)

4.5 Summary

In this chapter, the numerical simulations of the pure yaw tests in regular head waves for the KVLCC2 are carried out to detect the wave effect on the maneuvering hydrodynamic derivatives. The relative experiments were carried out in the towing tank of Shanghai Jiao Tong University for the first time. The simulations are carried out based on a RANS code with the overset mesh and Euler overlay techniques. The verification and validation of the simulation method are performed, which reveals the effectiveness of the current numerical methods. Three main conclusions can be summarized here.

1. The present numerical simulation methods can deal with the problem of PMM

tests in head waves efficiently and accurately. Considering the simulation efficiency and potential requirement of extension to more dangerous wave conditions, the overset mesh and Euler overlay techniques are crucial for the simulations of the captive model tests in waves.

2. In regular head waves, the hydrodynamic derivatives will be affected by the wave steepness and the wavelength. Y_r' is basically unchanged from that in the calm water condition except for extremely steep waves. For N_r', the absolute value increases significantly with the increase of wave steepness and wavelength. This explains why the ship might undergo uncontrollable deviation under head waves. However, a simple modification method is hard to be proposed because the nonlinear hydrodynamic derivatives do not increase or decrease monotonically with the increase of the wave steepness and wavelength.

3. The hydrodynamic forces during the maneuvering motions are changed by the high-frequency encounter wave frequency and the low-frequency maneuvering motions. There are two peaks around the encountered wave frequency and its multiples. Therefore, the previous studies on maneuverability in waves using the precalculated second-order wave force and real-time encounter wave frequency corresponding to the gravity center are not accurate enough.

4. The flow field of the captive model tests in head waves are also provided. It not only gives the instantaneous information of the flow field but also explains the source of the difference of time average force from the aspect of the flow field. The effect of waves on free surface fluctuation and dynamic pressure is much more significant than that of low-frequency maneuvering motions. Hence, the wave effect cannot be ignored when considering the instantaneous action and flow field information.

Chapter 5 Free-running tests in the calm water condition

As described in Chapter 1, there are three methods on assessing the maneuverability in waves. The experimental methods are expensive and always be adopted at the final design stage, which make the hull form optimization aiming to improve the maneuverability hard to achieve. The most widely utilized methods, the potential flow methods, are much more efficient and with acceptable engineering precision nowadays at many conditions. However, the potential flow methods require plenty of parameters obtained from captive model tests, such as the self-propulsion point, the hull maneuvering hydrodynamic derivatives, the interaction parameters among a hull, the propeller, and the rudder. In addition, the research shown in Chapter 3 and Chapter 4 reveals that the maneuvering hydrodynamic derivatives will change under the wave conditions, which indicates that there might be some error for present potential flow methods assuming hydrodynamic derivatives in calm water as those in waves. The pure CFD method for free-running tests can solve these problems. The self-propulsion point can be obtained through the pre-calculated simulations. The hull maneuvering hydrodynamic derivatives and the parameters for the hull-propeller-rudder interaction are not needed to obtain from experiments or empirical formulas because all the forces are considered in the simulations.

Before the simulations of free-running tests in waves, the free-running tests in the calm water condition should be simulated first. The research on this topic has been developed for about two decades. Carrica et al (2013) conducted simulations for turn and zigzag tests of a surface combatant using dynamic overset grids and a simplified actuator disk model. Broglia et al (2015) carried out the simulations of turning tests for a fully appended twin-screw vessel considering single and twin rudder configurations, respectively. For the above-mentioned studies, the propellers were simulated using the simplified actuator disk models. Shen et al (2015) implemented overset grid into OpenFOAM and applied the technique to simulate zigzag test using the discretized propeller. Wang and Wan (2018) further extended the solver in simulating the turning tests with discretized propellers and rudders. For these studies, varying degrees of success are achieved. However, the calculation speed and required simulation resources also limit the wide utilization of this method.

As the basis of maneuverability research in waves, this chapter will deal with maneuverability simulation in calm water. In present study, the free-running tests will be simulated using the structured overset Navier-Stokes solver NAGISA with dynamic overset grids. The resistance simulation should be carried out at the first step. Next, the self-propulsion simulation is performed to obtain the propeller rotation speed keeping the balance between the resistance and propulsion. Finally, the turning tests and zigzag tests are simulated using the results of the self-propulsion case as the initial condition.

5.1 Simulation conditions based on the experiments

The containership S175 is the target ship of the present simulations because it is one of the benchmark models for researching the maneuvering in waves according to ITTC (2017b). The free-running tests have been performed in the towing tank of Shanghai Jiao Tong University (Zhang et al, 2017). The principal dimensions and geometry of the ship model are shown in Table 5.1 and Fig 5.1, respectively.

TABLE 5.1 Principal particulars of S175 with a propeller and a rudder

Specifications	Full	Model	Nondimensionalized
Length between perpendiculars, L_{pp}	175m	3.0337m	1
Beam, B	25.4m	0.4403m	0.1451
Draft, d	9.5m	0.1647m	0.0543
Block coefficient C_b	0.57	0.57	0.57
L.C.B. from F.P.	90.65m	1.554m	0.5122
Height of C.G. above base line	\	0.1647m	0.0543
Radius of gyration in roll, k_{xx}	0.33 B	0.23 B	0.23 B
Radius of gyration in pitch, k_{yy}	0.25 L_{pp}	0.262 L_{pp}	0.262 L_{pp}
Radius of gyration in yaw, k_{zz}	0.269 L_{pp}	0.262 L_{pp}	0.262 L_{pp}
Displacement	24742 m^3	0.127 m^3	0.004549
Diameter of the propeller	6.5064m	0.1128m	0.03718
Numbers of blades	5	5	5
Pitch ratio	0.915	0.915	0.915
Rudder aspect ratio	1.8268	1.8268	1.8268
Rudder area	32.46 m^2	0.0098 m^2	0.001065
Rudder height	7.7583m	0.1335m	0.04401

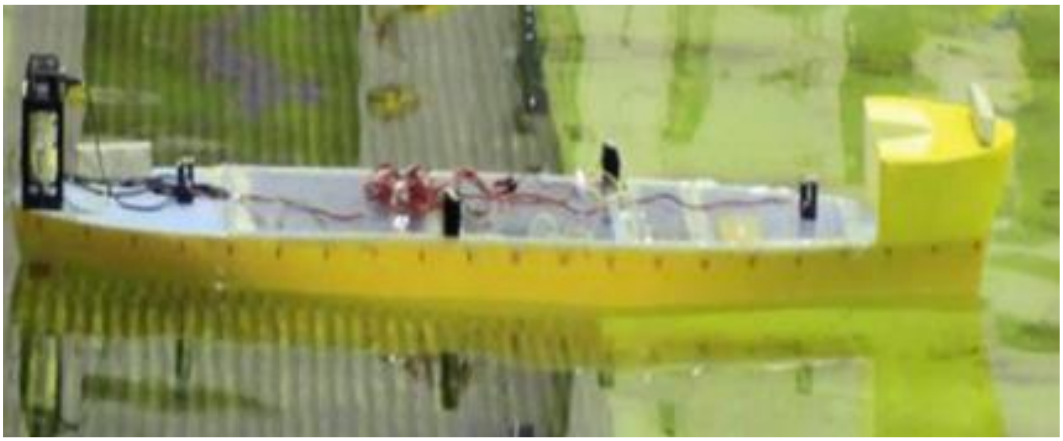

FIGURE 5.1 Ship model picture captured during the experiments

Fig 5.2 shows the flow chart of all simulation conditions for the free-running tests in calm water condition and waves. The free-running tests, including the course-keeping maneuvers, turning maneuvers, and the zigzag maneuvers, are simulated in calm water and wave conditions. For the calm water condition, the resistance test simulation and self-propulsion simulation should be performed before. The resistance test simulation is utilized to obtain the ship resistance in calm water and the initial flow field information for the self-propulsion simulation case. Then, the open-water characteristic of the propeller will be calculated, and the propeller rotation speed will be modified to keep the balance of the propulsion force and the resistance during the self-propulsion simulation case. Finally, different kinds of free-running tests can be simulated based on the flow field of the final steady self-propulsion case. For the simulations in waves, the self-propulsion simulations in various wave conditions should be performed to provide the flow filed information. Finally, based on the flow filed files, course-keeping maneuvers, zigzag maneuvers, and turning maneuvers in regular and irregular waves can be simulated.

Generally, turning circle tests are performed to starboard or port side with 35° rudder angle or the maximum design rudder angle permissible at the test speed. The rudder angle should be executed with a steady speed. The essential parameters measured from turning maneuvers are tactical diameter, advance, and transfer (IMO, 2002a, b). Zig-zag maneuvers are carried out by reversing the rudder alternately to the other side at a deviation ψ from the initial course. ψ is the execute heading angle which means the heading angle when the rudder is reversed. The zig-zag test begins by applying a specified amount of rudder angle to an initially straight approach ("first execute"). Then, the rudder angle is alternately shifted to the other side after a specified deviation from the ship's original heading is reached ("second execute" and following). The essential parameters measured from zig-zag maneuvers are the overshoot angles, initial turning time to second execute and the time to check yaw (IMO, 2002a, b). The course-keeping maneuvers are the steered ship maintain a straight path in a predetermined course direction without excessive oscillations of rudder and heading angle. In fact, the course-keeping maneuvers do not belong to the required experiments to assess the maneuverability in the standards. Usually, the course-keeping ability is assessed by the modified zig-zag tests (with 1 deg execute heading angle and 5- or 10-degrees rudder angle), the direct spiral tests or the reverse spiral tests. However, the simplicity of the direct course-keeping test simulations and the importance of the course-keeping ability for ship navigation in waves requires to conduct these simulations.

For the calm water condition, the turning test is carried out with the maximum rudder angle of 35deg and the rudder speed of 13deg/s which are the same as the experimental ones. The 20/20 zigzag test is simulated with the rudder speed 13deg/s. The propeller rotation is fixed to the predicted value obtained from the self-propulsion case. The vessel speed is set to be 0.818m/s corresponding to the Froude number 0.15. It should be noted that the dimensionless RANS code NAGISA is utilized to conduct the simulations in this and the next chapter. Therefore, the rotation speed and the vessel

speed should be nondimensionalized.

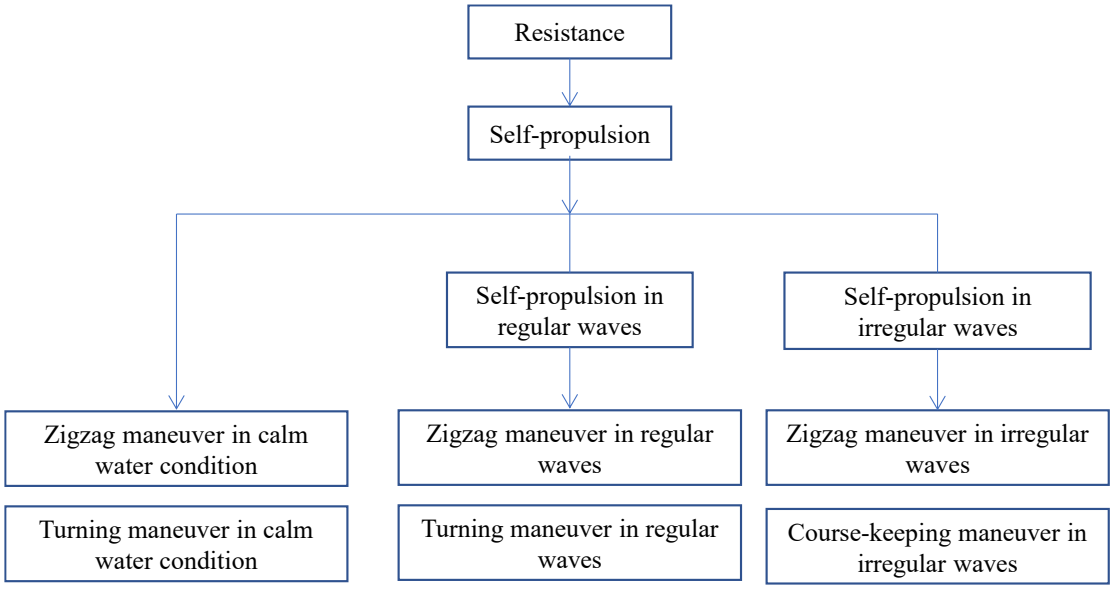

FIGURE 5.2 Flow chart of simulation conditions for the free-running tests

5.2 Computational domain and Grids

The ship geometry for the simulations, S175, is shown in Fig 5.3. Fig 5.4 shows the arrangement of the calculation domain. The base region extends to $-3.0L<x<2.0L$, $-2.5L<y<2.5L$, and $-1.0L<z<0.2L$. As mentioned before, the flow filed result of the resistance case is the initial condition for the self-propulsion simulations, and the result of the self-propulsion case is the initial condition for the free-running case in calm water and wave conditions. Hence, the mesh size around the free surface is determined based on the wave condition for the higher requirement for the mesh size. To achieve the good simulation for the wave field, the minimum size in the longitudinal and lateral directions is calculated by $\lambda/85$ and the minimum size in the vertical direction is calculated by $H_w/15$ for the flattest wave condition, which represents at least 85 points per wavelength and 15 points per wave height. Therefore, the grid number for the base region is around 5 million. The hull region extends to $-0.6L<x<0.6L$, $-0.1L<y<0.1L$, and $-0.1L<z<0.1L$ with the grid number of around 1 million. Considering that the calculation domain will rotate and translate with the ship and the wave is generated from the maximum and minimum coordinates in x and y directions under the initial coordinate system, the cylindrical calculation domain is adopted to reduce the calculation domain size. Wang and Wan (2018) also adopted the same region for the turning test simulations, which shows good accuracy compared with the experimental data. For the cylindrical calculation domain, it has the same horizontal motions (surge-sway-yaw) with the hull region. The other motions are fixed without moving with the hull region.

Fig 5.5(a) shows the overall grid distribution. The black part is the hull overset

region. The red part contains the hull surface and the rudder surface. The rudder overset region is marked in yellow. The outer base grid is drawn in green. Fig 5.5(b) shows the finer grid distribution around the hull from the top view. The detailed overset grid information is drawn in Fig5.5(c) and (d). All the grids are generated by Pointwise. Then, they are pretreated by the grid deformation/machining program UP_MOD and overset grid information generation program UP_OVS of the UP_GRID code (Kodama et al, 2012). The wall function is utilized and y+ is set to be 40 considering the turbulence model requirement. The grid numbers are listed in Table 5.2.

As for the boundary conditions, the hull surface and the rudder surface adopt the wall boundary condition. The other surfaces all adopt the outer boundary condition since the velocity is specified by the ship motion.

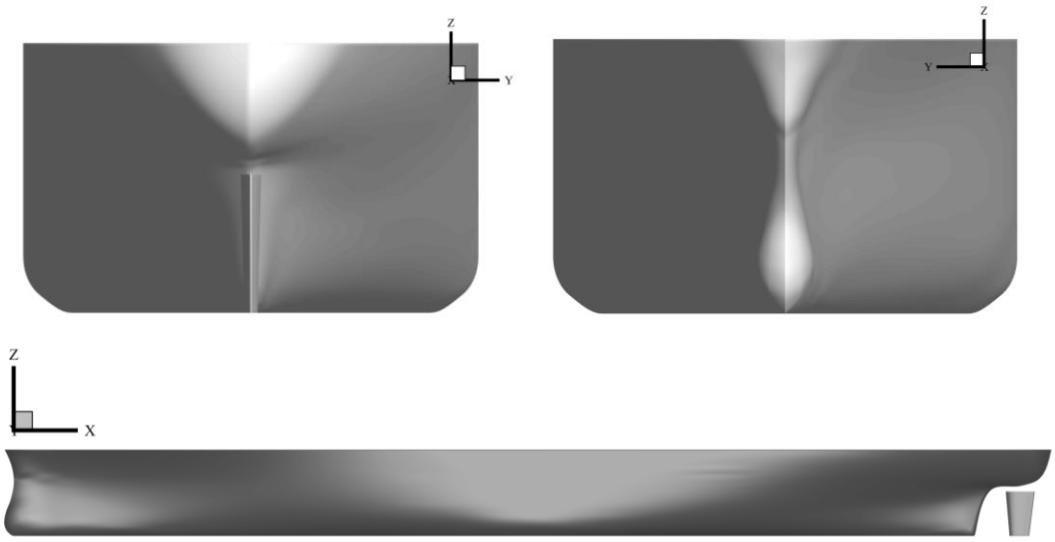

FIGURE 5.3 Ship geometry for the simulations

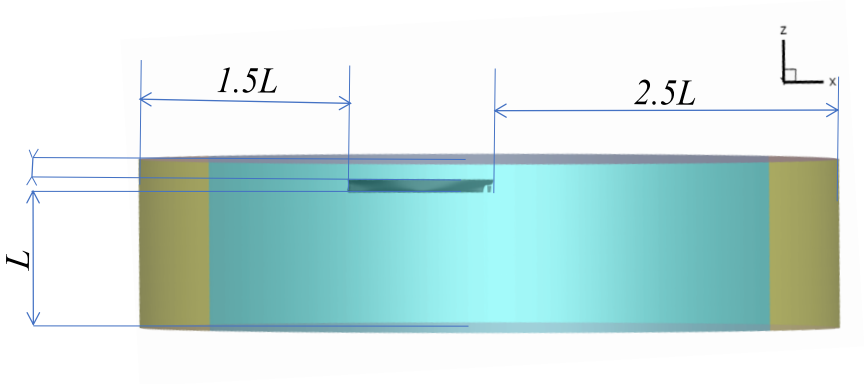

FIGURE 5.4 Arrangement of the calculation domain

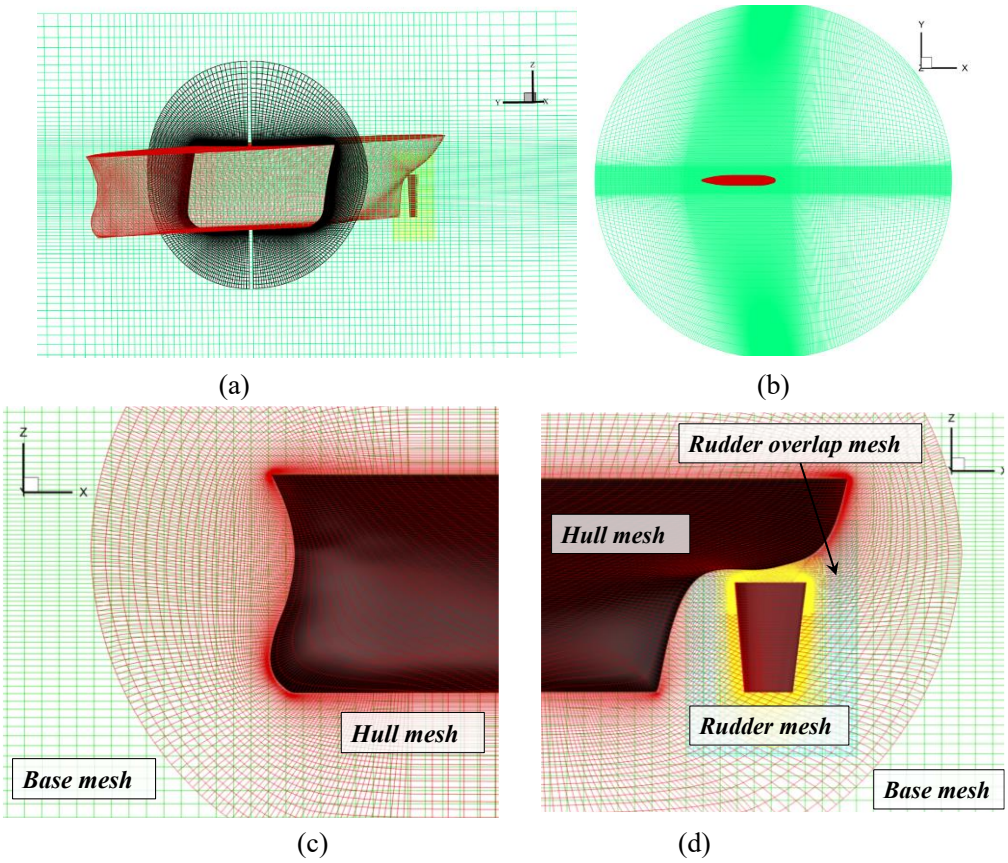

FIGURE 5.5 Grid arrangement

TABLE 5.2 Number of the cells

Grid	IM×JM×KM	Grid number
Hull	167×139×49	1.10 million
Rudder	77×65×45	0.21 million
Rudder overlap region	33×21×61	0.04 million
Base	347×129×111	4.87 million
Total	/	6.22 million

5.3 Numerical simulations

For the resistance simulation, the ship is forced to move ahead with the test velocity. Considering the small value of the pitch and heave motion for the low-speed vessel, the ship is free only in the surge direction with the other five motions fixed. The ship wave pattern at Fn=0.15 in model scale is drawn in Fig 5.6. For Nagisa the code utilized for free-running test simulations, the z=0 plane locates on the undisturbed free surface. Hence, the coordinate Z in Fig 5.6 represents the wave elevation. The symmetry Kelvin wave can be seen clearly in this figure.

Then, the self-propulsion case should be carried out based on the results of the resistance case. Before that, the open-water characteristics of the propeller is simulated. The result of the open-water propeller test is shown in Fig 5.7. It is obvious that the

simulation results are in good agreement with the experimental data, which can also reveal the high quality of the body force method. Based on the calculated open-water characteristics of the propeller, the self-propulsion case is simulated. The propeller rotation speed is modified from the initial value to keep the balance of the resistance and propeller thrust. The results are shown in Fig 5.8 and Fig 5.9. Figure 5.8 shows the axial inflow velocity distribution around the wake field. The inflow velocity shown in this figure is also nondimensionalized by the vessel speed. The negative value means that the velocity direction is from the aft to the fore. Hence, the positive values on the propeller section shows clearly that the propeller pushed the water backward. The vector also shows the effect of the right-handed propeller on the flow field. The non-uniformity of flow field velocity caused by propeller rotation can be seen clearly. In Fig 5.9, the time history of the predicted propeller rotation speed is compared with the experimental one, which shows good agreement. The error between the average value of the experimental data and the steady predicted value is about 5%. Even though the simulations using the real discretized propeller can decrease the error to about 2% by some scholars (Wang et al, 2017), the large computational resources increased by the grid number and extremely small time-step make these simulations of the maneuvering in calm water and wave conditions time-costing. Hence, the simplified propeller model is adopted and utilized in present simulations. In addition, the error might come from the difference between the experiment and the simulation. For the simulations, the ship is free only in the surge motion with the other motions fixed considering the little pitch and heave motion for the target low-speed containership model.

Finally, the simulations of the ship free-running test in calm water can be conducted relying on the results of the self-propulsion case. For these simulations, six degrees of freedom are utilized to predict the ship trajectories and motions.

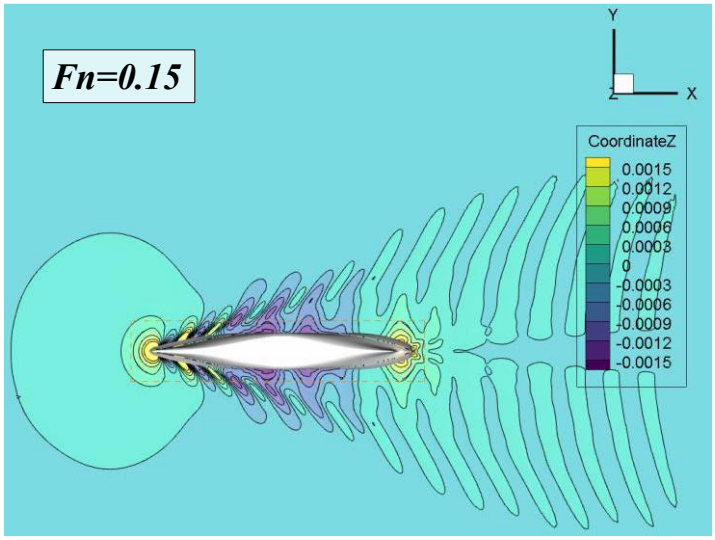

FIGURE 5.6 Computational result of ship wave pattern at Fn=0.15 in model scale

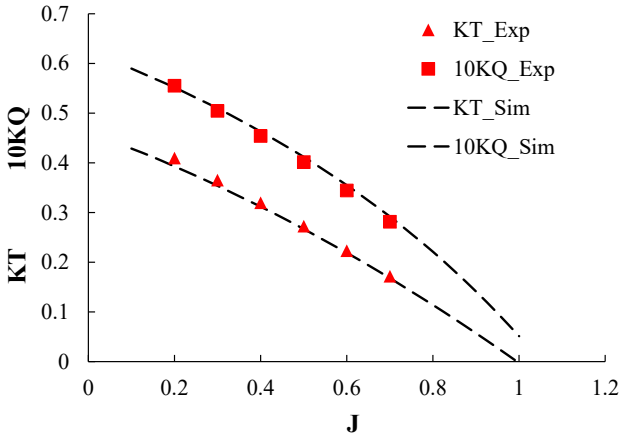

FIGURE 5.7 Open-water curve for experiments (dot) and simulations (dashed line)

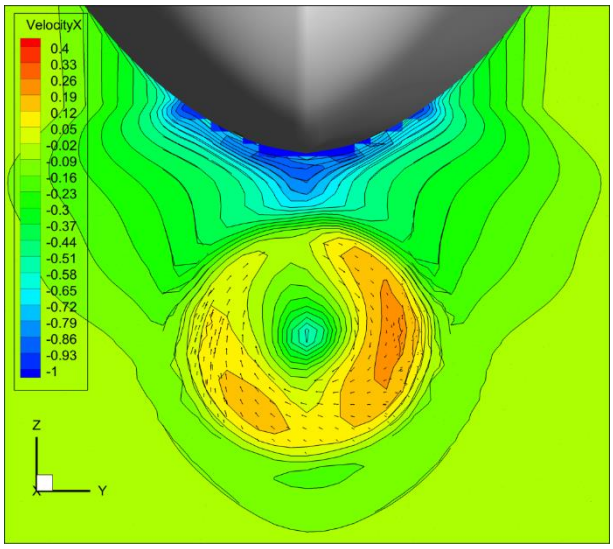

FIGURE 5.8 Axial inflow velocity distribution on the propeller section

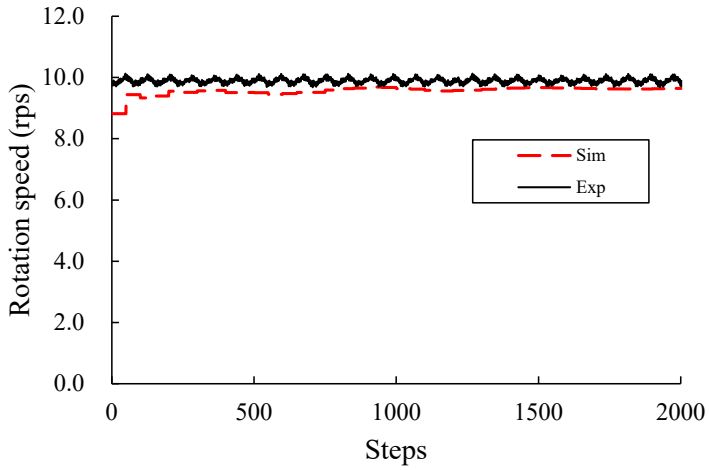

FIGURE 5.9 Comparison between the simulated propeller rotation speed and the experimental data

5.4 Results and discussions

5.4.1 zigzag tests in calm water condition

The 20/20 zigzag maneuver with the rudder speed of 13 deg/s is simulated and analyzed in this section. Fig 5.10 shows the simulated and experimental time histories of the heading angle and the rudder angle. In this figure, t denotes the physical time and the simulated CFD data is calculated using the function $t = t' L_{PP}/U$, in which t' is the nondimensionalized physical time obtained from the simulation and U is the ship initial velocity at the beginning. There are six typical positions marked as A to F respectively. Point A denotes the initial position when the rudder angle and yaw angle are zero. Point B and E represent the positions when the rudder angle reaches the specified angle to starboard and the specified angle to port side, respectively. Point C, D, and F represent the position when the heading angle reaches the maximum yaw angle, zero yaw angle, and the minimum yaw angle, respectively. These typical positions will be utilized to analyze the time histories of the forces and flow filed information later. In general, some typical parameters should be obtained and compared, which are the first overshot angle, the second overshoot angle, time to check yaw and time of a complete cycle. In terms of the heading angle prediction, there are quite small differences between the predicted magnitude value and the experimental data (0.04%) for the first cycle and slightly larger difference for the second cycle (4.44%). For the rudder period, the consistence is quite good with 2.76% difference for the first cycle and a little larger (4.15%) for the second cycle. The criteria parameters of the zigzag maneuvers are listed in Table 5.3. Good agreement between the CFD results and the experimental data is achieved in terms of the 1st overshot angle (0.13%) and the time for that (2.76%). When the ship rudder executes to the port side, especially the rudder angle keeps -20deg, the yaw rate predicted by the CFD methods seems to be underestimated. The 2nd overshoot angle predicted is overestimated by 10.30% and the time to the 2nd overshoot angle is overestimated by 4.15%. The discrepancies might come from the insufficient propeller model and the uncertainty of the measurement data. For the former, the body force method based on the potential-flow theory might ignore the strong viscous hull-propeller-rudder interaction and the propeller forces might be a little different from the experimental one. For example, the high-frequency fluctuation can be founded in the experimental data and actual rotating propeller method (Wang et al, 2018). This high-frequency fluctuation is considered to be the interaction of the blades on the flow field when rotating. For the latter, the uncertainty analysis of the experiments is not provided and the error between the simulated and experimental results should be determined considering the uncertainty level of the experimental data. Except the 2nd overshoot angle, the error for these parameters is smaller than 5%. In summary, considering the efficiency and accuracy, the present simulation results are acceptable and valuable. In Fig 5.11, the yaw rate predicted by the CFD method is presented and compared with the experimental results. The predicted yaw rate is

calculated based on $r = r'U/L_{pp}$. At the beginning, the predicted yaw rate agrees well with the experimental time history of the yaw rate. With the rudder executing to the port side, especially $12s \le t \le 17s$, the difference seems to be larger, resulting in the obvious error for the yaw angle in the second cycle of the zigzag test.

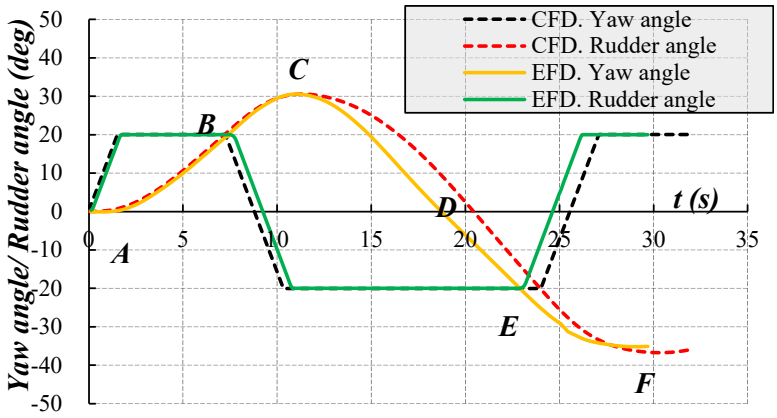

FIGURE 5.10 Yaw and rudder angle for the 20/20 maneuver in calm water condition

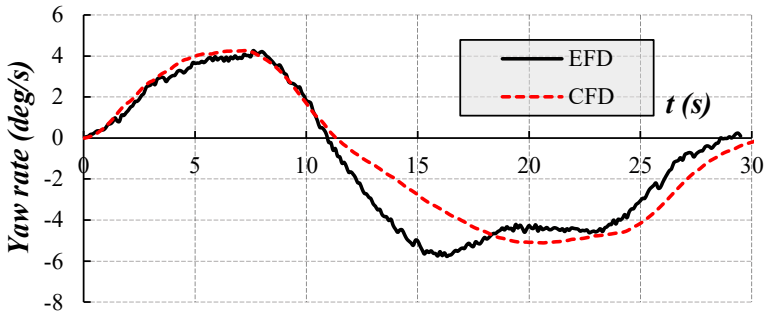

FIGURE 5.11 Yaw rate for the 20/20 maneuver in calm water condition

TABLE 5.3 Comparison of main parameters for 20/20 zigzag maneuver in calm water condition with rudder angle of 13deg/s

Parameters	EFD	CFD	Error
1st overshoot angle (deg)	10.53	10.54	0.13%
Time (1st overshoot angle) (s)	11.00	11.30	2.76%
2nd overshoot angle (deg)	15.19	16.76	10.30%
Time (2nd overshoot angle) (s)	29.10	30.31	4.15%

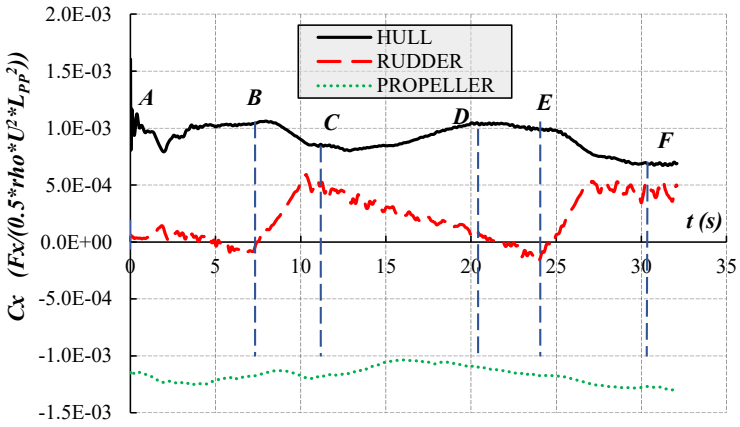
HULL
RUDDER
PROPELLER
A
B
C
D
E
F
t (s)
Cx (Fx/(0.5*rho*U^2*L_PP^2))
2.0E-03
1.5E-03
1.0E-03
5.0E-04
0.0E+00
-5.0E-04
-1.0E-03
-1.5E-03
0
5
10
15
20
25
30
35

(a)

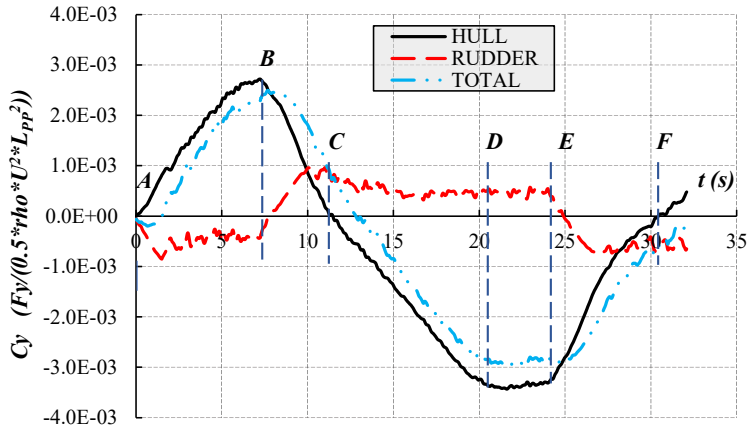
HULL
RUDDER
TOTAL
A
B
C
D
E
F
t (s)
Cy (Fy/(0.5*rho*U^2*L_PP^2))
4.0E-03
3.0E-03
2.0E-03
1.0E-03
0.0E+00
-1.0E-03
-2.0E-03
-3.0E-03
-4.0E-03
0
5
10
15
20
25
30
35

(b)

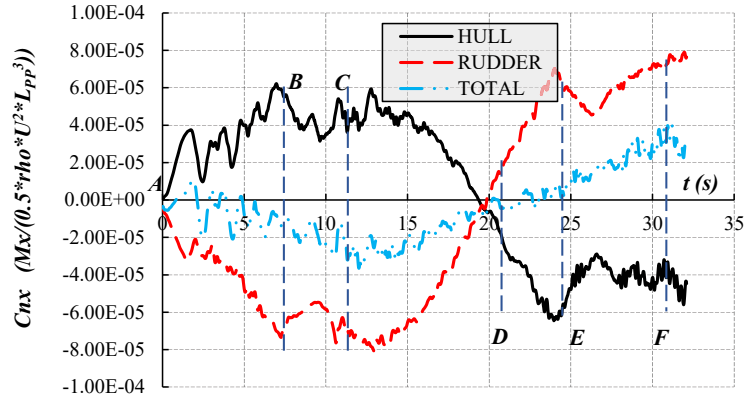
HULL
RUDDER
TOTAL
A
B
C
D
E
F
t (s)
Cnx (Mx/(0.5*rho*U^2*L_PP^3))
1.00E-04
8.00E-05
6.00E-05
4.00E-05
2.00E-05
0.00E+00
-2.00E-05
-4.00E-05
-6.00E-05
-8.00E-05
-1.00E-04
0
5
10
15
20
25
30
35

(c)

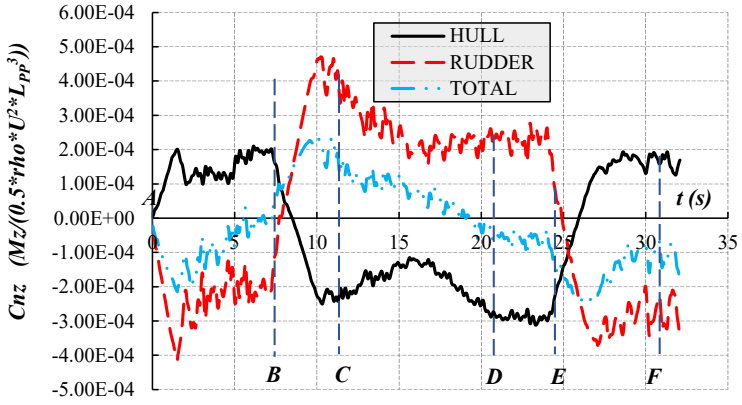

(d)

FIGURE 5.12 Non-dimensional forces and moments for the 20/20 maneuver in calm water condition (a: longitudinal force; b: lateral force; c: moment in the roll motion; d: moment in the yaw motion)

Fig 5.12 presents the time histories of longitudinal forces, lateral forces, roll moments and yaw moments on the hull and rudder in the ship-fixed coordinate system. The forces and moments are nondimensionalized through the functions: $C_x = F_x/\left(0.5\rho U^2 L_{PP}^2\right)$ and $C_{nz} = M_z/\left(0.5\rho U^2 L_{PP}^3\right)$. For the longitudinal direction, the propeller force is also considered. The total force in this figure represents the sum of the hull force and rudder force. As can be seen from this figure, the forces on the hull take the main parts of the resistance and lateral forces. However, the yaw moment created by the rudder takes larger proportion of the total yaw moment due to the longer arm of the forces even though the longitudinal and lateral forces on the rudder are smaller than those on the hull.

When the rudder executes to starboard (from A to B), the rudder lateral force points to the port side, which makes a large negative yaw moment on the rudder as shown in Fig 5.12(d). The ship is forced to turn to starboard by this negative yaw moment. Then, the positive yaw moment and lateral force on the hull are generated by reaction force of the water for the ship motion. When the rudder angle reaches the maximum specified value and keeps it, the ship yaw angle will increase due to the negative yaw moment. The longitudinal and lateral force on the rudder decrease during this period. When the rudder starts to turn to port side (Point B to Point C), the rudder yaw moment and lateral rudder force will change from the negative values to the positive ones. From the Point C to Point D, the rudder angle keeps, and the yaw angle changes from the maximum angle to zero. When the ship yaw angle is zero in Point D, the yaw moment on the hull is negative and huge forcing the ship turn to port side. The rudder yaw moment is huge and positive, which makes the total yaw moment close to zero. During the period from Point D to Point E, the hull yaw moment dominates the total yaw moment rather than the rudder in the other periods. By comparing the Point A with the Point D, it is clear that even though the yaw angle is the same, the lateral force at Point D is totally different from that at the Point A due to the large hull yaw moment and the different flow filed. The rudder starts to turn to starboard at Point E, the rudder yaw moment rapidly

decreases from the positive value to the negative. The lateral forces on the rudder at Point B and E are the extreme points. It can be seen that for this 20/20 zigzag maneuvers, the dominant part of the yaw moment is the rudder yaw moment at most times. For the rudder, the absolute values of Cy when the rudder in port side and those when the rudder locates starboard are close, which reveals the symmetry of the rudder force. So is the yaw moment coefficient on the rudder Cnz.

In addition, during the zigzag maneuver, there is an obvious speed loss phenomenon shown in Fig 5.13. The increased resistance due to the drift angle and the motions might contribute greatly to the 20% decrease of the vessel speed. When the propeller rotation speed is fixed and the rudder is executed frequently, the ship speed will decrease inevitably.

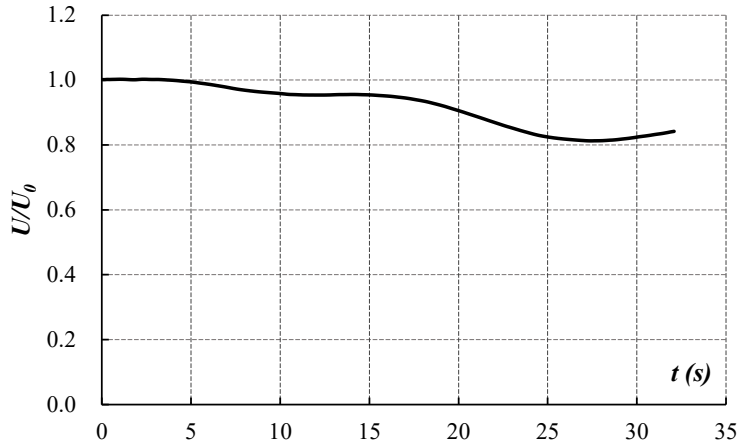

FIGURE 5.13 Dimensionless velocity for the 20/20 maneuver in calm water

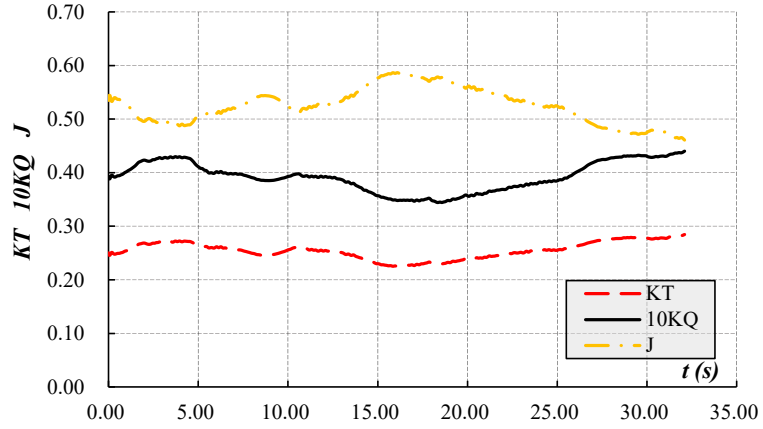

FIGURE 5.14 K_T and $10K_Q$ for the 20/20 maneuver in calm water

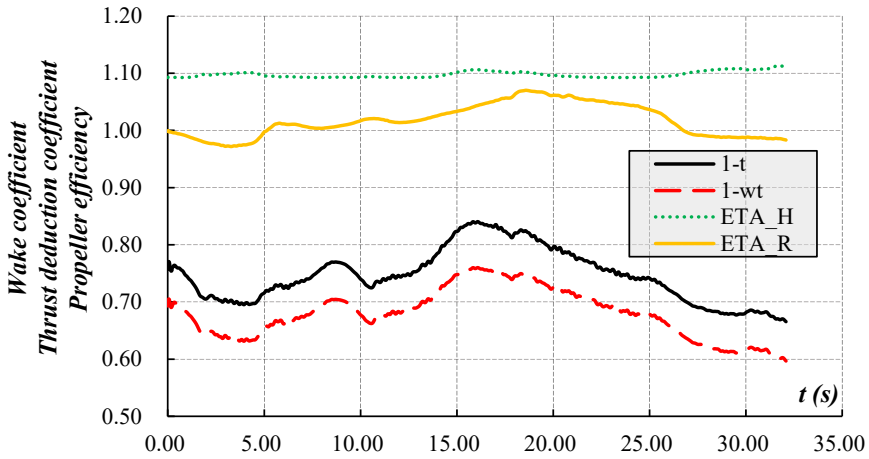

FIGURE 5.15 Self-propulsion factors for the 20/20 maneuver in calm water

To gain more insight into the effect of the propulsion system during the zigzag maneuver, the propeller thrust coefficient K_T, the torque coefficient K_Q, and the advance coefficient J are shown in Fig 5.14. K_T is defined as $K_T = T/\rho n^2 D^4$, K_Q is calculated using the equation $K_Q = Q/\rho n^2 D^5$ and J is defined as $J = V_A/nD$. T and Q represent thrust and torque of the propeller. V_A is the advance speed of the propeller, n is the propeller rotation speed in revolutions per second and D represents the diameter of the propeller. The time histories of self-propulsion factors are drawn in Fig 5.15. Due to the added resistance by the propeller, the thrust deduction fraction can be obtained using $t = (Thrust\text{-}Resistance)/Thrust$. The wake fraction reflecting the hull effect on the propeller can be computed by $\omega_t = 1 - V_A/U$. The hull efficiency for propulsion can be calculated by $\eta_H = (1-\omega_t)/(1-t)$ reflecting the interaction between the hull and propeller. The relative rotative efficiency of the ship propeller respect to the open water propeller is computed from $\eta_R = K_{Q0}/K_Q$ reflecting the nonuniformity of wake. K_{Q0} is calculated in the open-water condition. The thrust and torque have the same low-frequency fluctuation. Both thrust and torque are evidently related to the ship motions and rudder execution. When the rudder executes, the thrust and torque of the rotating propeller will show significant difference, which is mainly due to the large flow disturbance around the propeller caused by the rudder. Even though the vessel speed decreased in a fluctuating way, the advance coefficient J will not decrease following it all the time. The advance coefficient is determined by the ship motion and the wake flow field influenced by the hull, propeller and rudder simultaneously. In addition, the zigzag maneuver can cause the advance coefficient to fluctuate in the range of 20% of the average value in this case. The advance coefficient is negatively correlated with thrust and torque. $1-t$ and $1-\omega_t$ are positively correlated with the advance coefficient J.

Hence, the hull efficiency for propulsion η_H keeps constant during the zigzag maneuvers. The time history of the relative rotative efficiency of the ship propeller η_R shows that the nonuniformity of wake also changes with time.

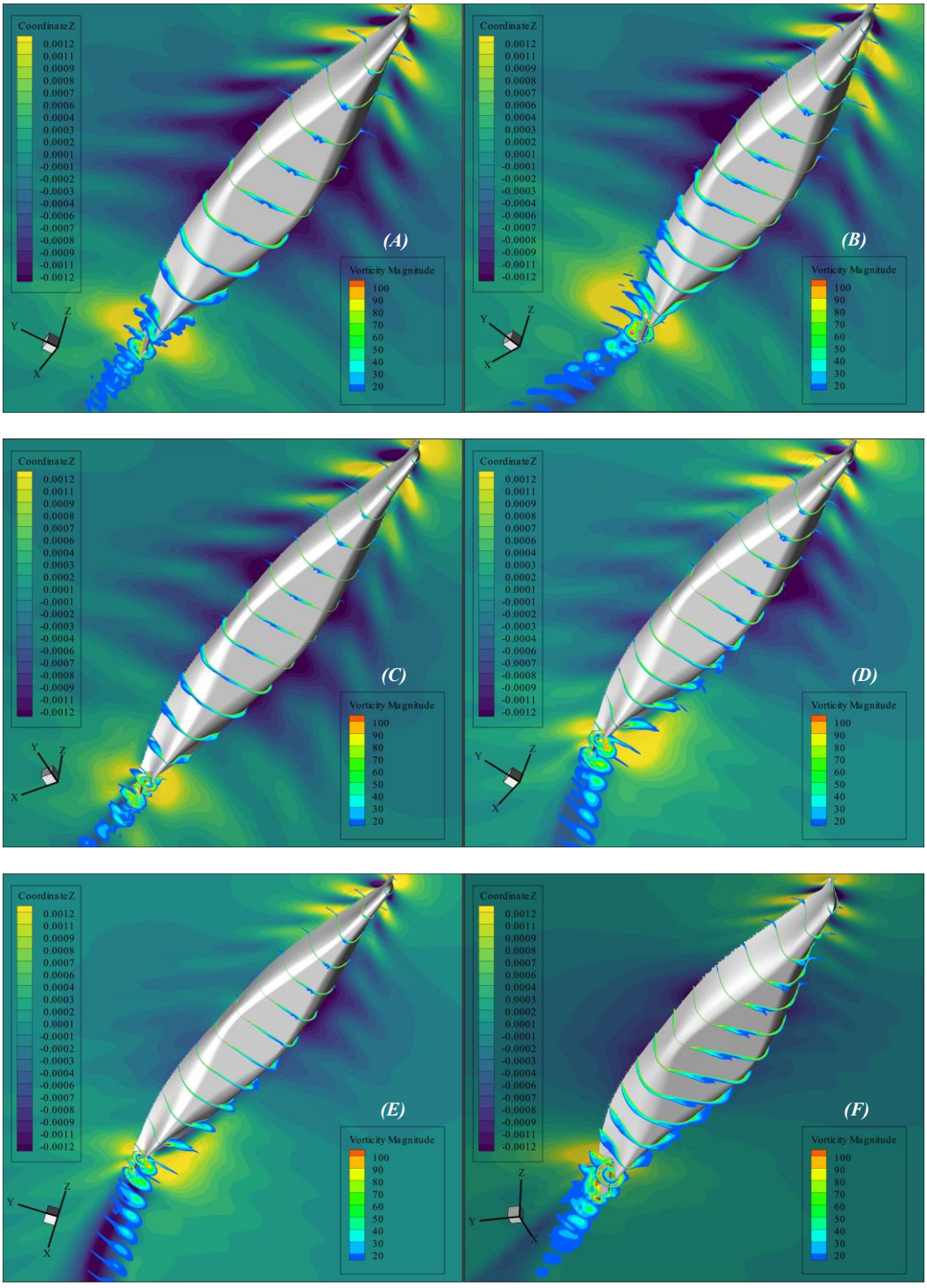

FIGURE 5.16 Snapshots of free surfaces colored by wave elevation and cross sections colored by vorticity magnitude during the 20/20 maneuver in calm water condition

Fig 5.16 shows the vorticity magnitude on significant sections and the wave elevation on the free surface during the zigzag maneuver in calm water condition. The sequence of pictures provides a clear representation of the flow evolution along the hull during the zigzag maneuver motions. The formation of large vorticial structures detaching from the hull as well as strong vortex/vortex and vortex/boundary layer interactions are shown in this figure. There are 12 equidistant sections on the hull and 7 equidistant sections from the after perpendicular of ship to 0.3L behind the hull. In Fig 5.16(A), the initial boundary layer is close to the self-propulsion case in calm water. A relatively weak vortex detaches from the bulbous bow and transports downstream following the hull. The vortex magnitude increases toward the stern. Particularly strong vortices are generated at the propeller and rudder. These vortices merge with the bulbous bow vortex to generate a complex wake near the free surface. Due to the symmetry of the hull and rudder, the vortices also show clear symmetry. When the rudder executes to starboard and keeps the 20deg till the yaw angle reaches 20deg (Fig 5.16(B)), the bulbous bow vortex on the starboard is much larger than that on the port side. The behind-hull vortices as well as the wake deflect towards the starboard. When the rudder executes to port side and the yaw angle reaches the maximum value (Fig 5.16(C)), the asymmetry of the vortex on the starboard and port side seems to be smaller compared with Fig 5.16(B) even though the yaw angle is larger. The larger hull yaw angle can cause the stronger vortices on the starboard and clear wake deflecting towards the starboard. However, the rudder angle deflecting to the port side has the contrary effect on the flow filed and the hull yaw angular velocity is zero at this point, which makes the flow filed closer to that shown in Fig 5.16(A). In Fig 5.16(D), the vortices on the port side are much stronger than those on the starboard even though the hull yaw angle is zero. It is due to the large yaw angular velocity and the rudder angle. Then, the vorticity distribution in Fig 5.16(E) is approximately symmetrical to that in Figure 5.16(B) about the longitudinal section of the ship. Finally, the deflection of tail vortices will be decreased when the ship yaw angular velocity close to zero in Fig 5.16(F), which is the same as that in Fig 5.16(C).

The pressure on the rudder is drawn in Fig 5.17, which indicates that the pressure distribution on the rudder is mainly related to the rudder angle. When the rudder deflects towards the starboard at point B and F, there is a low-pressure region on the port side of the rudder. When the rudder deflects towards the port side at point C, D and E, there is a low-pressure region on the starboard of the rudder. The pressure distributions at point D and E are similar, which corresponds to the time history of the lateral force coefficient C_y and yaw moment coefficient C_{nz} shown in Fig 5.12.

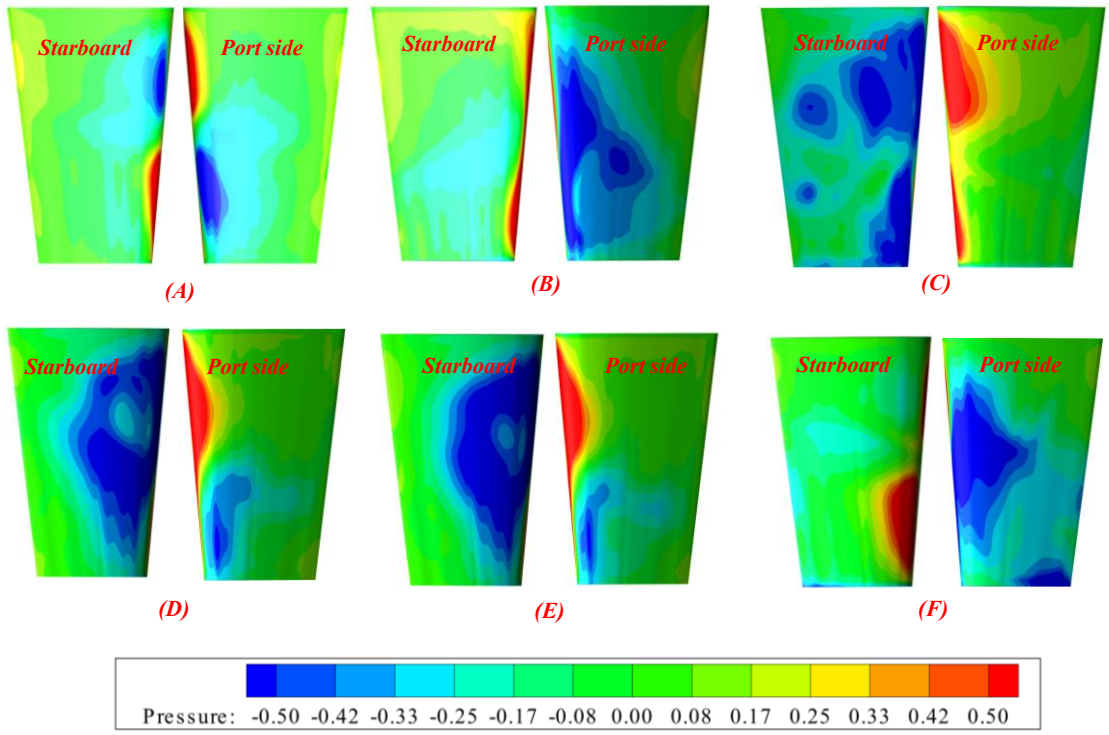

FIGURE 5.17 Snapshots of pressure on the rudder during the 20/20 maneuver in calm water condition

5.4.2 turning tests in calm water condition

The turning maneuver with the rudder speed of -13deg/s to the rudder angle of -35deg was simulated. The trajectory of the turning circle is shown in Fig 5.18. Some typical parameters for the turning circles should be defined to assess the turning ability. Advance x_{90} denotes the longitudinal distance from the initial point to the point when the heading angle change is 90 deg. Transfer y_{90} represents the lateral distance from the initial point to the point when the heading angle change is 90 deg. Steady turning radius means the radius of the steady turning circle. Similarly, x_{180} and y_{180} can also be defined to conduct the validation. T_{90} and T_{180} represent the time from the beginning of the rudder execution to the time when the heading angle changes are 90 deg and 180 deg, respectively. The results are summarized in Table 5.4. The tactical diameter error for this case is 2.78% and the predicted advance is a little larger with 5.50% error compared with the experimental data. These errors might come from the difference between the experiments and the simulation setup and the insufficient performance of the propeller model. In addition, the present simulation strategy still has some room for improvement considering resolving the large flow separation with such considerable rudder angle. Overall, the simulation strategy using the body force method to calculate the propeller force and the overlapping grid technology to deal with the

multiple motions can deal with the problem of simulating the turning motion. The comparison between the experimental and simulated trajectory indicates that the present simulation method can predict the turning maneuver with satisfying accuracy. The time histories of the yaw rate and dimensionless velocity are drawn in Fig 5.19 and Fig 5.20, respectively. The comparisons also validate the efficiency of the present simulation method. A clear speed loss phenomenon is shown in Fig 5.20. Compared with that of the zigzag test simulation, the speed loss of the turning test simulation is much larger with a 50% decrease of the initial vessel speed.

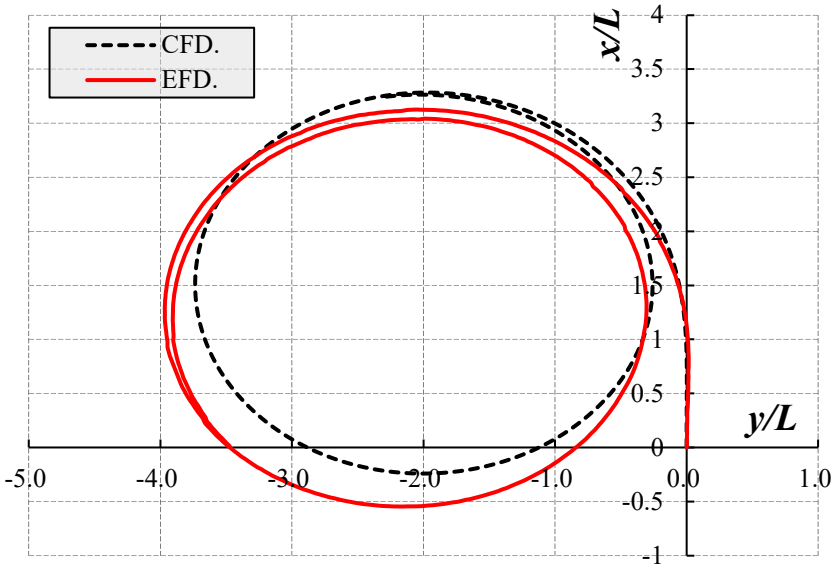

FIGURE 5.18 Trajectory of the ship turning maneuvers in calm water condition

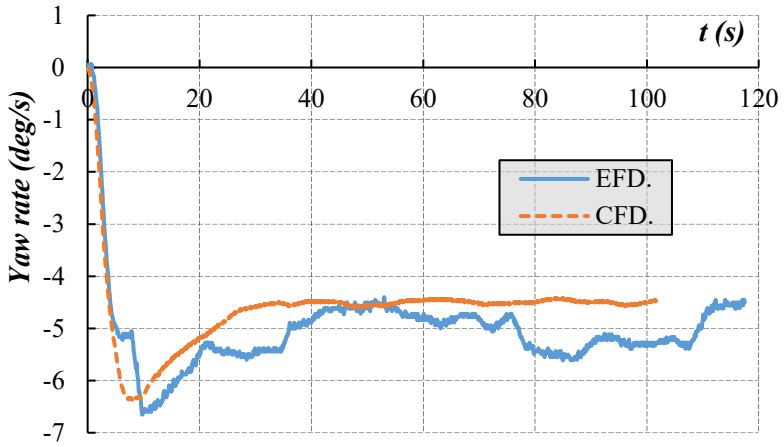

FIGURE 5.19 Yaw rate for the turning maneuver in calm water condition

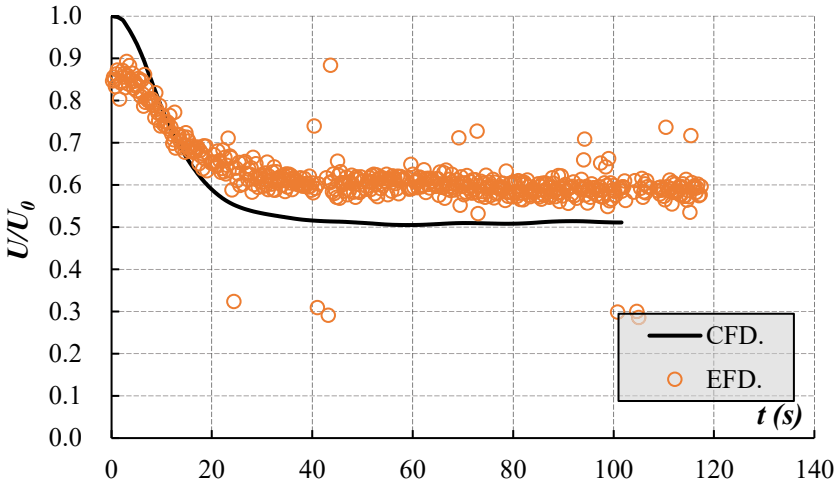

FIGURE 5.20 Dimensionless velocity for the turning maneuver in calm water condition

TABLE 5.4 Comparison of main parameters for the turning maneuver in calm water condition with rudder angle of 13deg/s

Parameters	EFD	CFD	Error
Advance x_{90} (m)	3.07	3.24	5.50%
Transfer y_{90} (m)	1.56	1.57	0.85%
x_{180} (m)	1.87	1.90	6.38%
y_{180} (m)	3.86	3.69	4.40%
Steady turning radius (m)	3.60	3.50	2.78%
T_{90} (s)	18.2	17.97	1.25%
T_{180} (s)	34.6	36.8	6.38%

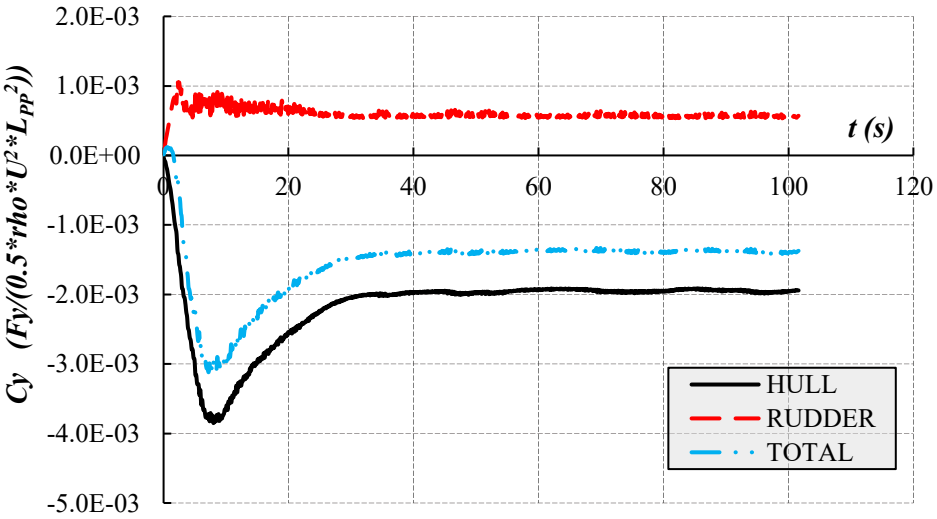

(a)

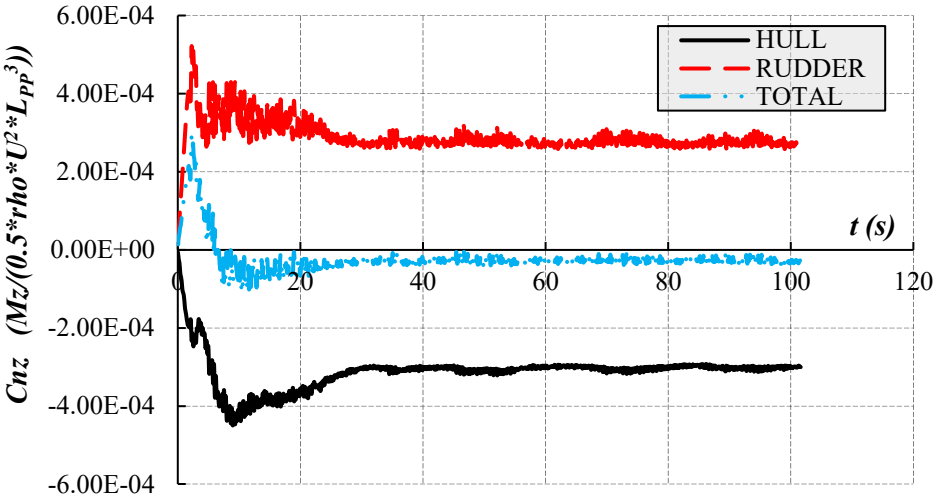

(b)

FIGURE 5.21 Non-dimensional forces and moments for the -35deg turning maneuver in the calm water condition (a: lateral force; b: yaw moment)

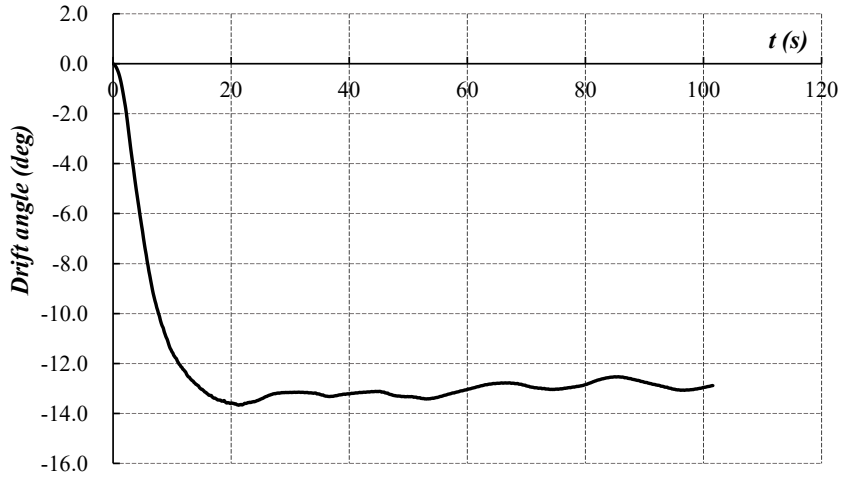

FIGURE 5.22 Drift angle for the turning maneuver in calm water condition

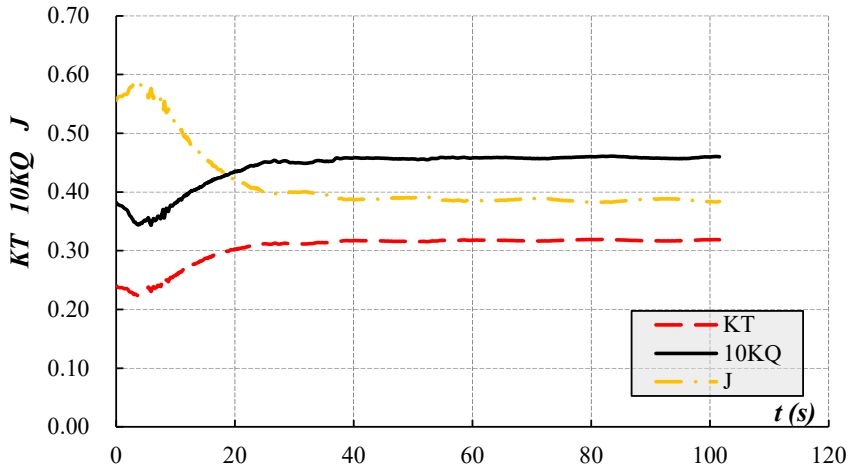

FIGURE 5.23 K_T and $10K_Q$ for the turning maneuver in calm water

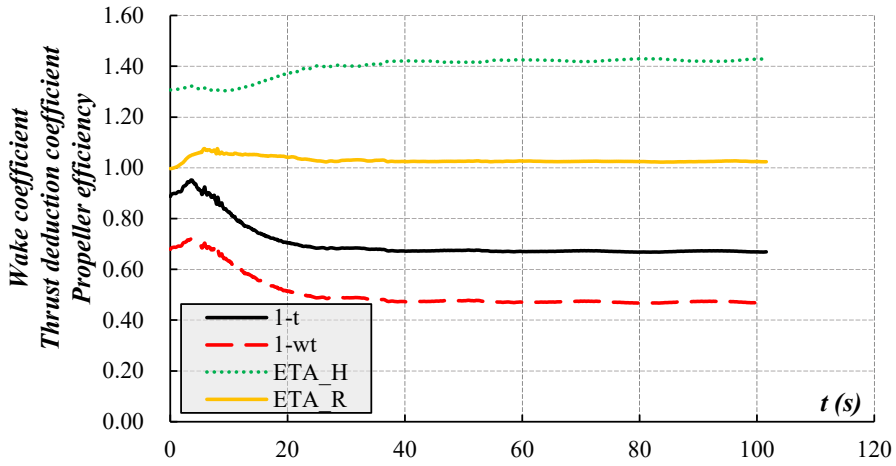

FIGURE 5.24 Self-propulsion factors for the turning maneuver in calm water

The time histories of the lateral forces and yaw moments on the hull and rudder are drawn in Fig 5.21. In general, there are three stages during the turning circle motions, which are the rudder execution stage, the transition stage, and the steady turning stage. For this simulation, the first stage is from 0s to 2.7s, and the second stage is from 2.7s to about 30s, and the stage after 30s belongs to the steady turning stage. The lateral force on the rudder increase rapidly at the rudder execution stage and the lateral force on the hull increases due to the drift angle of the hull. The peak of the lateral force on the hull comes later than that on the rudder because of the increasing drift angle shown in Fig 5.22. The yaw moment on the rudder also increases rapidly at the first stage and comes to the peak earlier than that on the hull. The difference between the yaw moments on the rudder and hull is much smaller than that between the lateral forces. A clear decrease can be seen in the time history of the lateral force during the transition stage. It is because the increase of the yaw angle will cause an increasing yaw moment to decrease the yaw motion. The lateral component of this moment reduces the C_{ny}. Hence, the similar decrease can be seen in the time histories of the yaw angle and C_{nz} but not in the drift angle.

To gain more insight into the effect of the propulsion system during the turning maneuver, the propeller thrust coefficient K_T, the torque coefficient K_Q and the advance coefficient J are shown in Fig 5.23. The time histories of self-propulsion factors are drawn in Fig 5.24. For the rudder execution stage, the thrust and torque decrease a little due to the increase of the advance coefficient J. $(1-t)$ and $(1-\omega_t)$ increase slightly. During the transition stage, the advance coefficient decreases significantly owing to the speed loss. Hence, the thrust and torque will increase with over 30% of the initial values. $(1-t)$ and $(1-\omega_t)$ have the contrary change trend. Compared with those in the zigzag tests, the variation ranges of the coefficients in the

turning tests increase much more significant. Finally, during the steady turning stage, all these parameters are constant as expected.

Fig 5.25 shows the vorticity magnitude on significant sections and the wave elevation on the free surface during the turning maneuver in the calm water condition. The sequence of pictures provides a clear representation of the flow evolution along the hull during the turning maneuver motions. There are also 12 equidistant sections on the hull and 7 equidistant sections from the after perpendicular of ship to 0.3L behind the hull. In Fig 5.25(A), the initial boundary layer is close to the self-propulsion case in calm water. When the rudder executes to the port side and keeps the -35deg till the turning motion steady, the vortices distribution is shown in Fig 5.25(B). There are much stronger vortices on the port side (leeward side) compared with those on the starboard due to the ship drift angle and the yaw motion. The transverse flow comes from the windward side (starboard) to the leeward side (port side). The tail vortices transport downstream following the circular path. Compared with Fig 5.16(D) and Fig 5.16(E), the drift degree and strength for the vortices around the stern and wake flow seem to be larger.

The pressure distribution on the rudder during the steady turning stage is shown in Fig 5.26. Due to the larger rudder angle, the high-pressure region and the low-pressure region are larger than those in the 20/20 zigzag test.

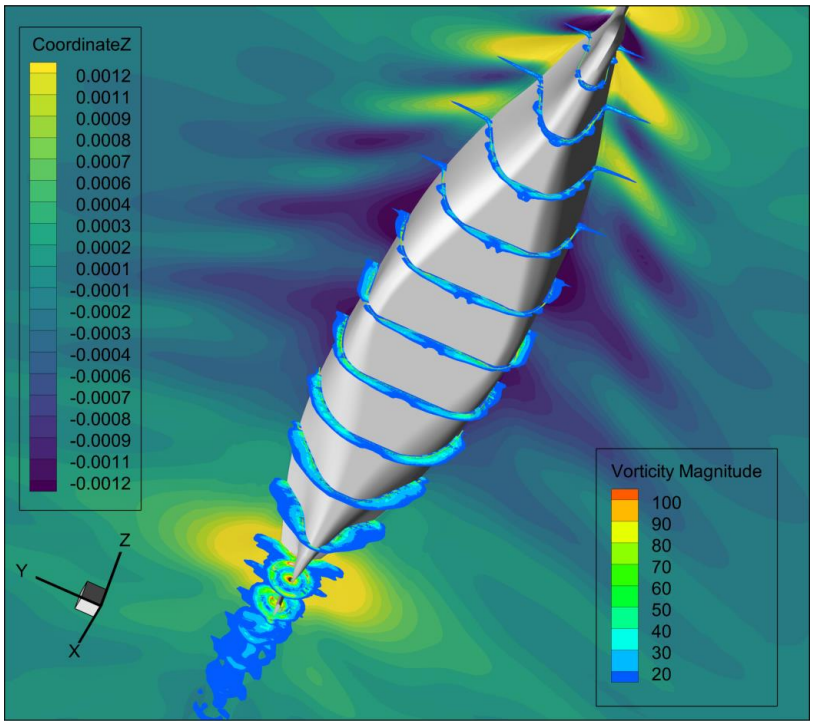

(a)

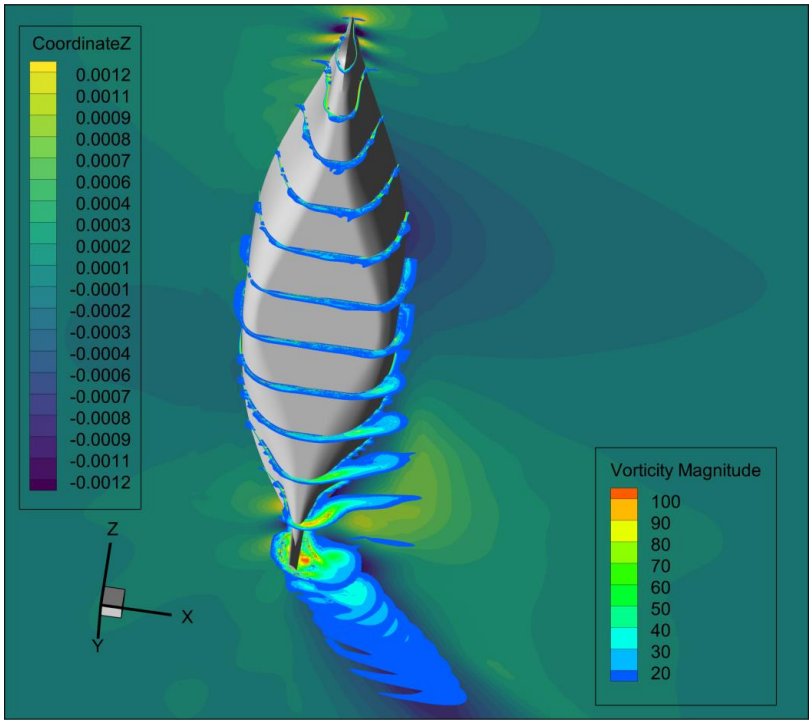

(b)

FIGURE 5.25 Snapshots of free surfaces colored by wave elevation and cross sections colored by vorticity magnitude during the turning test in the calm water condition (a) rudder execution stage (b) steady turning stage

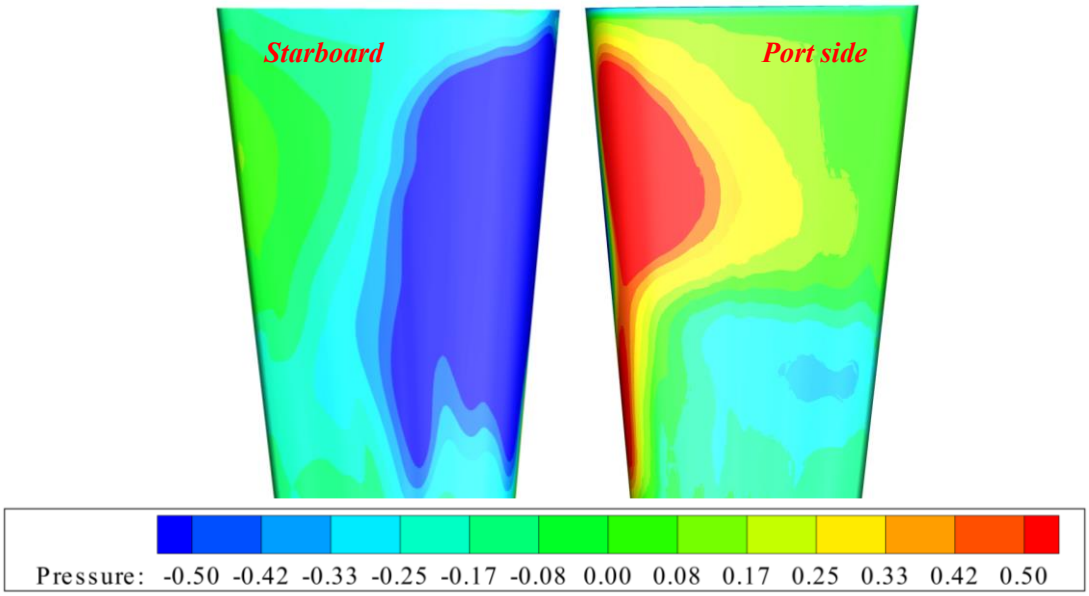

FIGURE 5.26 Snapshots of pressure on the rudder during the steady turning stage of the turning test simulation in the calm water condition

5.5 Summary

In this chapter, the numerical studies on the free-running tests in the calm water

condition for the standard model S175 containership are carried out to assess the effectiveness of the present simulation strategy. The numerical simulations are performed using an URANS code based on the dynamic overset mesh and body force techniques. The main conclusions are summarized as follows.

The present numerical simulation methods can deal with the problem of free-running test simulation efficiently and accurately. In the free-running case simulations, the body force technique can predict the propulsion forces with acceptable accuracy even though it is based on the potential flow theory ignoring the viscous effect. To minimize the calculation resources, the dynamic overset mesh is also necessary.

The ship motion and trajectory during the zigzag and turning maneuvers are predicted successfully. The time histories of the forces and moments on the hull are obtained. Propulsion forces and the rudder forces are also presented to illustrate the hydrodynamic performance during free-running tests. Flow visualizations, such as wave elevations, generation and evolution of vortices, and the pressure on the rudder are presented to give a better description of the flow variation during the maneuvers in the calm water condition.

Chapter 6 Free-running tests in waves

In this chapter, the numerical simulations on free-running tests in waves can be conducted based on the previous simulation methods in calm water condition and the wave generation and absorption method. The focus of the current research is placed on not only the ship motions but also propulsion coefficients and the rudder forces. In addition, the free-running test simulations under the regular and the long-crested and short-crested irregular wave conditions are also performed to analyze the wave effect on the maneuvering motions.

6.1 Simulation conditions

The containership S175 is the target ship of the present simulations. The principal particulars and geometry of the ship model are shown in Table 5.1 and Fig 5.1. As shown in Fig 5.2, the self-propulsion simulations in waves should be performed before the free-running test simulations in waves. The model speed is 0.818m/s corresponding to the Froude number of 0.15. The propeller rotation speed is 9.44 rps which is obtained from the self-propulsion test simulation in calm water. The experimental average rotation speed is 9.9 rps which is 5% larger than the simulated one as shown in Fig 5.9. For the purposes of comparison between the forces in calm water and waves, the same simulated propeller rotation speed 9.44rps is utilized to conduct all the simulations in waves. The regular wave is the head wave with the wavelength 0.7L and the wave amplitude 0.00742L (wave steepness H_w/λ equals to 0.021).

The turning test is carried out with the maximum rudder angle 35deg and the rudder speed 13deg/s in the head regular wave condition. The 20/20 zigzag test is also simulated with the rudder speed 13deg/s.

For the irregular wave conditions, the ISSC spectrum is adopted by NAGISA. The wave spectrum can be expressed as $S(f)=\frac{A}{f^5}\exp\left(-B/f^4\right)$, where $A=0.1107H_s^2\bar{f}^4$ and $B=0.4427\bar{f}^4$. The ISSC spectrum is a two-parameter wave spectrum based on the significant wave height H_s and the mean frequency $\bar{f}$. The significant wave height of 4.5 meter and 0.122 1/s mean frequency for the full scale, corresponding to the sea state 6, are adopted in present simulations. The short-crested irregular wave is also considered in the present research. Compared with the long-crested irregular wave, the short-crested one is obtained by multiplying the long-crested irregular wave spectrum $S(f)$ with the directional spectrum $G(\theta)$ whose function is $G(\theta)=2/\pi\cos^2\theta$.

6.2 Numerical simulations

As mentioned in section 5.1, the grid and boundary conditions are the same as those under the calm water conditions, which are not described here again. Before the free-running test simulations in waves, the self-propulsion simulations in different wave conditions should be performed to obtain the flow field information as the initial conditions for the maneuver simulations. The snapshots of the free surfaces are shown in Fig 6.1. A clear kelvin wave can be seen in the regular head wave condition but not obvious in the irregular head wave condition for the much higher irregular wave amplitude (significant value). For these simulations, the propeller rotation speed is fixed rather than modified to balance the resistance and propulsion as the self-propulsion case in the calm water condition. When the wave covers all the calculation domain, the simulations can be finished. Then, the free-running test simulations can be carried out based on the flow filed information.

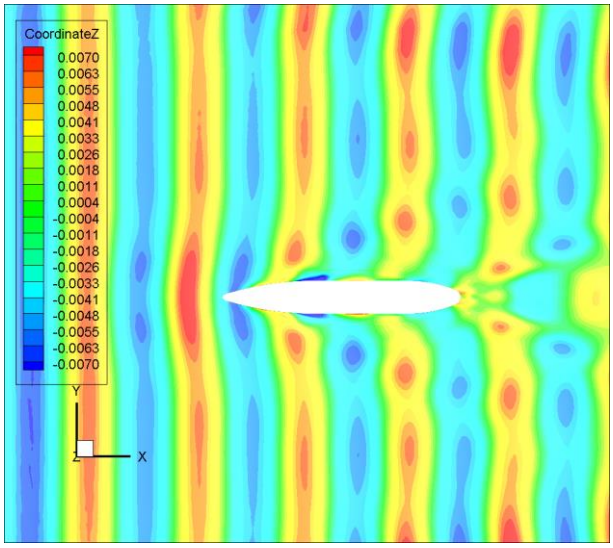

(a)

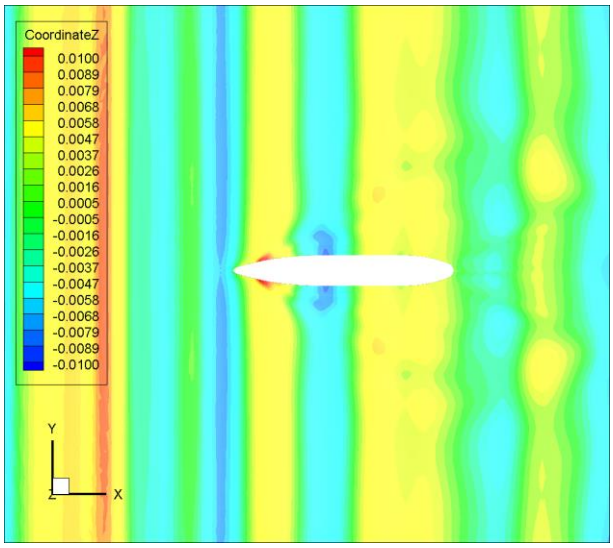

(b)

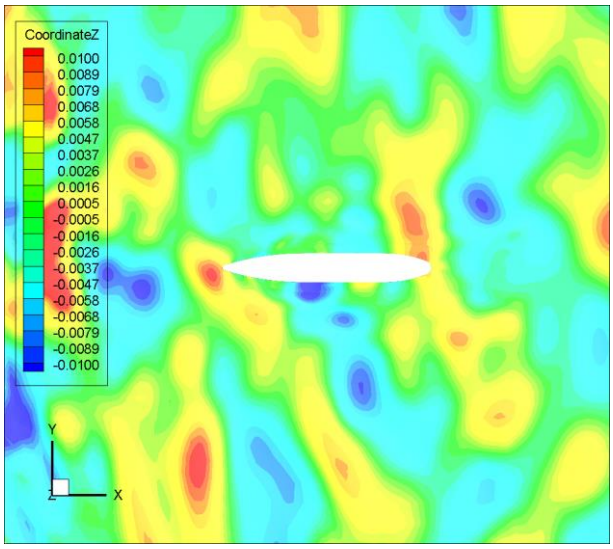

(c)

FIGURE 6.1 Snapshots of free surface for the self-propulsion cases in waves (a) regular wave condition (b) long-crested irregular wave condition (c) short-crested irregular wave condition

6.3 Results and discussions

6.3.1 course-keeping tests in irregular waves

The course-keeping ability is important for the economy and navigation safety of ship operation at seas. Compared with the zigzag test and turning circle test, the course-keeping test need less time to analyze the hydrodynamic phenomenon because of the high-frequency rudder execution. Hence, the course-keeping test is utilized to conduct the simulations in waves first. Considering that the head regular wave and head long-crested irregular wave are symmetry about the longitudinal section of the ship. The yaw angular velocity will be slight making the rudder angle tiny. To obtain an obvious rudder angle and yaw angle, the asymmetric environmental force is necessary. In the present study, the course-keeping test simulation in the short-crested irregular wave condition is carried out for its asymmetry.

For evaluating the course-keeping ability and keep the route automatically, a proportional-integral-derivative (PID) controller is applied to keep ship navigate in the predetermined route when the ship suffers asymmetry environmental forces to deflect. The control function is defined by the following expressions:

$$\delta = K_p \triangle\chi + K_i \int_0^t \triangle\chi dt + K_d \triangle\dot{\chi} \quad (5.1)$$

$$\triangle\chi = \chi - \chi_{con} \quad (5.2)$$

where K_p is the proportional gain, K_i is the integral gain, and K_d is the differential

time constant, χ is the heading angle, and χ_{con} denotes the target heading angle which is set to 0 deg to keep the ship advance straight. In this study, the gains are set to $K_p = -5, K_i = 0, K_d = -6$.

The trajectory of the ship is drawn in Fig 6.2, which shows that the ship can keep the predetermined route with a slight deflection. The maximum lateral drift is 0.04L. The time histories of the yaw angle and rudder angle are shown in Fig 6.3. As expected, the short-crested irregular wave will cause the yaw motion of the ship model. Due to the directional spectrum, the yaw angle will not increase or decrease monotonically. There will be some high-frequency fluctuations on the time history of the yaw angle. The sign of rudder angle is basically opposite to that of heading angle to ensure the yaw angle close to zero. Some scholars have simulated the course-keeping tests in regular head waves and calm water conditions (Kim et al, 2021b; Wang and Wan, 2018). They found the symmetry wave loads cause little yaw motion whose maximum value is smaller than 1deg. However, for the short-crested irregular wave condition simulated here, the maximum value of the yaw angle reaches 20deg and the maximum rudder angle up to 3deg.

Non-dimensional forces and moments for the course-keeping maneuver in short-crested irregular waves can be obtained and drawn in Fig 6.4. For all the forces, the hull forces are the dominant parts. The amplitudes of the high-frequency fluctuations on the longitudinal force, lateral force, and the yaw moment are extremely large compared with the low-frequency values.

Fig 6.5 shows the time history of the vessel speed. The speed loss comes from the wave added resistance and the yaw motions. The speed seems to be steady after 12s for the balance between the ship resistance and the propulsion force.

As for the propeller coefficients and the self-propulsion factors, they are drawn in Fig 6.6 and Fig 6.7. For the advance coefficient J, it decreases due to the drop of the vessel speed. The amplitude of the high-frequency wave-induced fluctuation is about 20% of the average value. The thrust and torque also have significant fluctuations. The variations of the low-frequency parts due to the rudder and ship motion for these parameters are not obvious. On the contrary, the self-propulsion parameters changed significantly not only for the high-frequency components but also for the low-frequency ones, except the relative rotative efficiency η_R. It is because the waves will have a significant impact on the flow field near the propeller.

The vorticity magnitude on significant sections and the wave elevation on the free surface during the course-keeping maneuver is drawn in Fig 6.8. By comparison, the vortex structure and the strength seem to be close to the zigzag maneuver. The free surface varies greatly without a clear wave crest and trough.

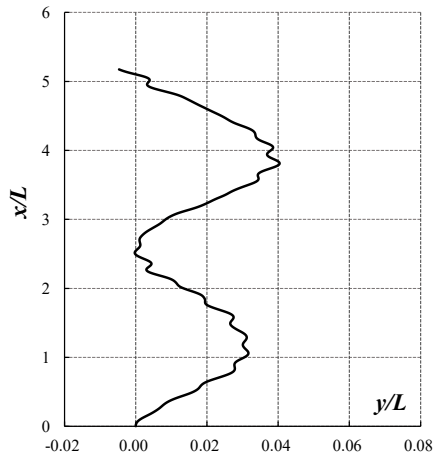

FIGURE 6.2 Trajectory of the course-keeping simulation in short-crested irregular waves

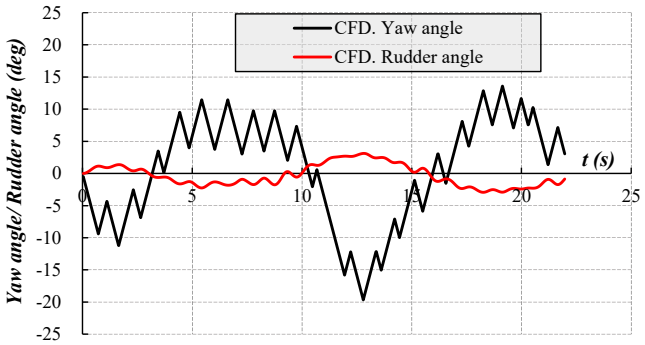

FIGURE 6.3 Time histories of the yaw and the rudder angle for the course-keeping simulation in short-crested irregular waves

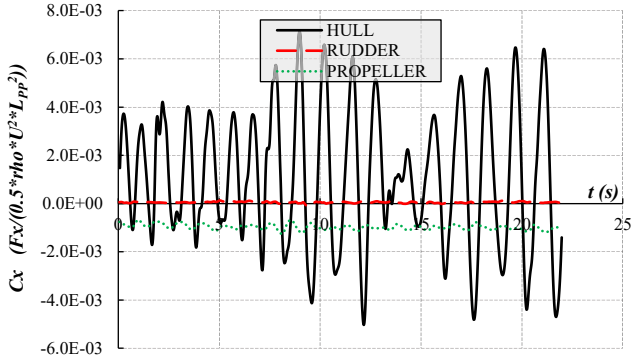

(a)

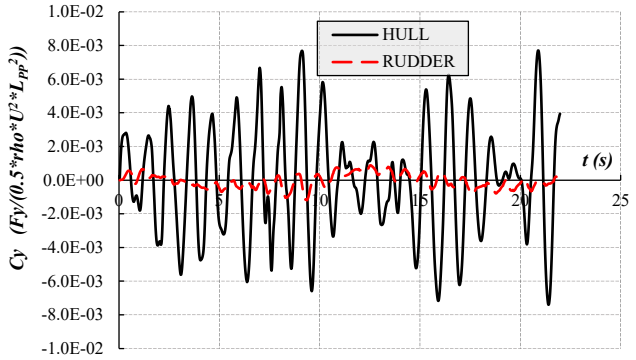

(b)

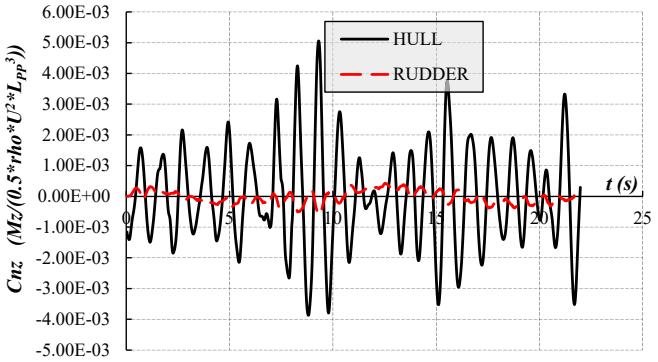

(c)

FIGURE 6.4 Non-dimensional forces and moments for the course-keeping maneuver in short-crested irregular waves (a: longitudinal force; b: lateral force; c: yaw moment)

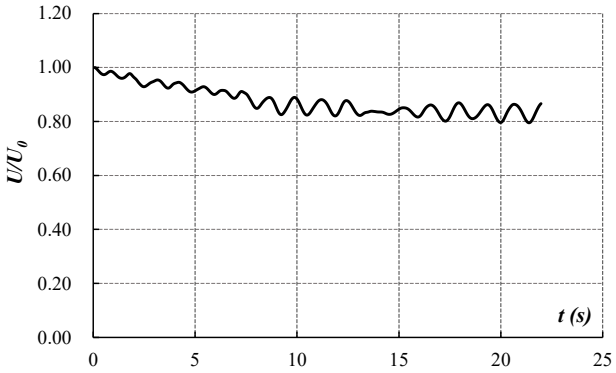

FIGURE 6.5 Non-dimensional velocity for the course-keeping maneuver in short-crested irregular waves

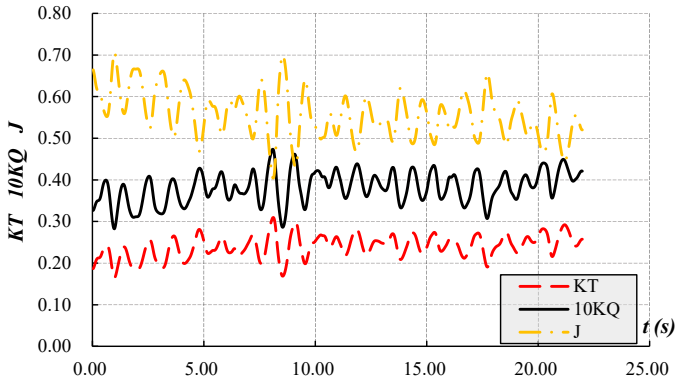

FIGURE 6.6 K_T and $10K_Q$ for the course-keeping maneuver in irregular waves

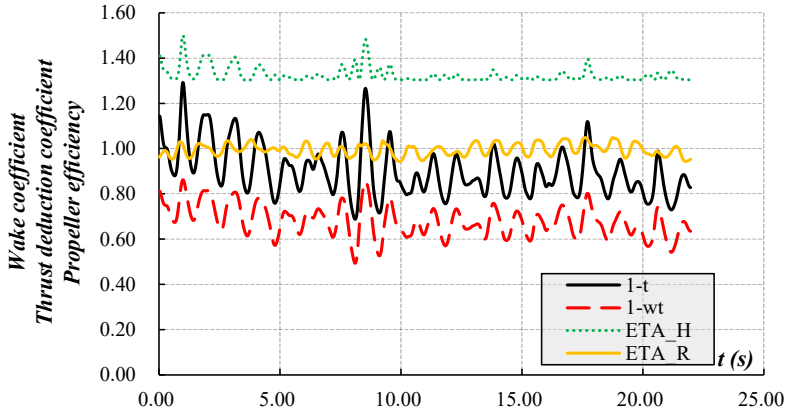

FIGURE 6.7 Self-propulsion factors for the course-keeping maneuver in irregular waves

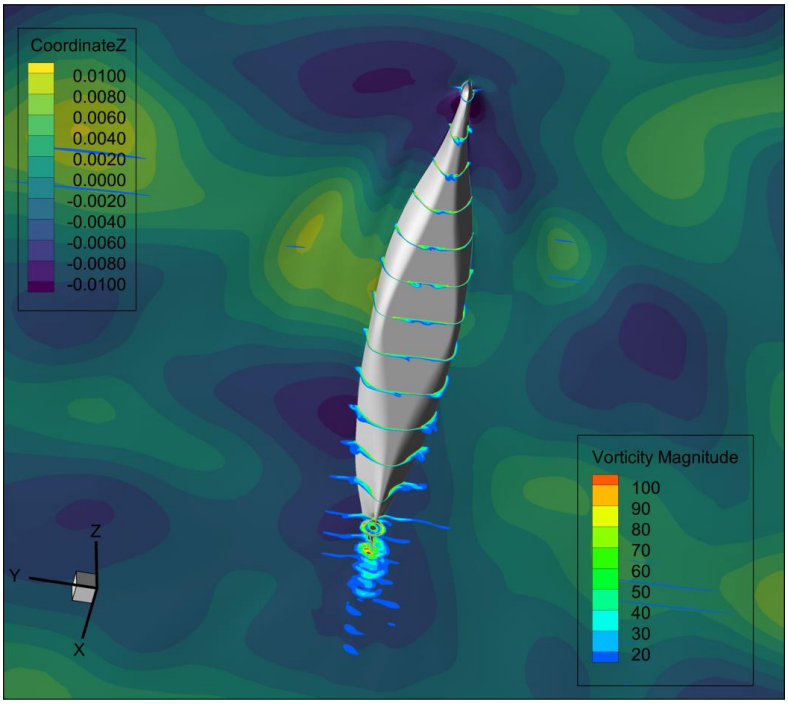

FIGURE 6.8 Snapshots of the free surface colored by wave elevation and cross sections colored by vorticity magnitude during the course-keeping maneuver

6.3.2 zigzag tests in regular waves

The 20/20 zigzag maneuver is simulated with the rudder speed of 13 deg/s under the head wave condition ($\lambda/L = 0.7$, $H = 0.045m$ for the model scale). Fig 6.9 shows the computational and experimental time histories of the heading angle and the rudder angle. There are also six typical positions marked as A to F, respectively. In terms of the heading angle prediction, there are acceptable differences between the computational and the experimental magnitude value for the first cycle (5.09%) and the second cycle (2.69%). The criteria parameters of the zigzag maneuvers are listed in Table 6.1. Good agreement between the CFD results and the experimental data is

achieved. In Fig 6.10, the yaw rate predicted by the CFD method is presented and compared with the experimental results. The predicted one agrees well with the experimental time history of the yaw rate. Compared with the yaw rate in the calm water condition, there are high-frequency fluctuations caused by the regular wave.

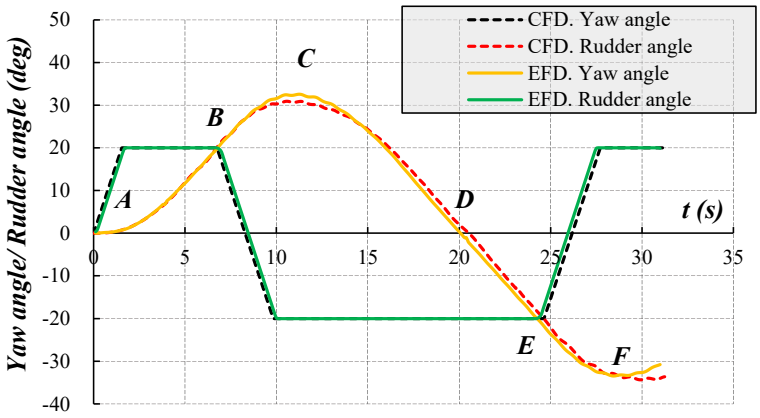

FIGURE 6.9 Yaw and rudder angle for the 20/20 maneuver in regular head waves

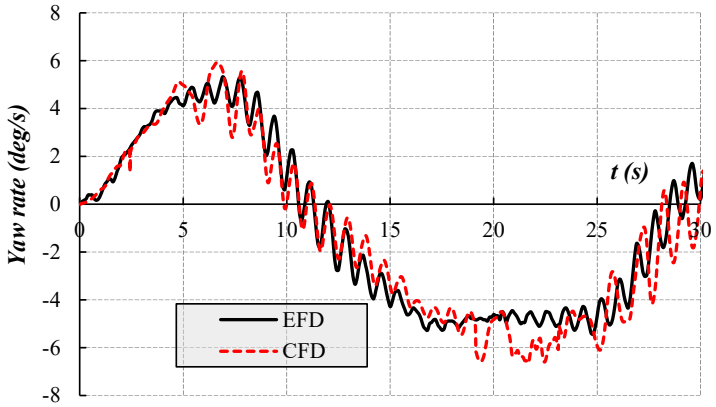

FIGURE 6.10 Yaw rate for the 20/20 maneuver in regular head waves

During the zigzag maneuver, there is also a speed loss phenomenon as shown in Fig 6.11. The propulsion thrust does not change significantly shown in Fig 6.12. The increased resistance comes from the drift angle, huge ship motions, and the wave added forces. As expected, the ship speed loss is much more obvious than that in the calm water condition.

Fig 6.12 and Fig 6.13 show the parameters related with the propulsion. Compared with the time histories of these parameters in the calm water condition, those in regular waves have high-frequency fluctuations, which is caused by the periodic changes of the flow field due to waves. Not only the variation trends but also the values of low-frequency parts of the time histories of these factors are close to those in the calm water condition.

Fig 6.14 shows the vorticity magnitude on significant sections and the wave elevation on the free surface during the zigzag maneuver in regular head waves. Compared with Fig 5.16 shown the formation and transportation of the vortices, the

results under waves in this figure are similar, except that the generation of vortices near the free surface and the complexity of tail vortices are stronger. In addition, except Kelvin wave which can also be seen under calm water condition, the crest and trough of the regular wave can be clearly seen on the free surface under the wave condition.

TABLE 6.1 Comparison of main parameters of zigzag maneuver in regular head waves

Parameters	EFD	CFD	Error
1st overshoot angle (deg)	12.55	10.89	13.21%
Time (1st overshoot angle) (s)	11.20	10.56	5.71%
2nd overshoot angle (deg)	13.45	14.35	6.68%
Time (2nd overshoot angle) (s)	28.50	29.91	4.96%

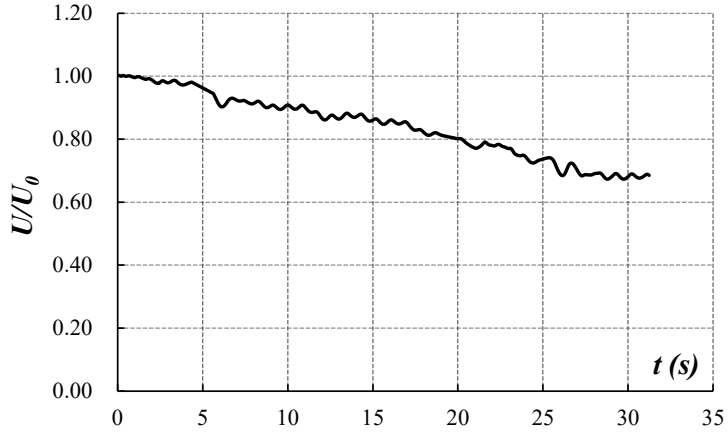

FIGURE 6.11 Dimensionless velocity for the 20/20 maneuver in regular wave condition

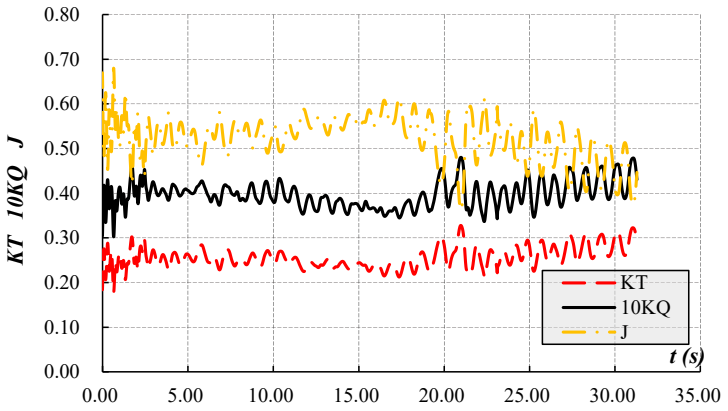

FIGURE 6.12 K_T and $10K_Q$ for the 20/20 maneuver in regular wave condition

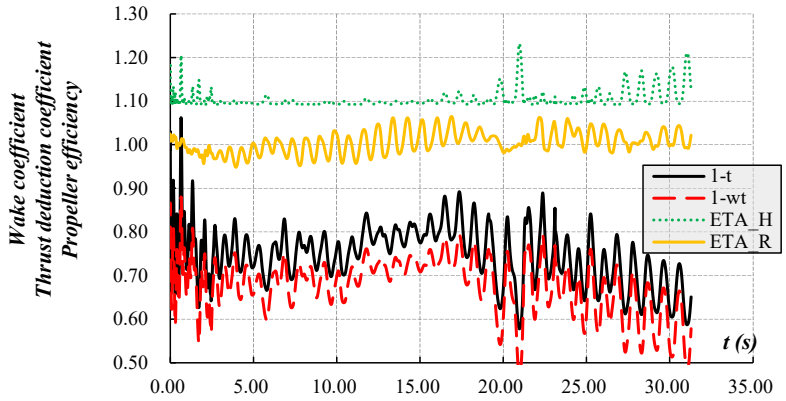

FIGURE 6.13 Self-propulsion factors for the 20/20 maneuver in regular waves

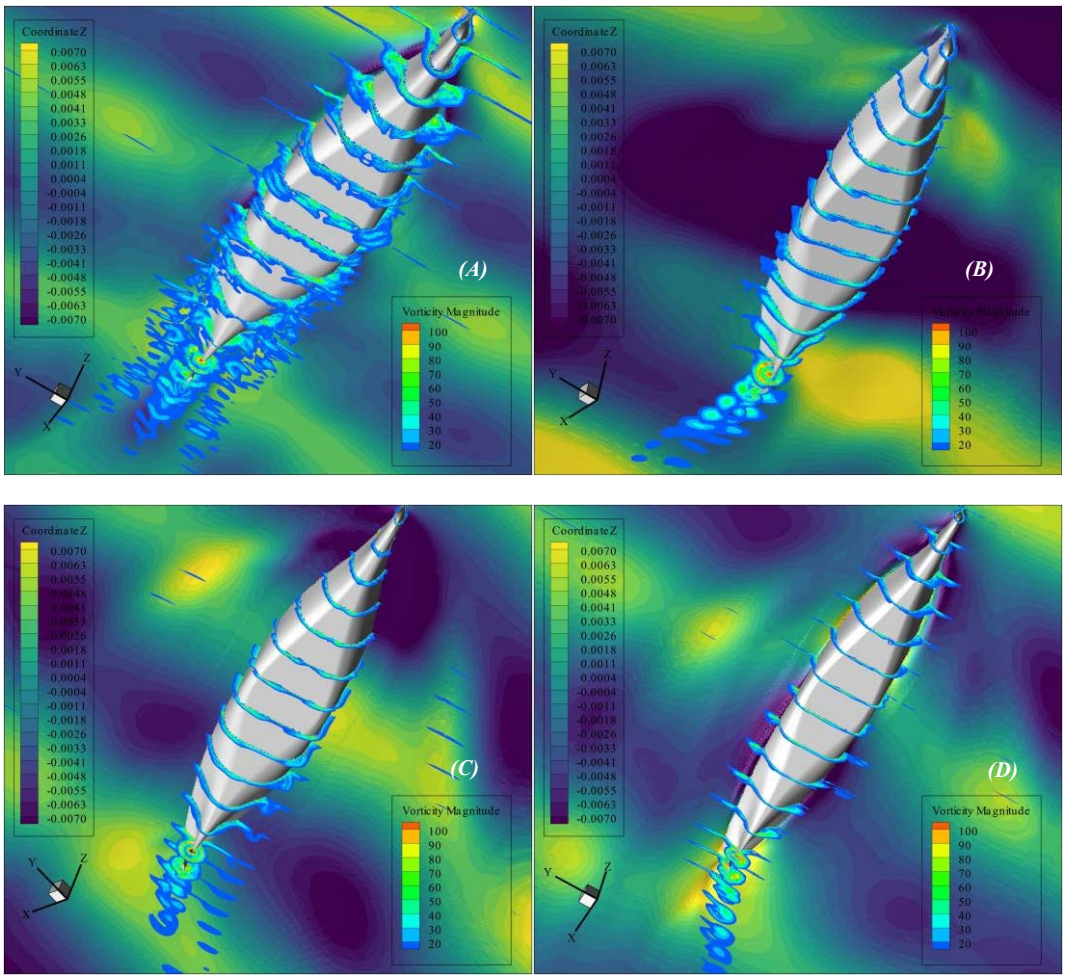

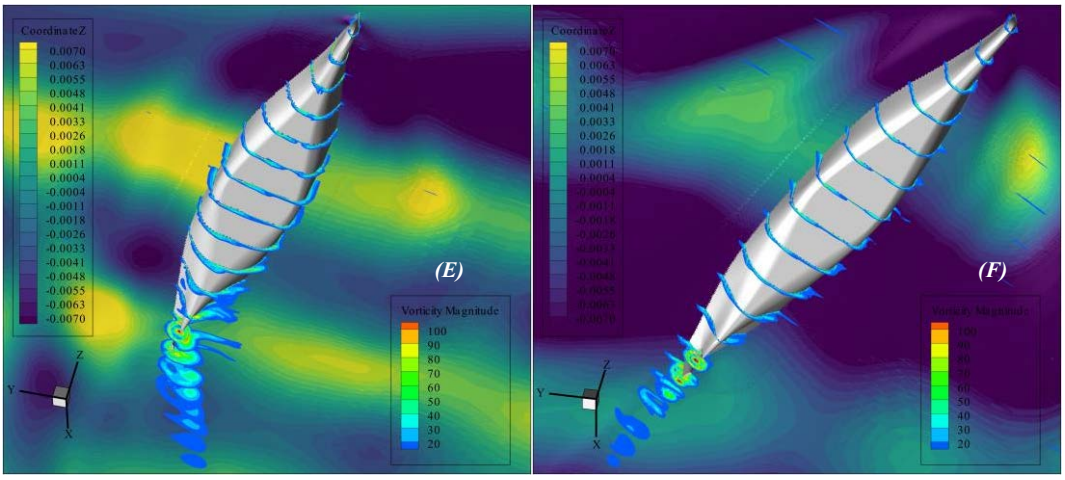

FIGURE 6.14 Snapshots of free surfaces colored by wave elevation and cross sections colored by vorticity magnitude during the 20/20 maneuver in regular wave condition

To analyze the effect of the wavelength on zigzag maneuvers in waves, various wavelengths ($\lambda/L = 0.5, 0.7, 1.0$) and a constant wave height ($H = 0.03m$) are utilized to perform the simulations. The time histories of the yaw angle and rudder angle are shown in Fig 6.15. The computed yaw and rudder angles are consistent with the experimental data. With the decrease of the wavelength, the time to reach the 1st and 2nd overshoot angle decrease obviously, and the values for the 1st and 2nd overshoot angle do not change significantly.

The roll motions of different cases are drawn in Fig 6.16. The roll motion can be considered as the superposition of the low-frequency motion influenced by the rudder execution and the high-frequency fluctuations due to the wave effect. The variation trend, amplitude and fluctuation frequency of roll motion can be simulated well, but there is still room for improvement. The error mainly comes from the difference between experimental and simulation conditions. At the beginning of the experiment, the ship has an initial roll angular velocity, which might be the main reason for the slightly larger error of long wavelength case ($\lambda/L = 1.0$). This is validated by Fig 6.17(a) in which the initial roll angular velocity of the experiment shows the large value. Fig 6.17 shows the roll angular velocities under different wavelengths. Combing Fig 6.15 and Fig 6.17, we can see that the largest roll angular velocity amplitude occurs when the yaw angles reach the peaks, and the smallest roll angular velocity amplitude occurs when the yaw angles reach zero. It is because when the yaw angle reaches the peaks under the head wave conditions, the incident wave angle will reach the peaks which makes huge roll motions. Different from the calm water conditions, the pitch motion is much more obvious under the head wave conditions. Therefore, the comparison between the experimental and numerical pitch angle is drawn in Fig 6.18. The CFD method can predict the amplitude and frequency of the pitch motion with high accuracy. In addition, the upper envelope and lower envelope of the pitch motion fluctuate during the zigzag maneuvers. Obviously, the amplitude of the pitch motion for the longer

wavelength condition is larger than that for the shorter wavelength condition.

The time histories of the forces and moments are drawn in Fig 6.19. Compared with the forces and moments under the calm water condition, those under the regular head waves have obvious high-frequency fluctuations whose amplitudes are extremely larger than those of the low-frequency values. For the lateral force coefficient, the values under various wavelength conditions are similar. However, the roll and yaw moment coefficients are influenced significantly by wave parameters. With the increase of the wavelength, the amplitude of the upper and lower envelope increases obviously.

Fig 6.20 shows the self-propulsion factors for the 20/20 zigzag maneuver under various regular wave conditions. Compared with those under the calm water condition, the variation trends and values of low-frequency parts are similar except obvious high-frequency fluctuations. In addition, when the wave height is the same, the longer the wavelength, the greater the fluctuation.

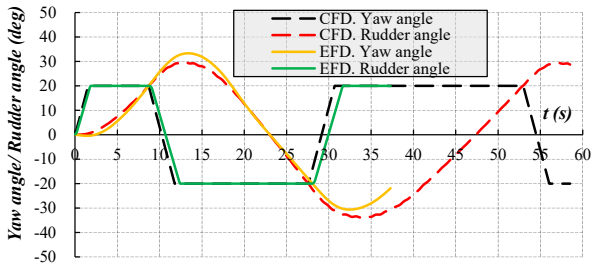

(a)

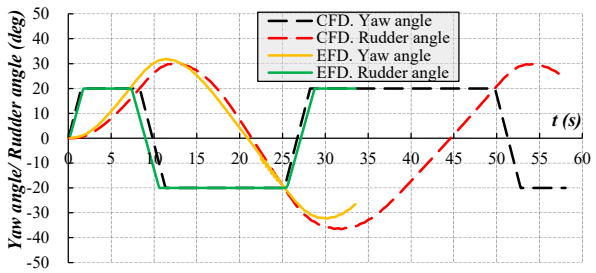

(b)

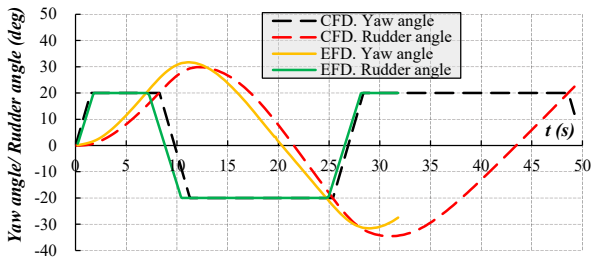

(c)

FIGURE 6.15 Yaw and rudder angle for the 20/20 maneuver under the regular wave condition ($H = 0.03m$) (a: $\lambda/L = 1.0$, b: λ/L=0.7 , c: λ/L=0.5)

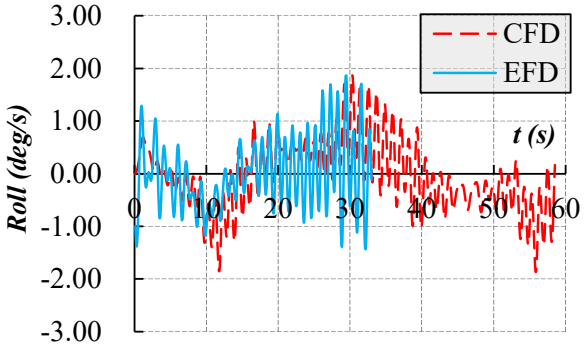

(a)

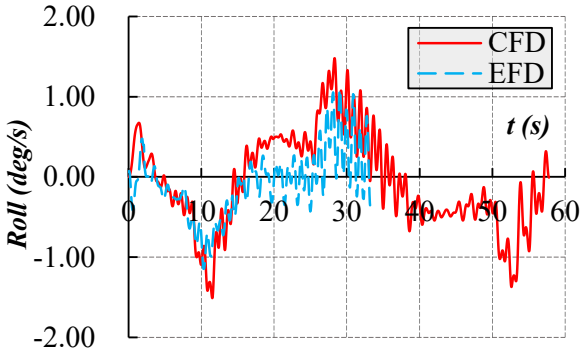

(b)

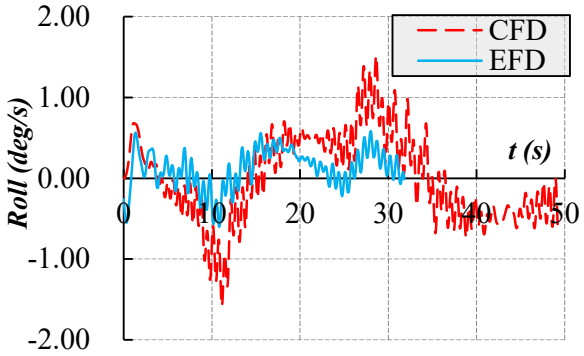

(c)

FIGURE 6.16 Roll angle for the 20/20 maneuver under the regular wave condition ($H = 0.03m$) (a: $\lambda/L = 1.0$, b: λ/L=0.7 , c: λ/L=0.5)

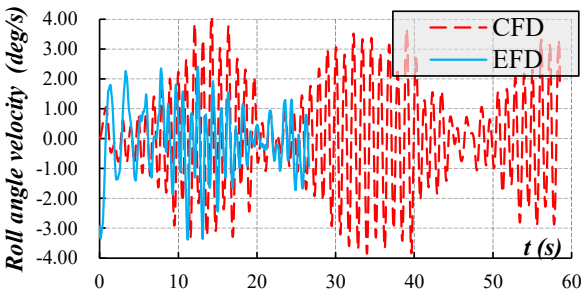

(a)

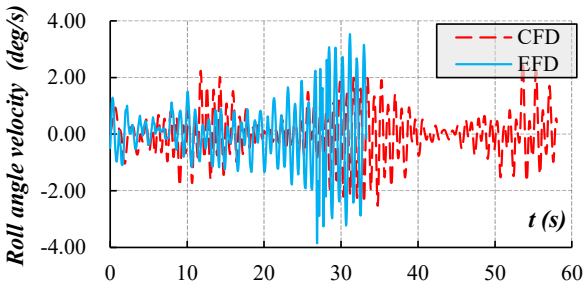

(b)

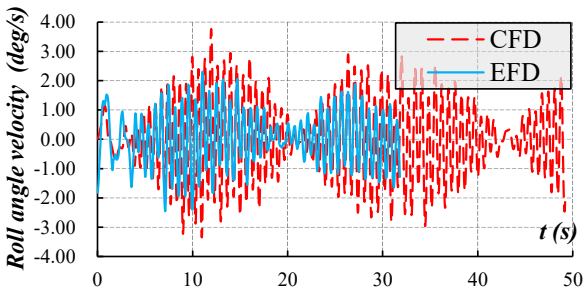

(c)

FIGURE 6.17 Roll angular velocity for the 20/20 maneuver under the regular wave condition ($H = 0.03m$) (a: $\lambda/L = 1.0$, b: λ/L=0.7 , c: λ/L=0.5)

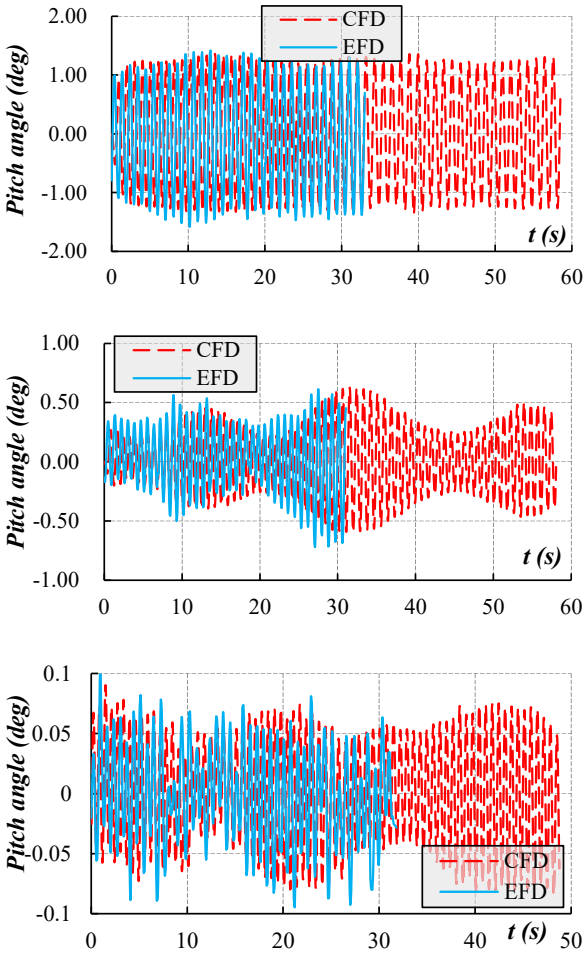

FIGURE 6.18 Pitch angle for the 20/20 maneuver under the regular wave condition ($H = 0.03m$) (Top: $\lambda/L = 1.0$, Middle: λ/L=0.7 , Bottom: λ/L=0.5)

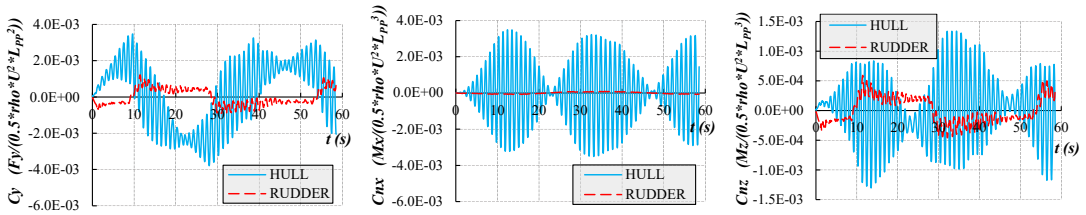

(a)

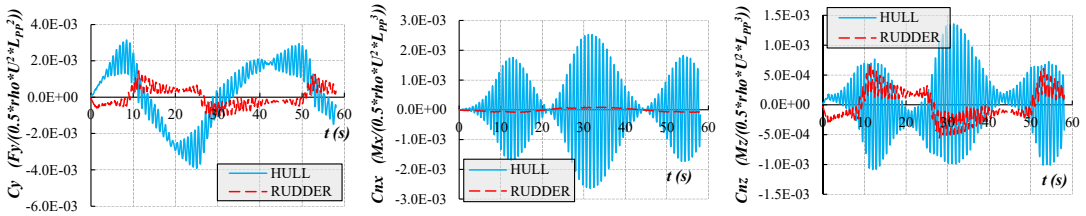

(b)

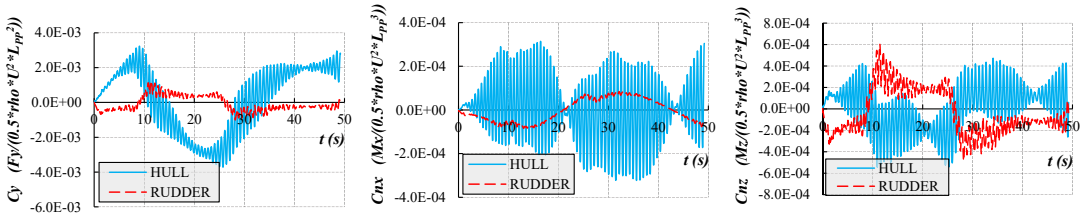

(c)

FIGURE 6.19 Dimensionless forces and moments for the 20/20 maneuver under the regular wave condition ($H = 0.03m$) (a: $\lambda/L = 1.0$, b: λ/L=0.7 , c: λ/L=0.5)

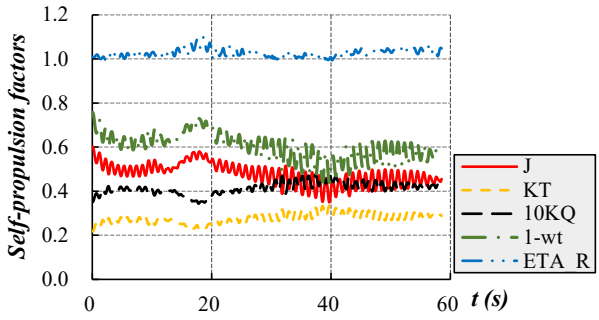

(a)

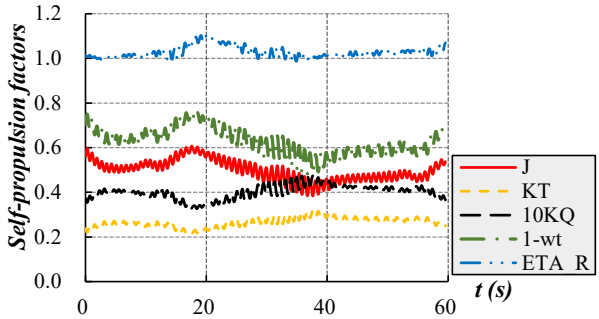

(b)

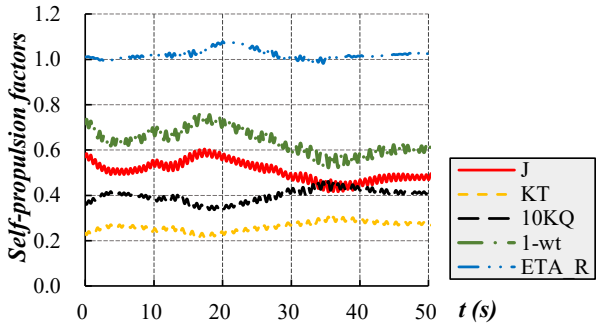

(c)

FIGURE 6.20 Self-propulsion factors for the 20/20 maneuver under the regular wave condition ($H = 0.03m$) (a: $\lambda/L = 1.0$, b: λ/L=0.7 , c: λ/L=0.5)

6.3.3 zigzag tests in irregular waves

Considering the irregular wave condition is much closer to the actual sea state, the 20/20 zigzag maneuvers under the long-crested and short-crested irregular head wave condition are simulated and summarized in Figs 6.21~6.24. The significant wave height of 3m and the mean period 6.685s for the full-scale ship corresponding to the sea state 5 are adopted to conduct the simulations. For the short-crested irregular wave, the directional spectrum $G(\theta) = \frac{2}{\pi}\cos^2\theta$ is utilized. In Fig 6.21, it seems that there is not obvious difference between the time histories of the rudder and the yaw angles in long-crested and short-crested irregular waves. The comparison between the roll angular velocities under the long-crested and short-crested irregular waves is shown in Fig 6.22. Compared with the results under the regular wave conditions, the main difference might be the frequency and amplitude of the high-frequency components. Dimensionless forces and moments for the zigzag maneuver under the irregular wave conditions are also shown in Fig 6.23. The hydrodynamic loads In Fig 6.24, self-propulsion factors under the irregular waves seem to be similar to those under the regular wave conditions.

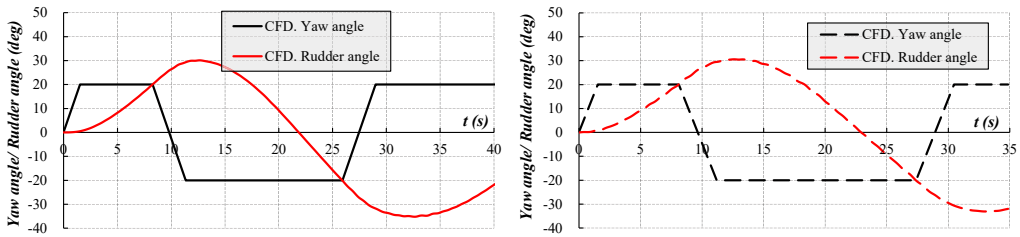

(a) (b)

FIGURE 6.21 Yaw and rudder angle for the 20/20 maneuver under the irregular wave condition (a: long-crested irregular wave, b: short-crested irregular wave)

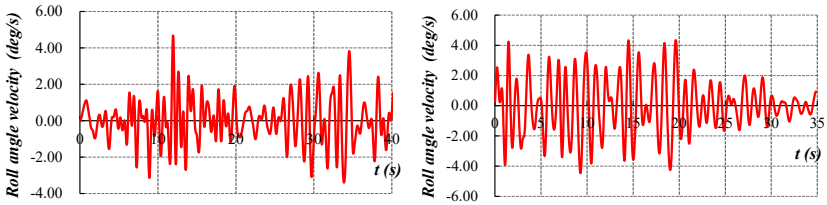

(a) (b)

FIGURE 6.22 Roll angular velocity for the 20/20 maneuver under the irregular wave condition (a: long-crested irregular wave, b: short-crested irregular wave)

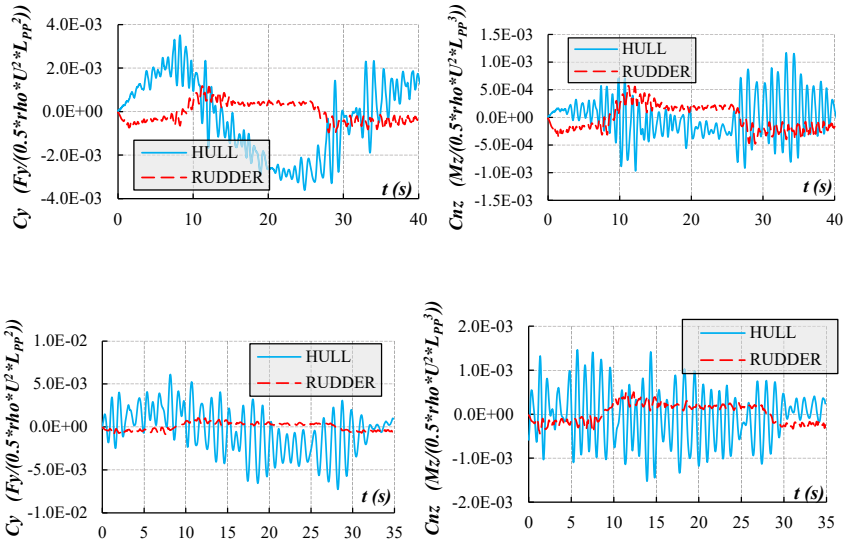

FIGURE 6.23 Dimensionless force and moment for the 20/20 maneuver in the irregular waves (Up: long-crested irregular wave, Bottom: short-crested irregular wave)

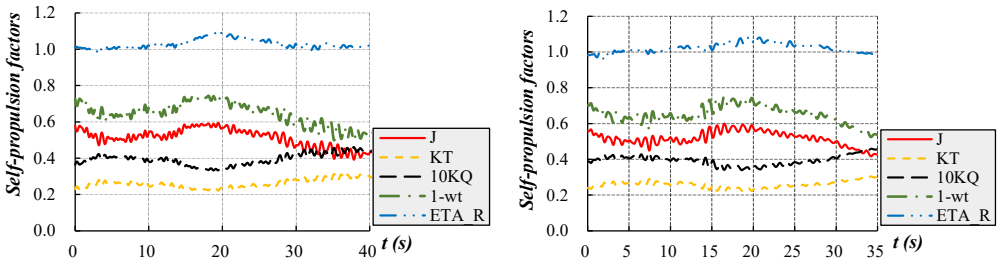

(a) (b)

FIGURE 6.24 Self-propulsion factors for the 20/20 maneuver under the irregular wave condition (a: long-crested irregular wave, b: short-crested irregular wave)

6.3.4 turning tests in regular waves

The turning maneuver with the rudder speed of -13deg/s to the rudder angle of -35 deg in regular head waves ($\lambda/L=1.0$, $H=0.03m$) was also simulated. The trajectory of the turning circle is shown in Fig 6.25. Compared with the trajectory in the calm water condition, the turning circle has an obvious drift tendency towards the starting point of the maneuvering motion in head waves which is due to the second-order wave force. The comparison between the simulated and experimental typical parameters for the turning circles are summarized in Table 6.2, which indicates the present simulation strategy can simulate the turning circle in waves with acceptable accuracy. However, due to the small value of x_{180}, the relative error is large which reveals that the drift distance is not simulated quite well. Hence, there is still some room for improvement on the prediction for the drift distance. Compared with the trajectory in the calm water condition (Fig 5.18), the maximum longitudinal and lateral displacements of the turning circle decrease. A drift motion of the turning circle to the original rudder execution point can be also seen clearly.

The dimensionless velocity shown in Fig 6.26 indicates that the speed loss phenomenon is similar to that under the calm water condition except the high-frequency fluctuations due to the wave effect. Fig 6.27 shows the comparison between the computational and experimental time histories of the roll angle and the pitch angle. The variation trend and high-frequency fluctuation can be simulated with satisfactory accuracy. The envelope of rolling and pitching motion changes significantly as the encounter wave direction. When the ship turns from the head waves to the beam seas, the pitch angle decreases rapidly from 1 deg to nearly 0 deg and the roll angle also decreases. Then, the maximum pitch angle increases to 1 deg and the maximum roll angle increases significantly to 4 deg when the ship turns from the beam seas to the following wave condition through the quartering waves. In the following wave condition, the pitch angle is still large, but the roll angle decreases obviously. Then, when the ship turns from the following wave condition to the beam seas through the quartering wave condition, the maximum roll angle increase significantly to around 6 deg and the maximum pitch angle does not change obviously.

The dimensionless forces and moments shown in Fig 6.28 have the similar low-frequency components as those under the calm water condition and the significant high-frequency components. Compared with the low-frequency parts on the hull, the high-frequency ones on the hull are extremely larger. However, the wave effect on the rudder forces is not as large as that on the hull. Fig 6.29 shows that the variation trend of self-propulsion factors under waves is the same as that in still water. The difference is that high-frequency components are added in these factors. Meanwhile, the stable value of torque coefficient during the steady turning stage decreases from about 0.5 under the calm water condition to about 0.4 under waves, which might be caused by the different aft flow field of the ship in waves compared with that in the calm water condition.

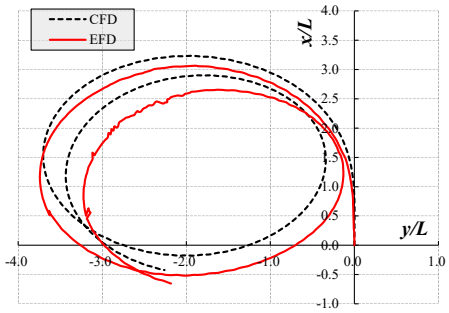

FIGURE 6.25 Trajectory of the ship turning maneuvers in a regular wave condition

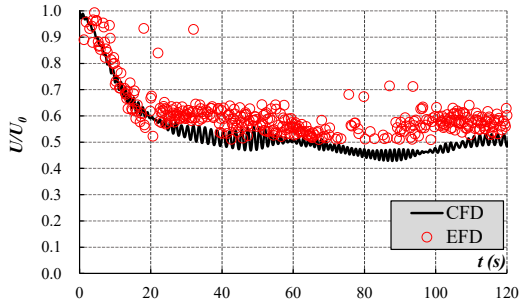

FIGURE 6.26 Dimensionless velocity for the turning maneuver in regular waves

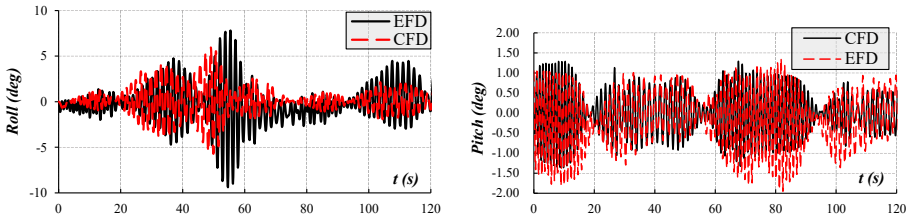

FIGURE 6.27 Roll and pitch for the turning maneuver in the regular wave condition

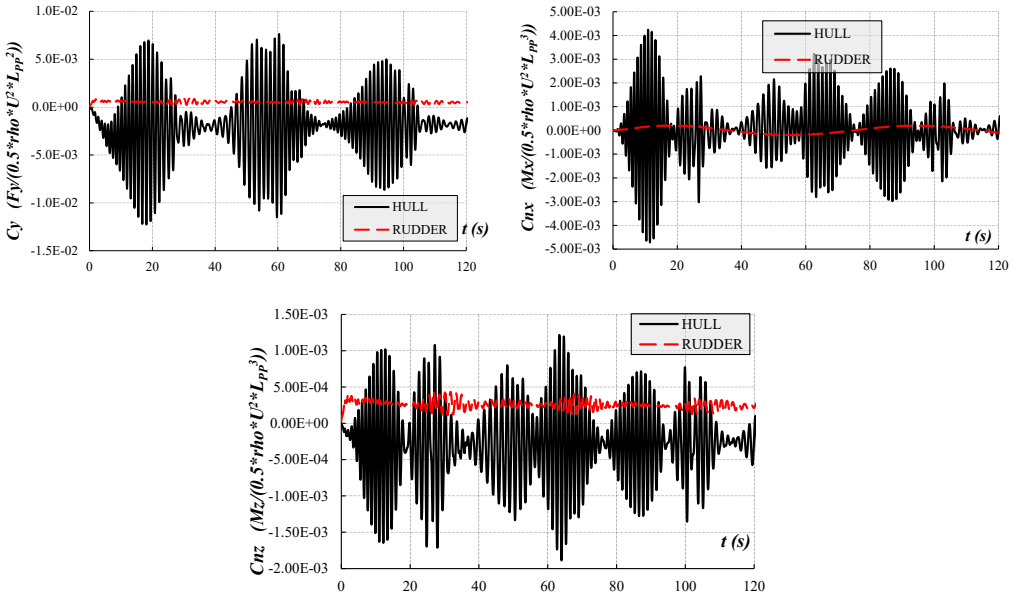

FIGURE 6.28 Dimensionless forces and moments for the 20/20 maneuver under the regular wave condition

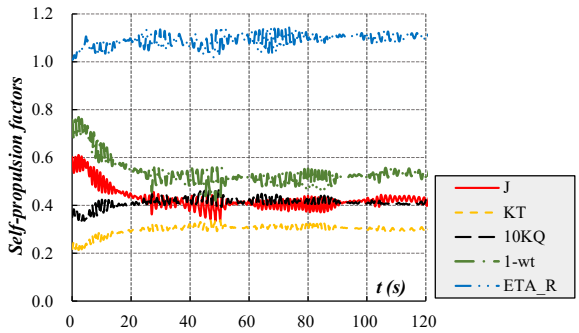

FIGURE 6.29 Self-propulsion factors for the turning maneuver in regular waves

Table 6.2 Comparison of main parameters for the turning maneuver in regular waves

Parameters	EFD	CFD	Error
Advance x_{90} (m)	3.04	3.19	4.97%
Transfer y_{90} (m)	1.67	1.60	4.50%
x_{180} (m)	1.27	1.92	50.34%
y_{180} (m)	3.74	3.66	2.14%
T_{90} (s)	17.20	18.74	8.96%
T_{180} (s)	35.40	36.76	3.84%

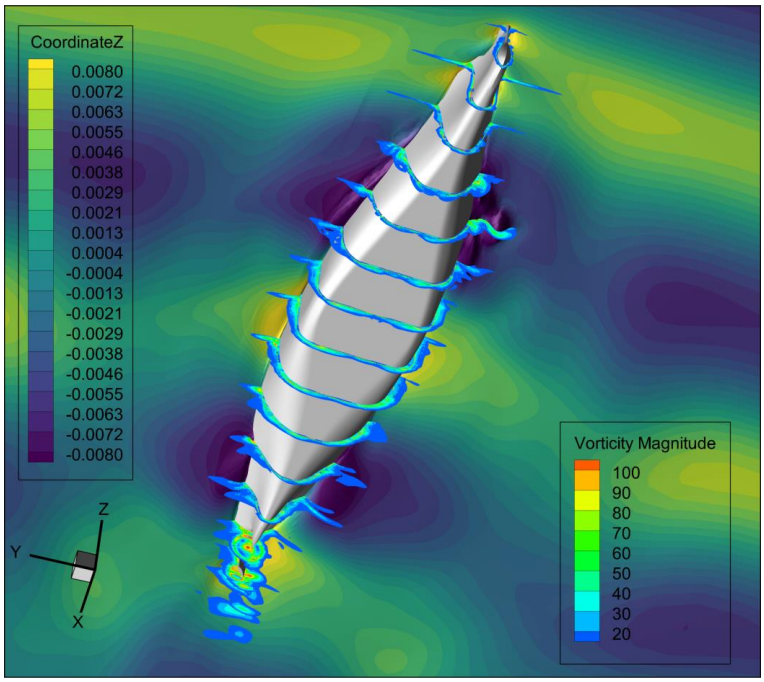

(a)

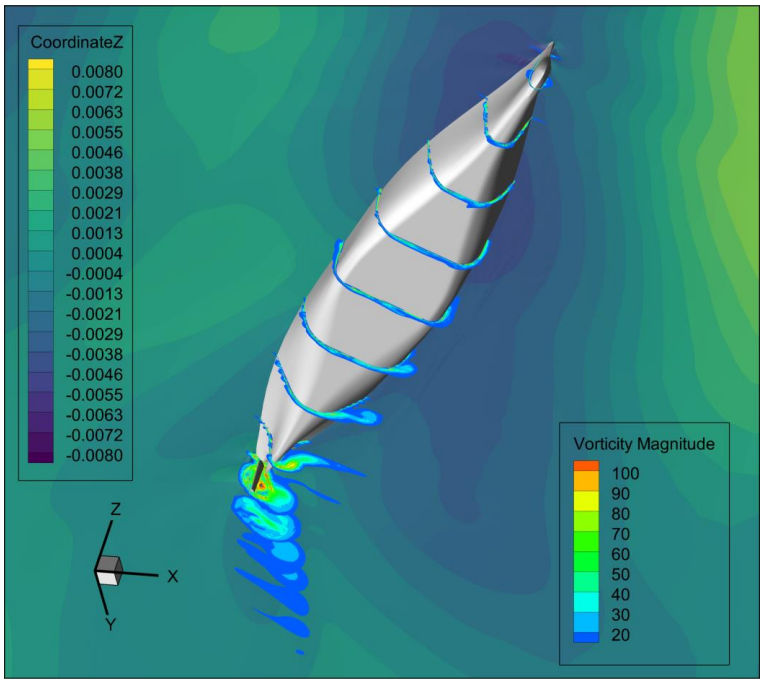

(b)

FIGURE 6.30 Snapshots of free surfaces colored by wave elevation and cross sections colored by vorticity magnitude during the turning maneuver in regular wave condition (a: transition stage; b: steady turning stage)

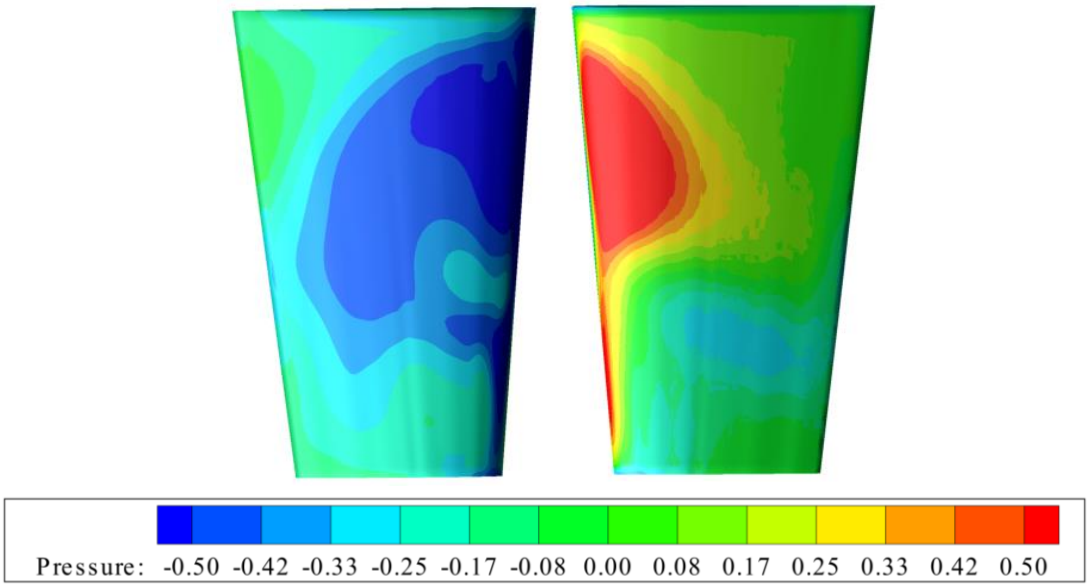

FIGURE 6.31 Snapshots of pressure on the rudder during the steady turning stage of the turning test simulation in the regular wave condition

The free surfaces colored by wave elevation and cross sections colored by vorticity magnitude during the turning maneuver in regular wave condition are drawn in Fig 6.30. The top picture is the transition stage and the bottom one is the steady turning stage. Even though the rudder angles of these two stages are the same, the vortices

distributions are different. The vortices on the port side in the steady stage will be more strengthened than those in the transition stage. The tail vortex has slight skewness in the transition stage and obvious skewness following the circulating trajectory in the steady turning stage.

The pressure distribution on the rudder during the steady turning stage is shown in Fig 6.31. As expected, high-pressure region locates on the port side and low-pressure region locates on the starboard. The wave seems not affect the pressure distribution on the rudder significantly by comparing with that under the calm water condition.

6.4 Summary

In this chapter, the numerical studies on the free-running tests in the regular and irregular waves are performed. The comparison between the experimental data with the predicted ones reveals that the present numerical simulation methods can deal with the problem of free-running test simulation in waves. The body force technique can be adopted to predict the propulsion forces for accelerating the calculation efficiency. The dynamic overset mesh can deal with the problem of multiple motions and the wave generated in the base region can keep the quality during the free-running test simulations. The simulations on the course-keeping test and the zigzag test in irregular waves also extend the scope of the application of the CFD methods.

Propulsion forces and the rudder forces during these simulations are presented to illustrate the wave effect on the hydrodynamic performance during free-running tests. Flow visualizations, such as wave elevations, generation and evolution of vortices, and the pressure on the rudder are also presented to give a better description of the flow variation during the maneuvers in waves.

The zigzag maneuvers under the calm water condition, various regular head wave conditions, the long-crested and short-crested irregular wave conditions are performed to obtain the hydrodynamic loads and self-propulsion factors. It is concluded that the ship motions and hydrodynamic loads increase with the increasing of the wavelength when the wave height keeps constant. In addition, the variation trends and magnitudes for low-frequency components of the self-propulsion factors in waves are similar to those under the calm water condition except obvious high-frequency fluctuations. The time histories of the yaw and rudder angle under the long-crested and short-crested irregular waves seem to be similar. However, the roll motion and hydrodynamic loads on the hull under two various conditions are changed obviously. The typical flow fields during the maneuvering motions are also provided to explore the evolution of the flow field and the physical mechanism.

The turning circle tests under the calm water condition and regular head waves are simulated successfully. The comparison between the non-dimensional forces under the calm water and regular waves illustrates that the wave effect is extremely significant. The wave effect on self-propulsion factors is also obtained. Compared with the roll motion of zigzag test under the same wave condition, the amplitude of roll motion of turning test in waves is obviously larger. The amplitudes of pitch motions for the turning test and zigzag test under the same wave condition are similar. Meanwhile, the drift of

the turning circle trajectory due to the wave is obvious.

The simulation on the course-keeping maneuver under the short-crested irregular waves corresponding to sea state 6 is carried out. It is concluded that the control strategy is feasible to keep the navigation course under the rough sea conditions. In addition, a course keeping simulation can be an alternative tool to predict course keeping maneuver in waves. The hydrodynamic loads and self-propulsion factors under the rough seas are also calculated.

Chapter 7 Conclusion and future work

7.1 Conclusions

Aiming at the complex problems of hydrodynamic load and motion prediction of a ship maneuvering in waves, this dissertation achieved the numerical simulations on the captive model tests in waves and the free-running tests in calm water and waves based on the CFD approach. The main content of this dissertation can be divided into two parts: the numerical studies on captive model tests in waves, and the numerical studies on free-running tests in calm water and waves. For the former, the numerical simulations based on the overset mesh technique and the Euler overlay method are proposed to conduct these simulations and the mathematical model to deal with the simulation results is also provided. For the later, the dynamic overset mesh and the body force method for propeller force prediction are adopted to conduct the simulations on the turning tests, zigzag tests, and course-keeping tests in clam water and wave conditions. The main contributions and conclusions can be summarized as follows:

1. A numerical simulation method using the overset grid and Euler overlay method on captive model tests in following waves is proposed for the first time. The verification and validation (V&V) on that reveal the effectiveness of this method. The maneuvering hydrodynamic derivatives in following waves is obtained using the numerical simulation method for the first time, which reveals that the wave has significant effect on these coefficients. The detailed changing tendencies of the hydrodynamic derivatives in waves are obtained. For instance, N_r' is twice that under the calm water condition when the ship gravity center locates on the wave trough, and $(m' + m_x' - Y_r')$ under the wave crest condition is around twice the value under the calm water condition. Based on these wave-effected hydrodynamic derivatives, a newly defined discriminant of the course stability in the following wave condition is calculated, which indicates the possible reason for the occurrence of the unstable broaching-to phenomenon. The course stability in waves with the PID control is also evaluated quantitatively relying on the Routh-Hurwitz criterion.
2. The simulation method on the captive model tests in following waves is extended to the head wave condition successfully. A mathematical model to obtain the wave-effected maneuvering hydrodynamic derivatives relying on the FFT technique in this condition is provided. By comparing the hydrodynamic derivatives in the calm water and regular head wave conditions, the obvious wave effect on these coefficients is obtained, reflecting that the wave effect on maneuvering components cannot be ignored sometimes. For Yr', it is basically unchanged from that in calm water except for extremely steep waves. For Nr', the absolute value increases significantly with the

increase of wave steepness and wavelength. The obvious difference between the hydrodynamic derivatives in calm water and wave conditions explains why the ship might undergo uncontrollable deviation under head waves rather than the calm water condition. The wave-effected nonlinear hydrodynamic derivatives are also calculated. However, a simple modification function is hard to proposed because of the nonlinear and nonmonotonic characteristics of the wave-effect hydrodynamic derivatives.

3. The simulation method based on the dynamic overset mesh with a structured grid is extended to the free-running test in the calm water condition. Based on the dynamic overset mesh approach and the body force method, the simulations on the zigzag test and turning test in calm water condition can be of satisfactory accuracy. The propulsion forces and the rudder forces are presented to illustrate the hydrodynamic performance during free-running tests. The time histories of the self-propulsion factors are also calculated, which reveals the effect of the maneuvering motions on the propeller hydrodynamic performance. Flow visualizations, such as wave elevations, generation and evolution of vortices, and the pressure on the rudder are presented to give a better description of the flow variation during the maneuvers in the calm water condition.
4. Based on the wave generation and absorption method, the numerical simulation method on the free-running tests in regular, long-crested and short-crested irregular wave conditions is provided and validated by the experimental data with reasonably accuracy. For the zigzag maneuvers, the ship motions and hydrodynamic loads increase with the increasing of the wavelength when the wave height keeps constant. The variation tendencies and magnitudes for low-frequency components of the self-propulsion factors in waves are similar to those under the calm water condition except huge high-frequency fluctuations. For the cases under the long-crested and short-crested irregular waves with the same significant wave height, the time histories of the yaw and rudder angle seem to be similar. However, the roll motion and hydrodynamic loads on the hull of these cases are significantly different. For the turning tests in regular waves, the amplitude of roll motion is obviously larger than that of the zigzag maneuvers in the same wave condition, and the amplitudes of pitch motion is similar to that of the zigzag maneuvers. Besides, the drift of the turning circle trajectory due to the second-order wave forces is obvious. For the course-keeping maneuvers using PID control in the short-crested irregular waves, the reasonable results indicates that the current course-keeping simulation strategy can be an alternative to predict course keeping maneuver in waves. Flow visualizations are also obtained revealing the differences between the cases in the calm water condition and wave conditions.

Based on these simulations, different kinds of tests on the maneuverability research in waves can be simulated using the CFD method, which will offer useful research tool for the complex hydrodynamic problem and contribute to the navigation safety in the future.

7.2 Prospects for future work

There are still many works to be improved considering the accuracy and the utilization on the design stage.

1. The present simulations focused on the maneuverability assessment on the ship in calm water and wave conditions. However, some dangerous and extreme conditions are not researched yet. In future, the free-running tests in the following wave conditions which is much more complex should be considered.
2. The present propulsion force is simulated based on a body force method in which the lateral propeller force and cavitation phenomenon are not considered. In future, more different state-of-the-art propeller force model should be considered. The cavitation phenomenon should be considered when the simulations on the propeller emergence or shallow draft condition.
3. The other kinds of controller should be carried out to achieve the simulations on all kinds of maneuvering tests automatically. For example, the stop tests involving the reverse performance of propeller should be performed.
4. Due to the huge grid number, the uncertainty analysis procedure is not proposed on the free-running tests in waves yet. In future, the method to assess the simulation uncertainty should be proposed.

References

[1] Adnan, F., and Yasukawa, H., 2008. Experimental investigation of wave-induced motions of an obliquely moving ship. In Proceedings of the 2nd Regional Conference on Vehicle Engineering and Technology, Kuala Lumpur, Malaysia. pp. 15-16.

[2] Anderson, W.K., Thomas, J.L. and Van Leer, B., 1986. Comparison of finite volume flux vector splittings for the Euler equations. AIAA journal, 24(9), pp.1453-1460.

[3] Araki, M., Umeda, N., Hashimoto, H. and Matsuda, A., 2011. An improvement of broaching prediction with a nonlinear 6 degrees of freedom model. Journal of the Japan Society of Naval Architects and Ocean Engineers, 14, pp.85-96.

[4] Ayaz, Z., Vassalos, D. and Spyrou, K.J., 2006. Manoeuvring behaviour of ships in extreme astern seas. Ocean Engineering, 33(17-18), pp.2381-2434.

[5] Bailey, P.A., 1997. A unified mathematical model describing the maneuvering of a ship travelling in a seaway. Trans RINA, 140, pp.131-149.

[6] Bonci, M., De Jong, P., Van Walree, F., Renilson, M.R. and Huijsmans, R.H.M., 2019. The steering and course keeping qualities of high-speed craft and the inception of dynamic instabilities in the following sea. Ocean Engineering, 194, p.106636.

[7] Broglia, R., Dubbioso, G., Durante, D. and Di Mascio, A., 2013. Simulation of turning circle by CFD: analysis of different propeller models and their effect on manoeuvring prediction. Applied Ocean Research, 39, pp.1-10.

[8] Broglia, R., Dubbioso, G., Durante, D. and Di Mascio, A., 2015. Turning ability analysis of a fully appended twin screw vessel by CFD. Part I: Single rudder configuration. Ocean engineering, 105, pp.275-286.

[9] Carrica, P.M., Ismail, F., Hyman, M., Bhushan, S. and Stern, F., 2013. Turn and zigzag maneuvers of a surface combatant using a URANS approach with dynamic overset grids. Journal of Marine Science and technology, 18(2), pp.166-181.

[10] Carrica, P.M., Mofidi, A. and Martin, E., 2015. Progress toward direct CFD simulation of manoeuvres in waves. In MARINE VI: proceedings of the VI International Conference on Computational Methods in Marine Engineering. pp.327-338.

[11] Carrica, P.M., Wilson, R.V., Noack, R.W. and Stern, F., 2007. Ship motions using single-phase level set with dynamic overset grids. Computers & fluids, 36(9), pp.1415-1433.

[12] Choi, J., and Yoon, S.B., 2009. Numerical simulations using momentum source wave-maker applied to RANS equation model. Coastal Engineering, 56(10), pp.1043-1060.

[13] Chorin, A.J., 1967. The numerical solution of the Navier-Stokes equations for an incompressible fluid. Bulletin of the American Mathematical Society, 73(6), pp.928-931.

[14] Cummins, W. E. 1962. The Impulse Response Function and Ship Motions.

Schiffstechnik, 9, 101-109.
[15] Davidson, J., Karimov, M., Szelechman, A., Windt, C. and Ringwood, J., 2019, July. Dynamic mesh motion in OpenFOAM for wave energy converter simulation. In Proceedings of the 14th OpenFOAM Workshop, Duisburg, Germany. pp.23-26.
[16] Dubbioso, G., Durante, D. and Broglia, R., 2013. Zig-zag maneuver simulation by CFD for a tanker like vessel. In MARINE V: proceedings of the V International Conference on Computational Methods in Marine Engineering (pp. 711-722). CIMNE.
[17] Dubbioso, G., Durante, D., Di Mascio, A. and Broglia, R., 2016. Turning ability analysis of a fully appended twin screw vessel by CFD. Part II: Single vs. twin rudder configuration. Ocean engineering, 117, pp.259-271.
[18] El Moctar, O., Lantermann, U., Mucha, P., Höpken, J. and Schellin, T.E., 2014. RANS-based simulated ship maneuvering accounting for hull-propulsor-engine interaction. Ship technology research, 61(3), pp.142-161.
[19] EMSA, 2021. Annual Overview of Marine Casualties and Incidents.
[20] Fujino, M., Yamasaki, K. and Ishii, Y., 1982. On the Stability Derivatives of a Ship Travelling in the Following Wave. Journal of the Society of Naval Architects of Japan, 152, pp.167-179.
[21] Gu, X., Ma, N., Xu, J., and Zhu, D., 2015. A simplified simulation model for a ship steering in regular waves. In: Proceedings of the 12th International Conference on the Stability of Ships and Ocean Vehicles, pp. 14–19.
[22] Hamamoto M., 1971. On the hydrodynamic derivatives for the directional stability of ships in following seas. Journal of the Society of Naval Architects of Japan. 130, pp.83-94.
[23] Hamamoto M., 1973. On the Hydrodynamic Derivatives for the Directional Stability of Ships in Following Seas (Part 2). Journal of the Society of Naval Architects of Japan. 133, pp.133-42.
[24] Hamamoto, M. and Kim, Y.S., 1993. A new coordinate system and the equations describing manoeuvring motion of a ship in waves. Journal of the Society of Naval Architects of Japan, 1993(173), pp.209-220.
[25] Hasnan, M.A.A., Yasukawa, H., Hirata, N., Terada, D. and Matsuda, A., 2020. Study of ship turning in irregular waves. Journal of Marine Science and Technology, 25(4), pp.1024-1043.
[26] He, S., Kellett, P., Yuan, Z., Incecik, A., Turan, O. and Boulougouris, E., 2016. Manoeuvring prediction based on CFD generated derivatives. Journal of hydrodynamics, 28(2), pp.284-292.
[27] Hino, T., 1999. An interface capturing method for free surface flow computations on unstructured grids. Journal of the society of Naval Architects of Japan, 186, pp.177-183.
[28] Hirano, M., Takashina, J., Takaishi, Y. and Saruta, T., 1980. Ship turning trajectory in regular waves. Publication of: West Japan Society of Naval Architects, (60) pp17-31.
[29] Inoue, S. and Murahashi, T., 1965. A calculation of turning motion in regular waves. Transactions of the west-Japan society of naval architects, vol 31, pp 77-99.

[30] IMO., 2002a. Standards for ship manoeuvrability. Resolution MSC.137(76), International Maritime Organization.
[31] IMO, 2002b. Explanatory notes to the standards for ship manoeuvrability. MSC/Circ. 1053, International Maritime Organization.
[32] IMO., 2013. Interim Guidelines for Determining Minimum Propulsion Power to Maintain the Manoeuvrability in Adverse Conditions. MEPC.232(65), International Maritime Organization.
[33] ITTC., 2008. The manoeuvring committee Final report and recommendations to the 25th ITTC. In: Proceedings of 25th international towing tank conference, Fukuoka, Japan.
[34] ITTC., 2011. The manoeuvring committee Final report and recommendations to the 26th ITTC. In: Proceedings of 26th international towing tank conference, Rio de Janeiro, Brazil.
[35] ITTC., 2014. The manoeuvring committee Final report and recommendations to the 27th ITTC. In: Proceedings of 27th international towing tank conference, Copenhagen, Denmark.
[36] ITTC., 2017a. ITTC Quality System Manual Recommended Procedures and Guidelines: Uncertainty Analysis in CFD: Verification and Validation, Methodology and Procedures. International Towing Tank Conference.
[37] ITTC., 2017b. The manoeuvring committee Final report and recommendations to the 28th ITTC. In: Proceedings of 28th international towing tank conference, Wuxi, China.
[38] ITTC., 2021. The specialist committee on manoeuvring in waves Final report and recommendations to the 29th ITTC. In: Proceedings of 29th international towing tank conference, Virtual.
[39] Jameson, A., 1991, June. Time dependent calculations using multigrid, with applications to unsteady flows past airfoils and wings. In 10th Computational fluid dynamics conference (p. 1596).
[40] Kawamura, T., Miyata, H. and Mashimo, K., 1997. Numerical simulation of the flow about self-propelling tanker models. Journal of marine science and technology, 2(4), pp.245-256.
[41] Kim, D., Song, S., Jeong, B. and Tezdogan, T., 2021a. Numerical evaluation of a ship's manoeuvrability and course keeping control under various wave conditions using CFD. Ocean Engineering, 237, p.109615.
[42] Kim, D., Song, S. and Tezdogan, T., 2021b. Free running CFD simulations to investigate ship manoeuvrability in waves. Ocean Engineering, 236, p.109567.
[43] Kim, J., O'sullivan, J., and Read, A., 2012. Ringing analysis of a vertical cylinder by Euler overlay method. In 31st International Conference on Ocean, Offshore and Arctic Engineering. pp.855-866.
[44] Kobayashi, H. and Kodama, Y., 2015. Developing spline based overset grid assembling approach and application to unsteady flow around a moving body. In MARINE VI: proceedings of the VI International Conference on Computational Methods in Marine Engineering. pp.838-849.
[45] Kodama, Y., Ohashi, K., Umezaki, Y. and Hirata, N., 2012. Development of

UP_GRID, and Overset Grid System for Computing Flows past Ship Hulls with Appendages. In Proceedings of the 26th Computational Fluid Dynamics Symposium, D08-1.
[46] Ma, C., Ma, N., and Gu, X., 2019. Time Domain Simulations of Ship Maneuvering and Roll Motion in Regular Waves Based on a Hybrid Method. In 38th International Conference on Ocean, Offshore and Arctic Engineering.
[47] Ma, C., Ma, N., Gu, X. and Feng, P., 2021. Numerical Study on Hydrodynamic Forces and Course Stability of a Ship in Surf-Riding Condition Based on Planar Motion Mechanism Tests. Journal of Offshore Mechanics and Arctic Engineering, 143(6).
[48] Mofidi, A. and Carrica, P.M., 2014. Simulations of zigzag maneuvers for a container ship with direct moving rudder and propeller. Computers & fluids, 96, pp.191-203.
[49] Motora, S., Fujino, M., Koyanagi, M., Ishida, S., Shimada, K. and Maki, T., 1981. A Consideration on the Mechanism of Occurrence of the Broaching-to Phenomenon. Journal of the Society of Naval Architects of Japan, 1981(150), pp.211-222.
[50] MSC 93/21/5, 2014, Safety evaluation of the interim guidelines for determining minimum propulsion power to maintain the manoeuvrability of ships under adverse weather conditions. International Maritime Organization
[51] MSC 93/INF.13, 2014, Safety evaluation of the interim guidelines for determining minimum propulsion power to maintain the manoeuvrability of ships under adverse weather conditions. International Maritime Organization.
[52] MEPC 67/INF.22, 2014, Japanese activity on "Minimum propulsion power to maintain the manoeuvrability of ships in adverse conditions". International Maritime Organization.
[53] MEPC 67/4/16, 2014, Comments on documents MSC 93/21/5 and MSC 93/INF.13 and consideration on the requirement of minimum propulsion power needed to maintain the manoeuvrability of a ship under adverse conditions. International Maritime Organization.
[54] Nishimura K., Hirayama T., 2003. Maneuvering and Motion Simulation of a Small Vessel in Waves. In: International Conference on Marine Simulation and Ship Maneuverability, MARSIM'03, Kanazawa, Japan.
[55] Nonaka K. 1990. On the manoeuvring motion of a ship in waves. Transactions of the West-Japan Society of Naval Architects, 80: 73-86.
[56] Ohashi, K., 2018. Development of numerical method to simulate flows around a ship at propulsion conditions in regular waves coupling with the ship propulsion plant model. Applied Ocean Research, 73, pp.141-148.
[57] Ohashi, K., Hino, T., Kobayashi, H., Onodera, N. and Sakamoto, N., 2019. Development of a structured overset Navier–Stokes solver with a moving grid and full multigrid method. Journal of Marine Science and Technology, 24(3), pp.884-901.
[58] Ohmori, T., 1998. Finite-volume simulation of flows about a ship in maneuvering motion. Journal of marine science and technology, 3(2), pp.82-93.

[59] Orihara, H. and Miyata, H., 2003. Evaluation of added resistance in regular incident waves by computational fluid dynamics motion simulation using an overlapping grid system. Journal of Marine Science and Technology, 8(2), pp.47-60.
[60] Papanikolaou, A., Zaraphonitis, G., Bitner-Gregersen, E., Shigunov, V., El Moctar, O., Soares, C.G., Reddy, D.N. and Sprenger, F., 2015, November. Energy efficient safe ship operation (SHOPERA). In SNAME 5th World Maritime Technology Conference. OnePetro.
[61] Patankar, S.V., 1981. A calculation procedure for two-dimensional elliptic situations. Numerical heat transfer, 4(4), pp.409-425.
[62] Phillips, A.B., Turnock, S.R. and Furlong, M., 2009. Evaluation of manoeuvring coefficients of a self-propelled ship using a blade element momentum propeller model coupled to a Reynolds averaged Navier Stokes flow solver. Ocean Engineering, 36(15-16), pp.1217-1225.
[63] Phillips, A.B., Turnock, S.R. and Furlong, M., 2010. Accurate capture of propeller-rudder interaction using a coupled blade element momentum-rans approach. Ship technology research, 57(2), pp.128-139.
[64] Queutey, P., Deng, G., Wackers, J., Guilmineau, E., Leroyer, A. and Visonneau, M., 2012. Sliding grids and adaptive grid refinement for RANS simulation of ship-propeller interaction. Ship technology research, 59(2), pp.44-57.
[65] Rameesha, T.V. and Krishnankutty, P., 2019. Numerical study on the manoeuvring of a container ship in regular waves. Ships and Offshore Structures, 14(2), pp.141-152.
[66] Reed A. M. and Beck R. F., 2018. Mathematical models of maneuvering in waves: historical perspectives and the state of the art. In: Proceeding of the 13th International conference on stability of ships and ocean vehicles. 16-21 September, Kobe, Japan.
[67] Renilson, M. R. and Driscoll, A., 1982., Broaching - An Investigation into the Loss of Directionary Control in Severe Following Seas, Read at Spring Meeting of R. I. N. A.
[68] Roe, P.L., 1986. Characteristic-based schemes for the Euler equations. Annual review of fluid mechanics, 18(1), pp.337-365.
[69] Sadat-Hosseini, H., Carrica, P., Stern, F., Umeda, N., Hashimoto, H., Yamamura, S. and Mastuda, A., 2011. CFD, system-based and EFD study of ship dynamic instability events: Surf-riding, periodic motion, and broaching. Ocean Engineering, 38(1), pp.88-110.
[70] Sakamoto, N., Carrica, P.M. and Stern, F., 2012a. URANS simulations of static and dynamic maneuvering for surface combatant: part 1. Verification and validation for forces, moment, and hydrodynamic derivatives. Journal of marine science and technology, 17(4), pp.422-445.
[71] Sakamoto, N., Carrica, P.M. and Stern, F., 2012b. URANS simulations of static and dynamic maneuvering for surface combatant: part 2. Analysis and validation for local flow characteristics. Journal of marine science and technology, 17(4), pp.446-468.
[72] Sanada, Y., Tanimoto, K., Takagi, K., Gui, L., Toda, Y. and Stern, F., 2013.

Trajectories for ONR Tumblehome maneuvering in calm water and waves. Ocean Engineering, 72, pp.45-65.
[73] Seo M G, Kim Y., 2011. Numerical analysis on ship maneuvering coupled with ship motion in waves. Ocean Engineering, 38(17–18): 1934-1945.
[74] Seo, J.H., Seol, D.M., Lee, J.H. and Rhee, S.H., 2010. Flexible CFD meshing strategy for prediction of ship resistance and propulsion performance. International Journal of Naval Architecture and Ocean Engineering, 2(3), pp.139-145.
[75] Shen, Z., Wan, D. and Carrica, P.M., 2015. Dynamic overset grids in OpenFOAM with application to KCS self-propulsion and maneuvering. Ocean Engineering, 108, pp.287-306.
[76] Shigunov, V., El Moctar, O., Papanikolaou, A., Potthoff, R. and Liu, S., 2018. International benchmark study on numerical simulation methods for prediction of manoeuvrability of ships in waves. Ocean Engineering, 165, pp.365-385.
[77] Simonsen, C.D., Otzen, J.F., Klimt, C., Larsen, N.L. and Stern, F., 2012, August. Maneuvering predictions in the early design phase using CFD generated PMM data. In 29th symposium on naval hydrodynamics (pp. 26-31).
[78] Skejic, R. and Faltinsen, O.M., 2008. A unified seakeeping and maneuvering analysis of ships in regular waves. Journal of marine science and technology, 13(4), pp.371-394.
[79] Son, K.H. and Nomoto, K., 1982. On the coupled motion of steering and rolling of a ship in following seas. Journal of the Society of Naval Architects of Japan, 1982(152), pp.180-191.
[80] Stern, F., Kim, H.T., Patel, V.C. and Chen, H.C., 1988. A viscous-flow approach to the computation of propeller-hull interaction. Journal of Ship Research, 32(04), pp.246-262.
[81] Tahara, Y., Longo, J. and Stern, F., 2002. Comparison of CFD and EFD for the Series 60 CB= 0.6 in steady drift motion. Journal of marine science and technology, 7(1), pp.17-30.
[82] Triantafyllou, M.S., 1982. A consistent hydrodynamic theory for moored and positioned vessels. Journal of Ship Research, 26(02), pp.97-105.
[83] Ueno, M., Nimura, T., and Miyazaki, H., 2003. Experimental study on manoeuvring motion of a ship in waves. In: International Conference on Marine Simulation and Ship Maneuverability, MARSIM'03, Kanazawa, Japan.
[84] Wang J, Zou L, Wan D. 2017. CFD simulations of free running ship under course keeping control. Ocean engineering. 2017 Sep 1; 141:450-64.
[85] Wang J, Wan D. 2018. CFD investigations of ship maneuvering in waves using naoe-FOAM-SJTU Solver. Journal of Marine Science and Application. 2018 Sep;17(3):443-58.
[86] Wang J, Zou L, Wan D. 2018. Numerical simulations of zigzag maneuver of free running ship in waves by RANS-Overset grid method. Ocean Engineering. 2018 Aug 15; 162:55-79.
[87] Windt, C., Davidson, J., Chandar, D.D., Faedo, N. and Ringwood, J.V., 2020. Evaluation of the overset grid method for control studies of wave energy converters in OpenFOAM numerical wave tanks. Journal of Ocean Engineering and Marine

Energy, 6(1), pp.55-70.
[88] Xu, J., 2015. Study on 6-DOF Numerical Model of Ship Maneuvering Motions in Waves. Shanghai Jiao Tong University.
[89] Xu, Y., Bao, W., Kinoshita, T. and Itakura, H., 2007. A PMM experimental research on ship maneuverability in waves. In: International Conference on Offshore Mechanics and Arctic Engineering (OMAE).
[90] Xu, Y., Kinoshita, T., Bao, W. and Itakura, H., 2011. Wave Drift Forces Affecting on Maneuverability Derivatives. In: International Conference on Offshore Mechanics and Arctic Engineering (OMAE), pp. 877-884.
[91] Yasukawa, H., 2006. Simulations of Ship Maneuvering in Waves (1st report: turning motion). Journal of the Japan Society of Naval Architects and Ocean Engineers, 4, pp.127-136.
[92] Yasukawa, H., 2008. Simulations of ship maneuvering in waves: 2nd report: zig-zag and stopping maneuvers. Journal of the Japan Society of Naval Architects and Ocean Engineers, 7(0), pp.163-170.
[93] Yasukawa, H., Hasnan, M.A.A. and Matsuda, A., 2021. Validation of 6-DOF motion simulations for ship turning in regular waves. Journal of Marine Science and Technology, 26(4), pp.1096-1111.
[94] Yasukawa, H., Hirata, N., Matsumoto, A., Kuroiwa, R. and Mizokami, S., 2019. Evaluations of wave-induced steady forces and turning motion of a full hull ship in waves. Journal of marine science and technology, 24(1), pp.1-15.
[95] Yoon, H.Y., 2009. Force/moment and phase-averaged stereo PIV flow measurements for surface combatant in PMM maneuvers. Ph. D. thesis, The University of Iowa.
[96] Yoon, H., Simonsen, C.D., Benedetti, L., Longo, J., Toda, Y. and Stern, F., 2015a. Benchmark CFD validation data for surface combatant 5415 in PMM maneuvers–Part I: Force/moment/motion measurements. Ocean Engineering, 109, pp.705-734.
[97] Yoon, H., Longo, J., Toda, Y. and Stern, F., 2015b. Benchmark CFD validation data for surface combatant 5415 in PMM maneuvers–Part II: Phase-averaged stereoscopic PIV flow field measurements. Ocean engineering, 109, pp.735-750.
[98] Yu, L., Wang, S. and Ma, N., 2021. Study on wave-induced motions of a turning ship in regular and long-crest irregular waves. Ocean Engineering, 225, p.108807.
[99] Zhang, W., Zou, Z.J. and Deng, D.H., 2017. A study on prediction of ship maneuvering in regular waves. Ocean engineering, 137, pp.367-381.
[100] Zhu, D., 2016. Study on Ship Maneuvering and Rolling Prediction and Course-Keeping Control in Waves. Shanghai Jiao Tong University.

Acknowledgements

I consider my very lucky to have a chance to join the exchange program to conduct my doctoral research at the Yokohama National University. In this tough period with the worldwide spreading of coronavirus, I suffered more carefulness and assistances from the supervisor, lab members, the staffs in the YNU, and the teachers and friends in SJTU. All these remembers are priceless treasure in all my life.

I am very grateful for the guidance and assistance provided by Prof. Takanori Hino. It is an honor for the author to have a chance to study under an excellent supervisor. Every time the author faces some hard problem, Prof. Hino will talk with the author and provide some enlightening guidance on that. He also provides the opportunity for the author to communicate with the researchers at National Maritime Research Institute, which helps a lot for this research. The author also thanks the guidance and concern of the supervisor Prof. Ning Ma at Shanghai Jiao Tong University to improve the quality of the research content. The valuable opportunity to join this double-degree program is also provided by Prof. Ma. Associate professor Youhei Takagi is thanked for his assistance of the course guidance during the doctoral periods of the author and the help for the graduation arrangement.

The lab members in YNU and SJTU are thanked for their help and accompany. Mr. Terui is thanked for the help of daily life as a tutor, which makes me familiar with the daily life in Japan faster. Mr. Igosawa is thanked for the help of dealing with the registration formalities when I just came to Japan. All the students in the hydrodynamics research group are thanked for their assistance warm and friendly including the graduated friends such as Mr. Shinji, Mr. Harushi, and Mr. Nambu and so on. The careful staffs in YNU also help me a lot during the quarantine period and the life in YNU. Dr. Wei Zhang and Ms. Jing Xu are thanked for the valuable experimental data they provided.

I am highly obliged and grateful to the financial support provided by the Ministry of Education, Culture, Sports, Science and Technology (MEXT) Scholarship during the period when I stay in Japan.

During the time in Japan, my parents and lover are always contact with me to encourage me when I feel confused and support my academic pursuit. I would like to express my infinite thanks to them.